THESIS FOR THE DEGREE OF DOCTOR OF PHILOSOPHY

Charge Transport in Polymer-based Insulating Materials for High Voltage Applications: Effect of Single- and Multi-layered Structures

ANH T. HOANG

High Voltage Engineering
Department of Materials and Manufacturing Technology
CHALMERS UNIVERSITY OF TECHNOLOGY
Gothenburg, Sweden 2016

Charge transport in polymer-based insulating materials for high voltage applications: effect of single- and multi-layered structures
Anh T. Hoang
ISBN 978-91-7597-500-9

Doktorsavhandlingar vid Chalmers tekniska högskola
Ny serie nr. 4181
ISSN 0346-718X

High Voltage Engineering
Department of Materials and Manufacturing Technology
Chalmers University of Technology
SE-41296 Gothenburg
Sweden
Telephone + 46 (0)31-772 1000

Chalmers Bibliotek, Reproservice
Gothenburg, Sweden 2016

Charge transport in polymer-based insulating materials for high voltage applications: effect of single- and multi-layered structures

Anh T. Hoang
Division of High Voltage Engineering
Department of Materials and Manufacturing Technology
Chalmers University of Technology

Abstract

Polymer composites have been widely employed as electrical insulating materials for high voltage components and devices such as power cables, gas-insulated systems, rotating machines, line and post insulators, *etc.* Such materials are usually made by introducing inorganic oxides (SiO_2, TiO_2, Al_2O_3, MgO) into polymeric matrices *e.g.* polyethylene (PE), epoxy, silicone rubber. Reported experimental evidences indicate improvements which can be achieved in dielectric strength, partial discharge resistance, and life time of the polymer composites as compared to their base materials. However, the reasons behind the advancements in materials' electrical performance have not been clearly elucidated in many cases. In this context, the present thesis concentrates on analyzing the influence of filler particles on the transport of charge carriers in two polymer-based insulations namely nanofilled PE and microfilled enamel, which are novel insulating materials for high voltage direct current (HVDC) cables and electric motors, respectively. The contribution of internal interfaces between insulating layers existing in multi-layered structures to their electrical conduction is also considered.

The investigation was conducted by following a similar methodology including both experiments and computer simulations. Charge generation and transport in the insulating materials were stimulated by applying a DC voltage or by depositing charges on their surfaces by means of corona charging. Charging currents through the insulations and the decay of surface potentials were measured and experimental results were compared for the composite materials and the base polymers, while simulation techniques were utilized for explaining the materials' measured responses. As the interaction of the fillers and the polymeric matrices strongly depends on the filler morphology and properties, the results are reported separately for the two insulations.

As for PE nanocomposites and its unfilled counterpart, specimens of thin films were prepared, whereas multi-layered structures were made by pressing them together at high temperature. Charging currents measured at various temperatures indicated a remarkable reduction in DC conductivity of the nanofilled dielectrics as compared to PE, making the former preferable insulating materials for HVDC cables, especially for those working under enhanced electric stresses. The observed effect was associated with the decreased charge mobility and increased trap energy in the nanocomposites as compared to the corresponding properties of the unfilled PE. By comparing the measured currents obtained on single-layered

and multi-layered structures, the impact of an insulation–insulation interface on the electrical conduction was revealed and analyzed. Further, the field dependencies were established for the transient currents and the quasi-steady state currents that were utilized for examining the dominant conduction mechanisms in the studied materials. A computer model was employed for studying the generation and transport of charge carriers in the insulations at various temperatures. The simulations demonstrated that apart from the reasons mentioned above, the weakening charge transport process in the nanocomposites is in great extent caused by the suppression of charge injection at electrode–insulation interfaces.

On the other hand, the insulation coatings of enameled wires are inherently multi-layered structures consisting of at least two layers of different materials. This study focuses on a partial discharge resistant enamel insulation that was created by introducing chromium oxide (Cr_2O_3) particles of micrometer size into the base polymer. Experiments were conducted mainly on multi-layered enamel coatings, while some tests were also performed on single-layered flat samples and filler powder. Thus, contributions of each phase (filler and polymer matrix) to the electrical conduction and the dielectric response of the filled enamel were highlighted. Charge transport in the multi-layered enamel coatings was studied in details by analyzing the surface potential decay characteristics. Accordingly, potential decay mechanisms due to the combination of charge injection, polarization, and intrinsic conduction were revealed, each of them dominating within a certain time interval. Based on that, a computer model of charge transport in multi-layered insulating structures was developed to reproduce the measured surface potentials. In this model, the consideration of the barrier effect of the internal interface is of utmost importance.

Keywords: polyethylene, nanocomposite, enamel insulation, charge transport, charge mobility, DC conductivity, charging current, surface potential decay, charge injection, charge trapping and de-trapping.

Acknowledgments

First and foremost, I would like to express my sincere gratitude to my supervisor Prof. Yuriy Serdyuk for his valuable guidance, consistent support, and carefully reading and revising my manuscripts. I will never forget numerous extended discussions we had over the past five years, in which he significantly broadened my horizons by generously sharing his immense knowledge and experience, constantly providing critical comments on the research outcomes, and suggesting new ideas. I am profoundly grateful to my examiner and assistant supervisor Prof. Stanislaw Gubanski for his valuable guidance and kind support. He always inspired me by suggesting most relevant and up-to-date literature and by giving insightful remarks on the experimental results. His patience and continuous encouragement have meant a lot to me in difficulties that I constantly encountered throughout the project.

My grateful acknowledgements go to Chalmers Area of Advance in Energy and the Swedish Foundation for Strategic Research for providing the financial support of this project.

I am grateful to Dr. Göran Paulsson and Dr. Henrik Hillborg from ABB Corporate Research, Sweden for providing material samples for the investigations on enamel insulations as well as for their helpful discussions. Dr. Le Wang who started the work on DC conductivity measurements of polyethylene nanocomposites is acknowledged for his kind help and instructions. I sincerely thank Love Pallon, Dongming Liu, Amir Pourrahimi, and Prof. Ulf Gedde from Royal Institute of Technology, Sweden for supplying specimens of polyethylene nanocomposites and for their fruitful cooperation within our joint project. I really appreciate the instructions and assistance in performing the measurements of thermally stimulated discharge currents by Quyet Nguyen, Werner Wirges, and Prof. Reimund Gerhard from University of Potsdam, Germany. Dr. Karolina Gaska is thanked for her help in preparing scanning electron micrographs of the polyethylene nanocomposites.

I would like to take this opportunity to thank all the current and former staff at the division of High Voltage Engineering, of which I am proud to be a member. I really appreciate many helpful comments and advice they gave me. Colleagues from the division of Electric Power Engineering are thanked for creating a pleasant working environment. Thanks to all my friends in Gothenburg for creating enjoyable activities outside university and helping in various matters.

Last but certainly not least, I am greatly indebted to my parents and my brother for always understanding and supporting me. Their continuous encouragements are invaluable to me in every step of my life. My special thanks go to my wife for her love and personal sacrifices as well as for sharing with me every single difficult moment and to my daughter who makes our home full of laughs and happiness.

Anh Hoang
Gothenburg, Sweden
November 2016

List of abbreviations

1D	One-dimensional
2D	Two-dimensional
3D	Three-dimensional
PE	Polyethylene
LDPE	Low-density polyethylene
HDPE	High-density polyethylene
XLPE	Cross-linked polyethylene
PAI	Polyamide-imide
PEI	Polyester-imide
PA	Polyamide
EVA	Ethylene-vinyl acetate
PET	Polyethylene terephthalate
HVDC	High voltage direct current
SPD	Surface potential decay
TSD	Thermally stimulated discharge
PD	Partial discharge
DFT	Density functional theory
SCLC	Space-charge-limited current
TFVL	Trap-filled voltage limit
MWS	Maxwell–Wagner–Sillars
ADC	Anomalous discharging current
DAQ	Data acquisition card
PEA	Pulse electro-acoustic
NDM	Negative differential mobility
SCD	Space charge distribution
TC	Transient current
Ref	Reference
NC	Nanocomposite
RT	Room temperature

Table of contents

1. Introduction

1.1. Background and objectives

Reliable electric power supply plays a vital role in the modern society. As the global population continuously increases, being forecasted to reach around ten billions in 2050, the worldwide demand for electric energy grows. Since the use of traditional fossil fuels such as coal and oil becomes undesirable due to their environmental impacts, the humans should rely on renewable resources of energy, *e.g.* hydro, solar, wind, tidal, *etc*. These energy types are usually located distantly from the consumption centers, which requires the development of long electrical transmission systems [1]. Additionally, the availability of renewable energy resources such as wind and solar is hardly predictable as they are strongly dependent on weather, which makes it difficult to control them. Today, the integration of the renewable energy sources into the power grids has been greatly alleviated owing to the recent advancements in power electronic technologies [2]. The combination of these changes in generation and transmission of the electric energy therefore results in extremely hazardous working conditions for the insulating materials of electrical devices and components in the electric power systems. These challenges include the enhanced electrical and thermal stresses as well as the presence of high-frequency harmonics that may cause partial discharge (PD) activities, eventually leading to premature failures of the insulating materials [3-7].

Polymers have been widely used as insulating materials thanks to a number of their technological advantages over traditional insulations. For example, the polymeric insulations have gradually expelled the use of paper and oil in high voltage cables or of glass and porcelain insulators in overhead transmission lines. However, due to the above mentioned challenges, employing conventional polymeric insulations appears to be less efficient and economical. To deal with the problem, one of the promising approaches is the development of composite materials by introducing inorganic fillers of nanometer or micrometer sizes into base polymers. It has been reported that numerous polymer composites showed great improvements in dielectric strength, PD resistance, and life time [8-11] as compared to their base materials. Although the effect of the fillers on the properties of composite insulations has been widely reported, there is still lack of understanding physical mechanisms behind the modifications in their properties.

This investigation focuses on analyzing contributions of filler particles, in particular their properties and content, to the charge transport and, to some extent, to the dielectric relaxation processes in composite insulations. Two polymer composites were considered, namely nanofilled polyethylene (PE) and microfilled enamel insulation. While the former is considered as an advanced insulating material for high voltage direct current (HVDC) cables, the latter is a PD resistant insulation for electric motors. Even though two materials are

different in various aspects, from properties, insulation structures to their applications, the investigations carried out on them are featured by the same methodology that comprises both experimental techniques and computer simulations. Additionally, effects of insulation–insulation interfaces on the charge transport in the studied materials are examined. The latter topic is significant due to the fact that the insulation–insulation interfaces are inevitable in insulating systems but investigations of their impact on the charge transport are rather limited [12-14].

Charge generation and transport in low-density polyethylene (LDPE) and its nanocomposites were stimulated by applying a DC voltage or by depositing charge carriers on their surfaces using corona discharge in air. The specimens were single-layered films and double-layered structures that were created by hot pressing the thin films together. The responses of the materials to the applied electrical stresses, *i.e.* time-varying charging currents and surface potentials, were obtained and compared for the nanocomposites and the unfilled counterpart under the same conditions in order to highlight the role of the filler particles in the charge transport. Charge carrier mobilities and trap energies in the studied dielectrics, as the most important parameters governing the charge transport processes, were derived from measured surface potential decay (SPD) characteristics and thermally stimulated discharge (TSD) currents. Further, field dependencies were established for transient currents and quasi-steady state currents, which were used for examining the dominant conduction mechanisms in the materials. Thereafter, a computer model of charge transport has been developed for simulating physical processes taking place in the insulations exposed to DC electric fields. The model is featured by charge injection at electrodes, charge trapping, de-trapping, and recombination while the input parameters for such processes were mostly gained from the experimental outcomes. Thus, the transient processes associated with transport of mobile carriers and accumulation of immobile charges in the bulk were exhibited, from which the effects of nanoparticles and temperature were analyzed and discussed.

Insulating coatings of enameled wires, on the other hand, are characterized by a multi-layered structure that usually consists of at least two layers of different materials. Experiments were conducted mainly on the enamel coating rather than on flat samples of a single-layered structure. As an electric field is applied to the multi-layered enamel insulation, interfacial polarization arises playing an important role in the relaxation processes, which was shown through analyzing results of dielectric spectroscopy measurements. The methodology described above was also employed for studying the electrical conduction in the enamel insulation, focusing on decay characteristics of surface potentials. The decay mechanisms on the multi-layered insulating structure were studied in details by examining experimental data in accordance to various hypotheses proposed in literature. The computer model used for simulating the charge transport in single-layered films was modified for modeling the potential decay on the multi-layered enamel insulation.

1.2. Outline of the thesis

The thesis is organized in the following structure.

Chapter 2 provides a brief overview of mechanisms of the electrical conduction and charge transport in insulating materials. The first section descibes charge generation and transport processes with the emphasis on the effect of localized and extended states existing in polymeric insulations. Thereafter, possible conduction mechanisms at high electric fields and the influence of an insulation–insulation interface on the charge transport are discussed. The second section concentrates on the reported properties of the materials under consideration, where electrical characteristics of both the base polymers and the filler materials are outlined. The last section reviews the existing computer models for simulating the charge transport in insulating materials.

Chapter 3 focuses on the description of the studied materials, procedures for their preparation, experimental methods as well as the computer model used in the investigation. The chapter starts with providing general information about the nanofiller particles and the procedure for preparing LDPE nanocomposites as well as micrographs showing the dispersion of nanofillers in the polymer matrix. Besides, the layered structure of enamel insulation is illustrated. The following section outlines the experimental techniques including measurements of DC conductivity, dielectric response, surface potential decay, and thermally stimulated discharge currents. The arrangements of test setups are depicted, whereas experimental conditions and procedures as well as parameters of applied electrical stresses on the materials are given.

Chapter 4 presents experimental and simulated results with regards to the electrical conduction and charge transport in LDPE and its nanocomposites. The first section summarizes the results of DC conductivity measurements where influences of antioxidant, filler content, temperature, and electric field on the measured charging currents are analyzed. Further, the measured potential decay characteristics are shown and discussed. The role of the internal interface between two layers in the multi-layered insulating structure is exhibited by comparing experimental results obtained on them and on single-layered insulations under similar conditions. Charge mobilities and trap energy distributions in the studied materials derived from the measured SPD are presented next. The trap depth that has not been detected using the results of the SPD measurements is therefore uncovered by means of TSD current measurements. At last, the transport and trapping of charges in the unfilled and nanofilled LDPE are compared and analyzed using numerical approach.

Chapter 5 reports experimental results on DC conductivity, dielectric response and potential decay for the enamel insulations. Based on that, contributions of different relaxation processes are analyzed and potential decay mechanisms are revealed. Further, the charge mobilities in both layers deduced from the measured SPD characteristics are presented. The obtained mobilities have been used as inputs for the computer model of charge transport in the multi-layered enamel insulation. The parculiarities of the model and the simulated results are discussed in the last section.

Finally, the concluding remarks drawn from the performed studies and the suggestions for future work are given in Chapter 6.

1.3. List of publications

This thesis is based on the research presented in the following publications and manuscripts:

1. **A. T. Hoang**, Y. V. Serdyuk, and S. M. Gubanski, "Charge transport in multi-layered enamel insulation," in manuscript.
2. **A. T. Hoang**, Q. D. Nguyen, W. Wirges, R. Gerhard, Y. V. Serdyuk, and S. M. Gubanski, "Open-circuit thermally stimulated currents in LDPE/Al_2O_3 nanocomposite," Ann. Rep. 2016 IEEE Conf. Electr. Insul. Dielectr. Phenomena (CEIDP 2016), Oct. 16–19, 2016, Toronto, Canada, pp. 611–614.
3. **A. T. Hoang**, L. Pallon, D. Liu, Y. V. Serdyuk, S. M. Gubanski, and U. W. Gedde, "Charge transport in LDPE nanocomposites Part I – Experimental approach," *Polymers*, vol. 8, 87 (19 pp.), 2016.
4. **A. T. Hoang**, Y. V. Serdyuk, and S. M. Gubanski, "Charge transport in LDPE nanocomposites Part II – Computational approach," *Polymers,* vol. 8, 103 (16 pp.), 2016.
5. **A. T. Hoang**, Y. V. Serdyuk, and S. M. Gubanski, "Mechanisms of surface potential decay on enamel wire coatings," *IEEE Trans. Dielectr. Electr. Insul.*, vol. 22, pp. 3470–3480, 2015.
6. **A. T. Hoang**, L. Wang, Y. V. Serdyuk, S. M. Gubanski, D. Liu, L. Pallon, C. Cobo Sanchez, W. Li, and U. W. Gedde, "DC electrical conductivity of LDPE-based nanocomposites," Proc. 9th Int'l. Conf. Insulated Power Cables (Jicable'15), Jun. 21–25, 2015, Versailles, France, paper B6.5.
7. **A. T. Hoang**, Y. V. Serdyuk, and S. M. Gubanski, "Charge decay on enamel wire surface," Proc. Int'l. Conf. High Voltage Engineering & Application (ICHVE 2014), Sept. 8–11, 2014, Poznan, Poland, paper A-4-3.
8. **A. T. Hoang**, Y. V. Serdyuk, and S. M. Gubanski, "Electrical characterization of a new enamel insulation," *IEEE Trans. Dielectr. Electr. Insul.*, vol. 21, pp. 1291–1301, 2014.

The author also contributed to the following publications, which are not included in the thesis:

9. A. Pourrahimi, **A. T. Hoang**, D. Liu, L. Pallon, S. M. Gubanski, R. T. Olsson, U. W. Gedde, and M. S. Hedenqvist, "Highly efficient interfaces in nanocomposites based on polyethylene and ZnO nano/hierarchical particles: A novel approach toward ultralow electrical conductivity insulations," *Adv. Mater.,* vol. 28, pp. 8651–8657, 2016.
10. A. Pourrahimi, L. Pallon, D. Liu, **A. T. Hoang**, S. M. Gubanski, M. S. Hedenqvist, R. T. Olsson, and U. W. Gedde, "Polyethylene nanocomposites for the next generation of ultra-low transmission-loss HVDC cables: insulations containing moisture-resistant MgO nanoparticles," *ACS Appl. Mater. Interfaces*, vol. 8, pp. 14824–14835, 2016.
11. L. Pallon, **A. T. Hoang**, A. Pourrahimi, M. S. Hedenqvist, F. Nilsson, S. M. Gubanski, U. W. Gedde, and R. T. Olsson, "The impact of MgO nanoparticle interface in ultra-insulating polyethylene nanocomposites for high voltage DC cables," *J. Mater. Chem. A*, vol. 4, pp. 8590–8601, 2016.
12. L. Pallon, R. T. Olsson, D. Liu, A. Pourrahimi, M. S. Hedenqvist, **A. T. Hoang**, S. M. Gubanski, and U. W. Gedde, "Formation and the structure of freeze-dried MgO nanoparticle foams and their electrical behaviour in polyethylene," *J. Mater. Chem. A*, vol. 3, pp. 7523–7534, 2015.
13. **A. T. Hoang**, T. Hammarström, T. Bengtsson, Y. V. Serdyuk, and S. M. Gubanski, "Partial discharge behavior of a newly developed enamel insulation at various voltage rise times," Proc. Int'l. Symp. Electr. Insul. Materials (ISEIM 2014), Jun. 1–5, 2014, Niigata City, Japan, pp. 241–244.

2. Literature review

Unlike the situation in conducting materials where free electrons exist, charge carriers in insulating materials are tightly bounded and only a small amount of charges are activated by an external electric field constituting a leakage current. The ability of insulation to provide such a leakage current is characterized by material bulk resistivity or its inverse quantity, *i.e.* bulk conductivity. These properties are usually measured in a laboratory following a standard procedure [15] by inserting a material sample in an electrode system comprising a high voltage electrode for applying a DC voltage, a measuring electrode connecting to a current sensor, and a guard electrode for eliminating a surface current. In such measurements, insulating materials are subjected to a polarization process that is exhibited by a gradually decaying current. The polarization may last for few hours, few days or even few months depending on the material conductivity. Conduction current is quantified at a quasi-steady state achieved at a reasonable extended duration after the voltage application. The conduction current while neglecting charge diffusion is expressed as:

$$j = qE\sum_i n_i\mu_i \,, \tag{2.1}$$

where q is elementary charge ($q = 1.6\times10^{-19}$ C), E being the electric field, n_i and μ_i stand for the density and mobility of the i^{th} type of charge carriers participating in transport, respectively. At a low field strength, the current usually increases linearly with the applied electric field and the well-known Ohm's law is applicable. At a high electric field, the voltage–current relationship may depart from Ohm's law that the conduction current rises faster than a linear dependence on the applied field. This has been related to various physical processes arising at the interfaces and within the bulk of the insulations.

In this section, an outline of electronic conduction is briefly recalled. The reader is referred to numerous reviews [16-20] and original investigations [21-26] on the topic for an insightful understanding of each mechanism. Ionic conduction, despite being observed in polymeric insulators such as polyamide 6.6 (nylon 6,6) [20], will not be considered here. First of all, the ionic conduction may not be relevant to pure polymers due to the lack of polar lattice for the movement of ions [20]. Furthermore, the appearance of the ionic conduction in polymeric dielectrics is theoretically related to the presence of impurities and additives like antioxidants and cross-linking agents that generate ionic heterocharges [19], but the experimental evidences are not commonly reported. Finally, the mechanism has been found to dominate at low electric field ~10^5 V/m [27], which is not the main focus of this work.

2.1. Electrical conduction in insulating materials at high electric fields

The term “high electric fields” in the title of this section appears to be ambiguous and it primarily needs to be clarified. The high electric fields are commonly referred to the field strength exceeding 10^7 V/m or 10 kV/mm. For several insulating polymers such as polyethylene (PE), this field level has been found as the onset of a conduction mechanism of other type than ohmic [28].

The electric field of high magnitude may stimulate the generation of extrinsic charge carriers and their transport in insulating materials. Contributions of such elementary processes as charge formation and movement to a macroscopic quantity of externally measured current are not obviously observed as the measured current is averaged by integration over the thickness of the used sample. Moreover, despite the simple relationship between the conduction current and concentration of charge carriers as well as their mobility, see eqn. (2.1), the latter two quantities are not easily attained from the measured conduction current. Thus, meaningful interpretation of the measured conduction current in insulations is a truly complicated task that requires the understanding of physical processes involved. To alleviate the task, this section provides a short summary on the elementary processes contributing to the electrical conduction in insulating materials with the focus on charge carriers of electronic origin.

2.1.1. Charge generation

The band theory has been commonly used as one of the starting points for explaining the properties of different materials including conductors, semiconductors, and insulators. We recall here a brief description of the energy band structure in insulations formulated in [29]. A schematic illustration of the energy band diagram adopted from this publication [29] is shown in Figure 2.1. Valence and conduction bands are respectively the highest filled and the first unoccupied bands at zero absolute temperature. The separation between these two is denoted as a forbidden band gap or simply a band gap. In the middle of the band gap, Fermi energy level is determined as a level at which the probability of finding an electron using Fermi–Dirac distribution function is always 50%. Further, vacuum level is known as the reference energy level of electron at rest after being completely removed from the material. Thus, the energy required for removing an electron from the Fermi level to the vacuum level is determined as work function. Electron affinity, on the other hand, is defined as the energy required for removing an electron from the bottom of the conduction band to the vacuum level.

For insulating materials, the band gap is as large as 6–8 eV so that the probability of exciting an electron from the valence band to the conduction band is negligibly small. Instead, sources of charge carriers can be donors and acceptors existing at the edge of the conduction and valence bands. Charge injection at electrode–insulation interfaces is another type of charge generation.

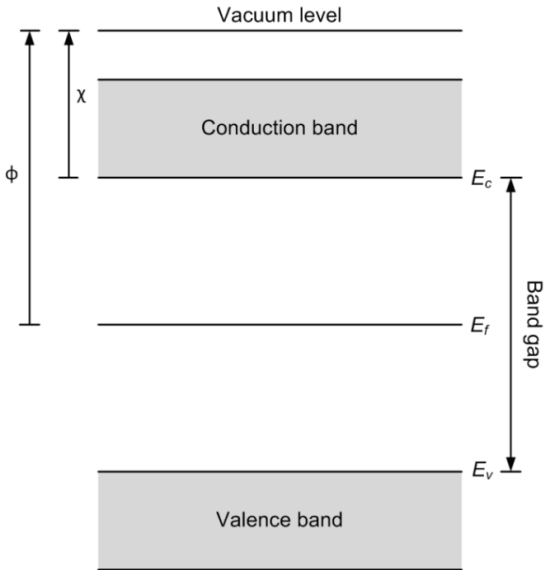

Figure 2.1. Schematic diagram of the energy band in insulating materials. E_v, E_c, and E_f are energy levels corresponding to the valence band, conduction band, and Fermi level; φ and χ denote the work function and the electron affinity, respectively.

2.1.1.1. Charge injection at insulation interfaces

Charge injection at insulation interfaces has been described by thermionic emission or Schottky emission [20]. The phenomenon was originally associated with the current emitted from a metal surface into vacuum. Its extended form with Schottky's field correction term has been widely applied for quantifying currents injected at metal–semiconductor junctions and has been recently adapted for quantifying the current injected at electrode–insulation interfaces. When a charge carrier is released from an electrode, there exists an interaction between them, which can be expressed by the electrostatic attraction between this charge carrier and an image charge. The latter is determined as a charge of opposite polarity mirrored of the real charge through the electrode. The attraction yields a potential barrier of coulombic form:

$$\Phi(x) = -\frac{q^2}{16\pi\varepsilon x}, \tag{2.2}$$

where ε is material permittivity, x is the distance from the electrode. As an electric field E is applied, the potential barrier is modified as shown in Figure 2.2:

$$\Phi(x) = -\frac{q^2}{16\pi\varepsilon x} - qEx. \tag{2.3}$$

As a result, the potential barrier height is lowered and the resulting injected current is field-dependent:

$$j_S = AT^2 \exp\left(-\frac{q\varphi}{kT}\right)\exp\left(\frac{q}{kT}\sqrt{\frac{qE}{4\pi\varepsilon}}\right), \tag{2.4a}$$

$$j_S = j_0 \exp\left(\frac{\beta_S\sqrt{E}}{kT}\right). \tag{2.4b}$$

Here, A is Richardson's constant ($A = 1.2\times10^6$ $Am^{-2}K^{-2}$); T being absolute temperature, K; k stands for Boltzmann's constant ($k = 1.38\times10^{-23}$ JK^{-1}); φ is the barrier height for charge injection, eV; j_0 is current density at low field, Am^{-2}; β_S is known as the Schottky coefficient showing the field-dependent behavior:

$$j_0 = AT^2 \exp\left(-\frac{q\varphi}{kT}\right), \tag{2.5a}$$

$$\beta_S = \sqrt{\frac{q^3}{4\pi\varepsilon}}. \tag{2.5b}$$

In reality, not all electrons possessing energies exceeding the potential barrier can be injected. A certain proportion R of electrons ($R \leq 1$) is reflected back to the electrode and the current density in eqn. (2.4) should be reduced by a factor of (1–R) [20]. It has been pointed out that the high frequency permittivity should be used in (2.4) because the time for electrons crossing the coordinate x_{max} corresponding to the maximum barrier height is small [20].

For extremely high electric fields ~10^9 V/m, Fowler–Nordheim injection is dominant. Accordingly, electrons possessing energy lower than the barrier height can penetrate through the barrier as its width becomes sufficiently thin due to the presence of high field strength. Such mechanism is referred to as tunneling and its treatment is based on quantum mechanical theory [20]. The injected current density j can be simplified to

$$j = C_1E^2 \exp\left(-\frac{C_2}{E}\right), \tag{2.6}$$

where C_1 and C_2 are constant parameters. As the current depends only on the field strength rather than on temperature, the mechanism is also known as the field emission or cold emission.

2.1.1.2. Charge generation in insulation bulk

As mentioned above, donors and acceptors are presented in the forbidden gap of insulating materials; specifically they are located below the conduction band and above the valence band. The application of an electric field stimulates the excitation of electrons from donor states to the conduction band and/or of holes from acceptor states to the valence band, the latter is equivalent to the electron transfer in the opposite direction. Such processes may follow Poole–Frenkel mechanism that is governed by the electrostatic interaction between an electron (a hole) and an ionized donor (an acceptor), resulting in a potential energy

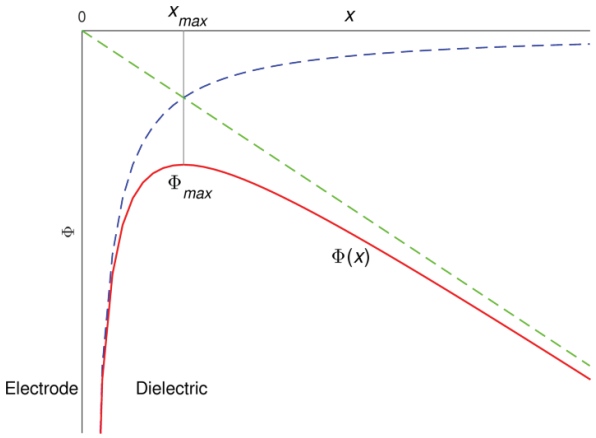

Figure 2.2. Barrier height for charge injection at electrode. Φ_{max} is the maximum barrier height achieved at the distance x_{max} to electrode.

similar to that in eqn. (2.3):

$$\Phi(r) = -\frac{q^2}{4\pi\varepsilon r} - qEr\,. \tag{2.7}$$

Here, r denotes the distance of separation. Similar to Schottky's mechanism, the potential barrier height is lowered by the applied electric field, yielding the field dependency of the material conductivity σ:

$$\sigma_{PF} = \sigma_c \exp\left(-\frac{W}{2kT}\right)\exp\left(\frac{q}{2kT}\sqrt{\frac{qE}{\pi\varepsilon}}\right), \tag{2.8a}$$

$$\sigma_{PF} = \sigma_0 \exp\left(\frac{\beta_{PF}\sqrt{E}}{2kT}\right), \tag{2.8b}$$

where σ_c is a constant, W is potential barrier at zero field, σ_0 and β_{PF} are respectively low-field conductivity and Poole–Frenkel coefficient that are defined as:

$$\sigma_0 = \sigma_c \exp\left(-\frac{W}{2kT}\right), \tag{2.9a}$$

$$\beta_{PF} = \sqrt{\frac{q^3}{\pi\varepsilon}}\,. \tag{2.9b}$$

It should be pointed out that there is an inconsistency in the reported multiplication factor for $E^{1/2}/kT$ in the exponential functions of Poole–Frenkel model. In some publications [26, 30, 31], it is simply accepted that the factor is doubled as compared to that in eqn. (2.8b) and thus the field dependence of the conductivity has a form:

$$\sigma = \sigma_0 \exp\left(\frac{\beta_{PF}\sqrt{E}}{kT}\right). \tag{2.10}$$

Note that both Schottky injection mechanism and Poole–Frenkel model show the exponential dependencies on the square root of electric field $E^{1/2}$, as can be seen in eqns. (2.4) and (2.8). The coefficient of Poole–Frenkel model is two time higher than that in Schottky's formula ($\beta_{PF} = 2\beta_S$). For examining the validity of these models, experimental data of quasi-steady state currents and DC conductivity are usually presented as functions of $E^{1/2}$ in semi-logarithmic plots, *i.e.* $\log(j)$ *vs.* $E^{1/2}$ and $\log(\sigma)$ *vs.* $E^{1/2}$. The slopes of the dependencies allow for deriving relative permittivities, which can be compared with values reported in the literature. This procedure often showed the departure of the relative permittivity used for best fitting the characteristics from the parameter values obtained in dielectric spectroscopy measurements [21, 26, 63]. This indicates that the above-mentioned mechanisms were not dominant in the conduction process. To explain the experimental data, Taylor and Lewis [21] proposed an alternative to Schottky's mechanism where a general form of the potential barrier described by a power law is used instead of the coulombic form. On the other hand, Ieda *et al.* [32] proposed a so-called three-dimensional (3D) Poole–Frenkel model that considers the barrier height in both the forward and reverse directions with regards to the applied electric field. The model yielded a consistent prediction of material conductivity at low and high electric field (in contrast, the conventional model is only applied for the high field limit). Further, Adamec and Calderwood [22] extended the theory for a coordinate system of three mutually perpendicular axes, one of which has the same direction as for the applied electric field. The field-dependent conductivity has been derived as:

$$\sigma = \sigma_0 \left(\frac{2 + \cosh\left(\beta_{PF}\sqrt{E}/2kT\right)}{3}\right)\left(\frac{2kT}{qE\lambda}\sinh\left(\frac{qE\lambda}{2kT}\right)\right), \tag{2.11}$$

where λ is the hopping distance or the trap site separation. The first term in eqn. (2.11) is associated with the field dependence of charge carriers' concentration, whereas the second term is due to the field dependence of mobility, the latter is close to 1 for the field strength up to 10^8 V/m and can be neglected. This model [22] provides more reasonable explanation of various experimental data on the field-dependent conductivity as compared to the original Poole–Frenkel model. Nath *et al.* [26], instead of modifying the charge injection (Schottky's) law or Poole–Frenkel mechanism, developed a theory accounting for the reduction of the trap depth caused by the field induced in materials. By applying the latter model, a good fitting of experimental data can be achieved and the trapping site separation and trap concentration can be found [26].

2.1.2. Charge transport

Transport of charge carriers in dielectrics is strongly controlled by the localized states existing in the materials. The localized states, which are also called traps, act as centers capturing charge carriers for certain time duration determined by their energy depth. Charges

captured in traps may acquire energy, for example from thermally-generated vibrations of polymer chains. If the acquired energy exceeds the barrier height of traps, the charge carriers are able to escape from them. Two types of traps, namely shallow and deep traps are commonly distinguished. The former trap type is attributed to structural defects in materials, such as folds, kinks, entanglements, or ends of polymeric chains. The latter trap type has chemical origin due to the presence of double bond (C=C) or reactive groups such as carboxyl (–COOH) as well as chemical impurities like acetophenone, alpha-mythylstyrene, *etc.* [33].

The distribution of localized states in the forbidden gap is usually strongly uneven. Dissado and Fothergill [29] proposed a schematic diagram for showing distributions of traps density and charge mobility with regard to electron energy. High density of traps is assumed in the vicinity of the conduction and valence bands, thus forming the tails of the bands. The trap site separation λ is usually in the range of few nanometers, corresponding to the trap concentration N of ~10^{25}–10^{26} m^{-3} (note that $N \approx \lambda^{-3}$) [26, 34]. Charges can be transferred between traps in close proximity either by hopping or tunneling mechanisms. In contrast, the trap concentration close to the center of the band gap is in many orders of magnitude lower and the charge transport between those traps is hardly possible. In other words, charge mobility is greatly reduced that results in the so-called mobility gap, whereas the sharp boundaries between the extended and localized states are so-called mobility edges. Charges transported between shallow traps are mobile carriers, thus contributing to the conduction current. On the other hand, charges trapped in the deep trapping centers for a considerably long residence time result in the space charges. A dynamic equilibrium between the charge transport and trapping is maintained in the materials.

2.1.2.1. Charge mobility

The transport of electrons and holes is featured by their apparent effective mobilities $\mu_{e,h}$ defined by the depth of shallow traps $\varphi_{e,h}$ as:

$$\mu_{e,h} = \mu_{b(e,h)} \exp\left(-\frac{\varphi_{e,h}}{kT}\right), \tag{2.12}$$

where $\mu_{b(e,h)}$ are band mobilities of the respective carriers. Here, the subscripts *e* and *h* denote electron and hole, respectively.

The effective mobility of charges can be found using different experimental techniques, for example by measuring space charge distribution (SCD), surface potential decay (SPD), and transient currents (TC). The first method relies on the determination of the average velocity of the charge front observed in the measured space charge distribution. The second technique is based on the theoretical derivation that the effective mobility is directly proportional to the potential decay rate and inversely proportional to the square of the applied electric field. The third approach is also called the time-of-flight method that considers the arrival of charge carriers to a counter electrode resulting in a broad peak in the transient current curve.

Charge carrier mobilities obtained experimentally for numerous polymeric insulating materials vary within the range of 10^{-15}–10^{-10} $m^2V^{-1}s^{-1}$, for several dielectrics the parameter

is even as low as 10^{-18}–10^{-16} $m^2V^{-1}s^{-1}$ [35]. Table 2.1 summarizes the charge carrier mobility attained for different morphologies of PE, the insulation being investigated most intensively. As seen, the parameter obtained in the majority of the studies is ~10^{-15}–10^{-13} $m^2V^{-1}s^{-1}$, except for a much higher value of ~10^{-8}–10^{-7} $m^2V^{-1}s^{-1}$ revealed by Tanaka and Calderwood [36], who utilized a rectangular impulse voltage for charging samples and then recorded a transient current through them. The condition used in the latter work [36] is different from that in the time-of-flight method, for which a DC voltage is generally employed. Results provided in Table 2.1 indicate that values of charge mobility in a similar material may be strongly different while being obtained in different methods and by different researchers. This distinction in the material property can be attributed to the variation in morphologies, impurity contents, experimental conditions, preparation methods, *etc.*

It is worthwhile to mention that charge mobility in insulating materials depends on both the applied electric field and temperature. In general, such a dependency can be described by a hyperbolic sinus function [23, 34]:

Table 2.1. Effective charge mobility in polyethylene (PE), low-density polyethylene (LDPE) and high-density polyethylene (HDPE). Different test methods were employed including measurements of surface potential decay (SPD), transient currents (TC) measurements, and space charge distribution (SCD).

Reference	Materials	Test method	Electric field, V/m	Temperature	Charge mobility, $m^2V^{-1}s^{-1}$
Wintle (1970) [37]	PE	SPD	$(2–20)\times10^7$	Room temperature (RT)	~10^{-15}
Perlman *et al.* (1976) [38]	LDPE	SPD	5×10^7	RT 21 °C	2×10^{-14}
Baum *et al.* (1977) [39]	PE	SPD	$(3–12)\times10^7$	Unspecified, probably RT	2.2×10^{-15}
Toomer and Lewis (1980) [40]	PE	SPD	$(2–10)\times10^7$	21°C	μ_h ~$(4–5)\times10^{-15}$ μ_e ~$(1.5–5)\times10^{-14}$
				31 °C	μ_h ~1.5×10^{-14} μ_e ~$(1–2)\times10^{-13}$
Berlepsch (1985) [34]	HDPE	SPD	$(2.5–11)\times10^7$	50 °C	$(1.5–13.3)\times10^{-15}$
			~8×10^7	22–75 °C	$(0.7–25)\times10^{-15}$
Tanaka and Calderwood (1974) [36]	PE	TC	$(2.7–8)\times10^7$	24–84 °C	$(2.4–10)\times10^{-8}$
Fischer and Röhl (1977) [23]	Oxidized LDPE	TC	$(0.2–1.8)\times10^7$	71 °C	$(2–6.5)\times10^{-15}$
Mizutani and Ieda (1979) [41]	HDPE	TC	4×10^7	70 °C	6×10^{-15}
			8×10^7		1.6×10^{-14}
Mizutani *et al.* (1980) [42]	HDPE oxidized HDPE oxidized LDPE	TC	4×10^7	60–80 °C	6×10^{-15}–1×10^{-13}
				70–84 °C	3×10^{-15}–6×10^{-14}
			10^7	40–80 °C	6×10^{-15}–8×10^{-13}
Pelissou *et al.* (1988) [25]	LDPE	TC	~10^7–10^8	21 °C	10^{-15}
Chen *et al.* (2001) [43]	LDPE	SCD	$(3–5)\times10^7$	RT	$(2–3)\times10^{-15}$

$$\mu \propto E^{-1} \sinh\left(\frac{q\lambda E}{2kT}\right). \tag{2.13}$$

Nevertheless, the field dependence is usually unpronounced at electric field of order of ~10^7 V/m that a constant mobility is sufficient for characterizing the parameter at a given temperature.

2.1.2.2. Charge diffusion

Diffusion also comes into play in the charge transport process. Diffusion is caused by a non-zero gradient of charge concentration, which may be essential, *e.g.* at the front of a propagating charge. The diffusion coefficient D_{dif} is linked to charge mobility via Einstein relation:

$$D_{dif} = \frac{kT}{q}\mu. \tag{2.14}$$

Thus, the density of the conduction current in general comprises two components, namely the drift and diffusion currents as presented by the first and second terms in eqn. (2.15)

$$j = q\mu nE - qD_{dif}\frac{\partial n}{\partial x}. \tag{2.15}$$

However, the contribution of the diffusion current to the total conduction current is usually small and can be neglected [44-46], so the conduction current density is commonly represented by the drift current only, as expressed in eqn. (2.1).

2.1.2.3. Trap energy

Determining the band structure and the trap depth in the forbidden gap has attracted a great interest among researchers. Investigations have been conducted using various methods including UV and X–ray photoemission, optical absorption, *etc.* A short review of the methods and obtained results can be found in [29]. It has been detected that a band gap is 8.8 eV for PE and the Fermi level is at the center of the gap, *i.e.* at 4.4 eV below the conduction band. In fact, the parameters have been revealed by using so-called internal photoemission on linear alkane hexatriacontane *n*–$C_{36}H_{74}$ instead of PE owing to the similarity in their hydrocarbon chain structures, see [29] and references therein. The edge of the conduction band is ~0.65 eV above the vacuum level, resulting in a negative electron affinity [47]. Measurements of optical absorption in PE, on the other hand, discovered a lower band gap of 7.35 eV [48]. Electron traps were found at ~1 eV and deep donors at 2–3 eV below the conduction band. The latters have been suggested to account for the generation of charges at high electric fields by Poole–Frenkel mechanism [48].

The trap depth in disordered solids has been also detected by measurements of TSD currents. For example, various trapping centers of energy depth in the range of 0.1–1.7 eV have been found in PE and attributed to defects in amorphous or crystalline phases and in their interface as well as to the presence of impurities such as oxidation by-products or cross-

linking agents [18]. The residence time of charge carriers in the deepest traps (1.7 eV) of the indicated range is in order of 5×10^{15} s, *i.e.* 1.5×10^{8} years! As a consequence, a considerable amount of space charges can be accumulated in the insulation bulk in spite of a low concentration of such deep traps.

Another approach for determining energies of traps was proposed by Simmons and Tam [49] and it is based on the concept of demarcation energy. The demarcation energy is the energy level below which all localized states are filled and above which all localized states are emptied. Since the trap density is proportional to the product of current and time $I{\cdot}t$ while the trap depth is proportional to $\log(t)$, the plot of $I{\cdot}t$ *vs.* $\log(t)$ represents the image of the energy distribution of trap density. This model has been utilized for deriving the property in numerous materials, including polystyrene [50], polypropylene [51], *etc.*

On the other hand, Meunier *et al.* [52, 53] employed the density functional theory (DFT) for defining the trap depth in PE due to the presence of both physical and chemical defects and impurities in the material. For keeping a reasonable computing time, linear alkane chains n–C_mH_{2m+2} with m = 13 and m = 10 were used in the respective works [52, 53] as modeled materials of PE. Again, the simplification was justified by the similarity in the chain structure of the selected alkanes and PE. While the conformational traps of physical nature at energy levels less than 0.3 eV were detected, the traps of chemical origin were much deeper and their trap depth varied in a wider range of 0.04–1.53 eV [52, 53]. It was also found that the trap density decreases exponentially with the trap depth [52, 53]. The results therefore support the assumption of the continuous trap energy distribution followed an exponential law [54].

2.1.3. Space-charge-limited current mechanism

The generation and transport of charge carriers in insulating materials have been described in the previous sections. In general, the imbalance between these processes occurs if the generation processes supply more charge carriers than their amount being transported through material bulk thus providing conditions for space charge accumulation. Under such circumstances, a local field enhancement may occur, which eventually violates the linear current–voltage relationship (Ohm's law). The conduction process is therefore governed by the space-charge-limited current (SCLC) mechanism, which is one of the most common mechanisms in insulating materials at high electric fields. In trap-free materials, the current–voltage dependence is followed the Mott–Gurney square law:

$$J_{tf} = \frac{9\varepsilon\mu V^2}{8L^3}, \tag{2.16}$$

where V is applied voltage and L is sample thickness. In material with traps, by assuming a constant ratio between the densities of mobile charges n_c and trapped charges n_t and denoting

$$\theta = \frac{n_c}{n_c + n_t}, \tag{2.17}$$

the current density can be expressed as:

$$J = \theta \frac{9\varepsilon\mu V^2}{8L^3}. \tag{2.18}$$

Note that the density of mobile charges is usually in several orders of magnitude smaller than that of trapped charges ($n_c << n_t$), thus $\theta << 1$ and the current density is greatly reduced as compared to the case of trap-free materials.

As the density of trapped charges reaches the total trap density, all traps are filled. The current density increases rapidly with a slope much larger than 2. This regime is called trap-filled voltage limit (TFVL). Thereafter, further increase of the applied voltage results in a square law dependency of the current–voltage relationship as for trap-free materials shown in eqn. (2.16). The current–voltage dependence of the described mechanism [20] is illustrated in Figure 2.3.

On the other hand, by considering an exponential distribution of traps in materials, Mark and Helfrich [54] found that the current increases with voltage faster than square law

$$J \propto \frac{V^{l+1}}{L^{2l+1}}, \tag{2.19}$$

where factor $l = T_C/T$, with T_C being the characteristic temperature of the proposed exponential distribution of the trap density and T indicating the absolute temperature (usually $T_C > T$, so $l > 1$). Such a dependence was found to be applicable for several polymers such as polyimide [55] which allows for obtaining the voltage corresponding to the onset of TFVL regime that is usually close to the breakdown voltage of materials. Using this approach, the trap density can be derived and is found to be in the order of 10^{23} m^{-3} for polyimide [55].

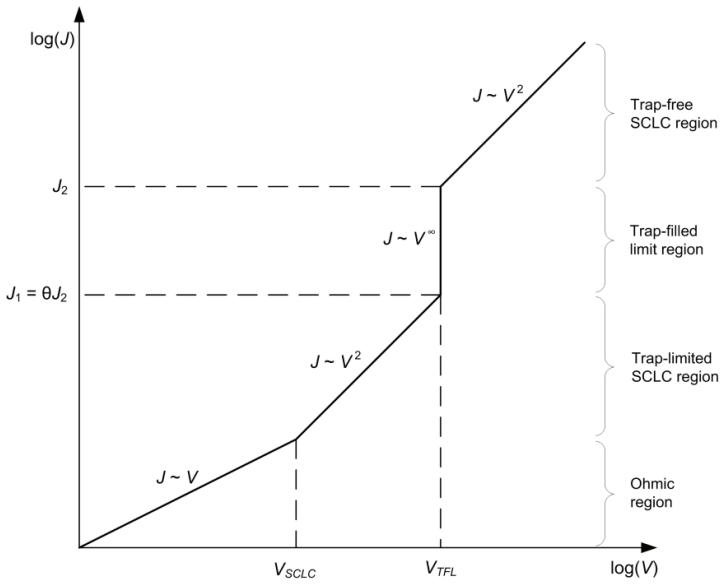

Figure 2.3. Current–voltage dependence for an ideal case of SCLC mechanism.

2.1.4. Effect of insulation–insulation interface on charge transport

Multi-layered insulating structures are inevitable in practice that the inherent insulation–insulation interfaces may greatly affect the conduction processes through the materials. Insulations of two neighboring layers in such systems are usually featured by different electrical properties. In general, a discontinuity in the ratio of material permittivity to conductivity ε/σ arises at the interface, yielding Maxwell–Wagner–Sillars (MWS) polarization, which is characterized by the accumulation of free charge carriers at the interface. In dielectric spectroscopy measurements, this process manifests itself by a relaxation peak in the loss (ε") curve of the considered materials. Note that insulating materials are usually operating at an electric field strength significantly higher than that used in the dielectric spectroscopy measurements and thus the influence of the interfaces can be more pronounced and, therefore, should be investigated.

Suzuoki *et al.* [12] measured conduction currents on single-layered ethylene-vinyl acetate (EVA), PE and multi-layered samples made of their combination. It is interesting to notice that the conduction currents for EVA and PE/EVA(+) are approximately two orders of magnitude higher than those for PE and PE/EVA(–). Here, (+) and (–) indicate the polarity of the DC voltage applied to the EVA layer. Taking into account that EVA is much more conductive than PE, the authors attributed the difference in the measured conduction currents for PE/EVA(+) and PE/EVA(–) to the difference in intensity of charge injection into EVA, *i.e.* it is significantly stronger at the anode than that at the cathode. After being injected, positive charges in EVA layer can penetrate through the interface that enhances the charge transport in PE layer. A certain amount of charges may also be accumulated at the PE/EVA interface, thereby resulting in the occurrence of additional peaks in the TSD current spectra of PE/EVA(+) as compared to those observed in PE/EVA(–) and EVA [12]. This hypothesis was latter on confirmed by Suh *et al.* [13], who measured space charge distribution in similar insulating structures utilizing pulse electro-acoustic (PEA) technique. The space charges accumulated at the interface can be explained by MWS polarization and charge trapping at localized states existing at the surface layer of the junction.

Space charge distributions were recently measured in double- and triple-layered samples of LDPE and LDPE/SiO_2 nanocomposite aiming at distinguishing the contributions of the charge injection and the charge transport to the accumulation of space charges in the insulation bulk [14]. For double-layered specimens, a test voltage was always applied to LDPE, the more conductive material as compared to LDPE nanocomposite, while the latter was in contact with grounded electrode. At room temperature, charges accumulated at the interface were found to be of the same polarity as the carriers injected into the more conductive layer (LDPE) and their presence was explained by the MWS polarization. At an elevated temperature (60 °C), the behavior of interfacial charges depended on whether positive or negative voltage was applied. In the former case, charges of both polarities were accumulated at the vicinity of the interface (positive charges on the side close to the anode, negative charges close to the cathode), while in the latter case only negative charges were observed. The authors [14] explained the observation by considering the band theory in multi-layered insulating structures. According to it, the interface between two dielectric layers plays a role as a blocking contact while applying a positive voltage to LDPE, otherwise the

interface is non-blocking. The proposed model also provided a reasonable explanation for the observation of space charges in triple-layered structures. The accumulation of charges at the interface between LDPE and its nanocomposites was also reported in other works [56, 57] and the observations were in most cases attributed to the MWS polarization.

In summary, the insulation–insulation interfaces exhibit the MWS polarization and can act as a blocking contact preventing the charge transport in multi-layered insulating structures.

2.2. Electrical properties of insulating materials under consideration

As mentioned above, two types of polymer-based insulating materials are utilized in this investigation, namely polyethylene-based nano-composites and micro-filled enamel insulations. A brief review of the properties of each component in the studied composites is provided here focusing on the electrical conduction processes.

2.2.1. Polyethylene-based nanocomposites

2.2.1.1. Polyethylene

Polyethylene is characterized by a simple hydrocarbon chain constituting a repeating unit $–CH_2–CH_2–$. The hydrocarbon chains are organized in order, giving rise to crystalline lamellae of 10–20 nm thick and ~100 nm wide. The planar lamellae build up in radial direction, yielding spherulites of diameter ~10 μm. The crystalline lamellae are separated by an amorphous phase of 5–10 nm thick comprising disordered chains, loops, kinks, and entanglements [58]. Thus, PE itself can be considered as a natural nanometric dielectric [59].

The material can be distinguished as low-, medium- and high-density, the crystalline degree of which increases from ~50% to ~90%. The mass densities are respectively 1.0 and 0.86 g/cm^3 for the crystalline and amorphous phases, resulting in the total mass density in the range of 0.91–0.94 g/cm^3 for the semi-crystalline polymer. While LDPE is characterized by high degree of branching, much fewer branches are presented in HDPE. This affects mechanical properties of the materials; in particular, LDPE has lower tensile strength and higher ductility than HDPE. The melting point of the material varies in a wide range of ~115–135 °C, with the lower limit corresponding to that of LDPE.

Although some properties of PE have been reported in the previous sections, they are outlined here for the sake of brevity. PE is characterized by a low DC conductivity of 10^{-14}–10^{-15} S/m that is associated with a large band gap of ~8.8 eV [58]. For such a band gap, the probability of exciting an electron from the valence band to the conduction band is almost zero. Charges can be generated in PE either at insulation–electrode interfaces via injection process or by excitation from donors and/or acceptors present in the bulk. Donors have been found at deep energy levels of 2–3 eV that can be excited by a high electric field. Physical defects in the amorphous region give rise to conformational traps located at ~0.15–0.3 eV below the conduction band edge [52], whereas the energy level of traps due to chemical defects are much deeper (up to 1.5 eV) [53]. Charges can be transferred to neighboring trapping sites by hopping or tunneling mechanisms. It has been suggested that due to the weak bonding of electrons to hydrocarbon chains and the negative electron affinity, the transport of electrons occurs most likely in the inter-chain paths rather than along intra-chains as for hole

transport [47, 60]. Ionic charge carriers can also be generated in PE by the dissociation of neutral molecules due to the presence of impurities and additives such as cross-linking agents. Note that transport of ionic charges is associated with mass transfer that is not the case for electronic type of charges, *i.e.* electrons and holes. Nevertheless, distinguishing the nature of charge carriers is not an easy and trivial task.

Mobilities of charge carriers in PE have been studied extensively [23, 25, 34, 36-43] and their dependencies on both the electric field and temperature have been established. An apparent charge mobility ~(10^{-14}–10^{-15}) $m^2V^{-1}s^{-1}$ has been commonly detected at room temperature for PE exposed to electric fields ~(10^7–10^8) V/m [34, 37-40, 43], see Table 2.1. It is worthwhile to note that electrons were found to be more mobile than holes: the mobility of electrons is usually few times (up to one order of magnitude) higher than that of holes [40, 43]. In contrast, holes are more likely to appear in PE rather than electrons [43]. Lewis and Llewellyn [47] attributed the charge transport in PE to the tunneling through amorphous phase and suggested that hole mobility reaches its maximum at a field strength beyond 10^8 V/m. The reduction of charge mobility at higher field, so-called negative differential mobility (NDM), has been detected in experiments [61]. The phenomenon was hypothesized as one of the causes of the formation of charge packets, *i.e.* repetitive and discrete generation of charge pulses, which have been observed experimentally in PE [61, 62].

2.2.1.2. Polyethylene nanocomposites

Introduction of nanofillers into PE greatly modifies the electrical properties of the material. Most importantly, a substantial reduction in DC conductivity [64-66] and a suppression of space charge accumulation [56, 66, 67] have been noticed. In a review published in 2005, Tanaka [8] argued that the insignificant accumulation of space charges is caused by the increased mobility of charge carriers that accelerates the charge transport through the materials. However, this hypothesis appears to be contradictory to the experimental evidences reported later on. In particular, the reduction in charge mobility in nanofilled PE as compared to that in the unfilled material has been underlined [64, 66]. Lewis [68] attributed this result to the hindering of the transition of electrons and holes during tunneling caused by the presence of nanofillers in the amorphous phase of PE. Another interpretation is related to the formation of deep trapping centers in PE nanocomposites [69]. These trapping sites are created at the interfaces of nanoparticles due to the difference in their dielectric permittivity compared to that of the polymer matrix. The deep traps can capture mobile charge carriers to form a thin layer of homocharges at the vicinity of electrodes. As a result, the electric field close to the electrodes is reduced, preventing further injection of charges into the bulk. This hypothesis has been verified by computer simulations that reveal substantial role of deep traps in suppression of space charge accumulation [70, 71].

It is worth noting that remarkable improvements in the properties have been reported for nanocomposites but not for micro-filled composites. As an example, while introduction of nanofillers into PE leads to a great reduction of DC conductivity, the opposite tendency was found when using fillers of micrometer size [64, 65]. In fact, the properties of composite materials are strongly governed by the size of the filler particles that determines the surface area of filler–polymer interfaces per unit volume. The specific surface area can be as large as

several square kilometers per cubic meter in nanofilled materials [72], but it is several orders of magnitude lower for microcomposites. Compared to both the fillers and the base polymers, the interfacial region in nanocomposites may have remarkably different properties that play a deterministic role in characteristics of nanofilled materials. Based on this, Tanaka *et al.* [72] proposed a multicore model that emphasizes the formation of three layers (*i.e.* bonded, bound, and loose layers) around inorganic fillers. Using this model, the authors [72] successfully explained various modifications in electrical properties of polymeric nanocomposites. Also, Lewis [68] pointed out that only nanofillers can be introduced into the inter-lamellae regions because the latter is of nanometer size, while microfillers cannot. Thus, nanofillers rather than microfillers block the charge transport in PE.

2.2.1.3. Inorganic fillers

Aluminum oxide (Al_2O_3) and magnesium oxide (MgO) were used in this investigation as fillers for manufacturing nanocomposites. Both materials are good electrical insulators characterized by large energy band gaps and low DC conductivities. Relative permittivities of the oxides are much higher than that of PE (which is commonly accepted to be 2.3). The characteristics of the oxides are provided in Table 2.2.

2.2.2. Enamel insulations and inorganic fillers

2.2.2.1. Properties of enamels

As mentioned above, the insulation of enameled wires usually constitutes a multi-layered structure consisting of at least two layers, a base coat and a top coat. The materials used for these layers are usually polyester-imide (PEI) for the former and polyamide-imide (PAI) for the latter. They are high temperature materials with stable thermal properties. The glass transition temperature (T_g) of both materials is approximately 270 °C [77, 78].

The dielectric permittivity of PAI has been reported in [77] for a wide range of temperatures (from –100 °C to 400 °C) and frequency (10^{-1}–10^{6} Hz). At temperatures below 200 °C, the real part of the complex permittivity varies from 4 to 4.5 depending on the frequency of the applied voltage. For temperatures close to T_g, the real part of the complex permittivity increases rapidly with reducing frequency. The DC conductivity of PAI has been derived in [77] from the AC conductivity measured at 0.1 Hz. At 250 °C, the obtained DC conductivity is ~10^{-11} S/m. For temperatures above T_g, the DC conductivity of the material exhibits nonlinear temperature behavior.

Limited information about the dielectric properties of PEI is available. The measurements performed in a frequency range of ~10^{1}–10^{5} Hz [78] showed that the real part of the complex

Table 2.2. Material properties of the inorganic oxides.

Material	Al_2O_3	MgO
Energy band gap, eV	~7–9 [73] and references therein	7.8
DC conductivity at RT, S/m	~3×10^{-16} [74]	~10^{-12} [75]
Relative permittivity, 1	9.6 (at 1 MHz) [74]	9.7 (at 10 GHz) [76]

permittivity increases monotonously from 4.2 to 5 with decreasing frequency, the loss factor ($\tan\delta$) is ~10^{-2} and it is characterized by two loss peaks at ~10^2 Hz and 10^5 Hz.

2.2.2.2. Properties of chromium oxide

For microfilled composites such as the enamel insulation considered in this work, the contribution of filler–polymer interfacial regions to the effective material properties is not as pronounced as for nanocomposites. The effect of filler properties, on the other hand, is more important. Thus, the detailed description of electrical characteristics of chromium oxide fillers is provided in this section.

Chromium (III) oxide Cr_2O_3 is widely used as a pigment in the paint industry due to its characteristic dark green color. Being added to enamel insulation it provides the material with the same hue. Volume DC conductivity of chromium oxide was reported in several works, for example [79-82]. Crawford and Vest [79] described two conduction mechanisms of chromium oxide crystals, namely defect-controlled and intrinsic conductions. The defect-controlled mechanism occurs below a characteristic temperature (~1000 K), and is affected by external conditions. It is caused by defects in material crystals that generate charge carriers by reaction with oxygen. Consequently, the electrical conductivity strongly depends on the partial pressure of oxygen. On the other hand, the intrinsic mechanism is observed above the characteristic temperature and is unaffected by external conditions. In such a case, the conduction is induced by charge transfer between ions (Cr^{3+} and O^{2-}) through the formation of an electron–hole pair. The experimental results showed that in the temperature range of 600–1400 °C, the electrical conductivity is as high as 10^{-2}–10^{1} S/m for chromium oxide crystals in oxygen at pressures of 10^{-2} to 1 atm [79]. Further, the volume conductivity of material in the form of thin films strongly depends on temperature and sample thickness [80]. The conductivity increases significantly with increasing temperature, whereas it decreases dramatically with increasing material thickness. As an illustration, the DC conductivity of a 125 nm thick film at 25 °C is ~1 S/m and it is ~10^{-6} S/m for the mm thick Cr_2O_3. Gas medium and its pressure also affect the measured volume conductivity of chromium oxide. For instance, it is increased considerably in oxygen environment as compared with the case of vacuum.

The conductivity measurements reported in [81] performed at high temperatures (200–500 °C) for chromium oxide powder used as a catalyst. Experiments were conducted in different gas media and showed that the volume conductivity varied in a range of 10^{-9}–10^{-7} S/m for vacuum, 10^{-8}–10^{-6} S/m for hydrogen environment, and it was significantly higher (10^{-5}–10^{-2} S/m) for oxygen medium. Besides, the values of 10^{-1}–10^{1} S/m were recorded for porous specimens immersed in oxygen at temperatures 550–1300 °C [82]. The variations in the magnitudes of the volume conductivity of the material in vacuum, hydrogen, and oxygen were explained by differences in conduction mechanisms and types of charge carriers. Accordingly, positive charge carriers (holes) were suggested to be dominant in the material exposed to oxygen whereas negative carriers (electrons) were assumed to be prevalent in hydrogen medium.

The relative permittivity (the real part of the complex permittivity) of chromium oxide was measured in [83] using a single crystal of 6 mm in diameter and 0.5 mm in thickness at

room temperature (25.5 °C). Since the material has the corundum structure (hexagonal system) [79], the relative permittivity is anisotropic and it was determined for two directions, namely directions parallel to *a* axis and parallel to *c* axis. The relative permittivity value of 13.3 was recorded at 1 kHz and 13.0 at 2 MHz for the first direction, whereas it was 11.9 at 1 kHz and 11.8 at 2 MHz for the second direction. Furthermore, the relative permittivity was found to be weakly dependent on temperature and the magnitude of the temperature factor was found to be ~10^{-3} K^{-1} in the range of 25–52 °C. In summary, the average value of the relative permittivity of chromium oxide is around 12–13 at the indicated frequencies.

2.3. Computer simulation of electrical conduction in insulating materials

Accumulation of space charges in polymeric insulations exposed to a DC electric field is the main concern during the operation of electrical devices and components. It may greatly enhance the electric field inside the insulation bulk that eventually has a detrimental effect on the life expectancy of insulations. Thus, knowledge of the generation and transport of charge carriers plays an important role in designing reliable insulation systems. Apart from various experimental techniques used to assess charge dynamics in insulating materials, computer simulations have become popular since they offer great flexibility in investigating effects of different factors and in conducting parametric studies.

Teyssedre and Laurent [84] in 2005 summarized attempts in developing computer models of charge generation and transport in insulating materials from molecular to macroscopic scales. Apart from providing an in-depth analysis of various models available, the authors [84] also pointed out the challenges should be dealt with in order to fill the gap of knowledge in the topic. Within the scope of this thesis, we concentrate only on the second aspect, *i.e.* in the macroscopic scale. The most significant works including those implemented recently are listed in Table 2.3 with the main focus on PE used as cable insulation. A pioneering computer model considering transient processes of charge generation and transport in insulations exposed to a DC stress was published in 1994 by Alison and Hill [44] with the aim of reproducing the space charge accumulation attained experimentally [85] on a 2.5 mm thick sample of cross-linked polyethylene (XLPE). The model incorporated a constant source for charge injection at insulation–electrode interfaces and charge transport through the bulk associated with trapping and recombination, while de-trapping was not considered. Since that time, a variety of models [45, 46, 86-92] have been developed for studying different physical processes taking place in insulations under a high DC electric field. Unlike the earlier proposed model [44], Schottky's law is usually used for implementing charge injection. Le Roy *et al.* [46] proposed a model accounting for the de-trapping of charges from deep trapping sites (in contrast to earlier works [44, 86, 87]) that yielded consistent prediction of experimental results on space charge distribution, conduction currents, and electroluminescence in LDPE. Furthermore, Boufayed *et al.* [45] introduced the more realistic exponential distribution of traps instead of two single trap levels (shallow and deep traps) utilized in other models [44, 46, 86, 88]. Most recently, the contribution of surface states at the interfaces between dielectrics and electrodes to the dynamics of space charges in LDPE films has been considered [91]. Additionally, the formation of charge packets arising as the applied electric

field exceeds 100 kV/mm has been studied [87, 92]. The model [92] is implemented by assuming a hysteresis loop in the injection process (so-called switching model) or NDM,

Table 2.3. Works on simulation of charge transport in insulating materials in chronological order. The models classified as "fitting" reproduce experimental characteristics while those "analyzing" focus on analyzing charge transport and accumulation without fitting the experimental data.

Reference	Main features and/or outcomes	Type	Material samples	Temperature
Alison and Hill (1994) [44]	a constant source for charge injection, a constant charge mobility, including charge trapping and recombination	fitting	degassed XLPE 2.5 mm thick	unspecified, most likely RT
Fukuma *et al.* (1994) [86]	Schottky's law for charge injection	fitting	degassed XLPE 2.5 mm thick	unspecified, most likely RT
Fukuma *et al.* (1995) [97]	introducing a potential barrier at an internal interface	fitting	double-layered XLPE 2.0 mm thick	unspecified, most likely RT
Kanoke *et al.* (1999) [87]	formation of charge packets at an electric field of 130 kV/mm	analyzing	oxidized XLPE films 100 µm thick	RT (300 K)
Sahli *et al.* (2003) [94]	modeling the decay of surface potential on corona charged insulation, assuming instantaneous charge injection from the charged surface and the field-dependent mobility	fitting	polypropylene films 50 µm thick	RT
Le Roy *et al.* (2004) [88]	introducing the charge de-trapping; simulating the space charge accumulation, conduction currents, and electroluminescence	analyzing	LDPE films 150 µm thick	RT
Le Roy *et al.* (2006) [46]	considering the charge de-trapping; fitting experimental results of space charge accumulation, conduction currents, and electroluminescence	fitting	LDPE films 150 µm thick	RT
Boufayed *et al.* (2006) [45]	introducing the exponential distribution of traps and the field-dependent mobility	fitting	LDPE films 150 µm thick	RT
Serdyuk *et al.* (2006) [89]	analyzing the space charge distribution in a cable insulation subjected to the polarity reversal of DC voltage	analyzing	cable insulation PE, thickness 3.5 mm	RT
Chen (2010) [96]	modeling the decay of surface potential on corona charged insulation; assuming bipolar charge injection followed Schottky's law	analyzing	LDPE films 50 µm thick	RT
Le Roy *et al.* (2013) [90]	analyzing the electric field distribution and the space charge distribution in a cable insulation subjected to isothermal and temperature gradient	analyzing	cable insulation, thickness 1.5 mm	isothermal and thermal gradient conditions
Taleb *et al.* (2013) [91]	considering surface states as interfacial layers of 1 µm thick that have higher trap depth and trap density; assuming the exponential distribution of traps and the field-dependent mobility	analyzing	LDPE films 200 µm thick	RT
Baudoin *et al.* (2014) [92]	analyzing the formation of charge packets at electric field 130 kV/mm	analyzing	LDPE films 150 µm thick	RT
Zhang *et al.* (2014) [70]	a parametric study for analyzing the space charge distribution within the first 10 min after voltage application	analyzing	LDPE/MgO nanocomposite	RT
Lean and Chu (2015) [98]	developing a 3D 'particle-in-cell' model of charge transport in ferroelectric nanocomposites; considering charge attachment/detachment to/from nanofillers instead of charge trapping/detrapping	analyzing	PVDF/$BaTiO_3$ nanocomposite, cubic cell of 1 μm^3	RT
Min *et al.* (2015) [71]	a parametric study for analyzing the conduction current and space charge distribution	analyzing	LDPE nanocomposite	RT (297 K)

which are featured by an abrupt change at a threshold field strength either of barrier height for charge injection at anode or of hole mobility. The effect of the interface between two dielectric layers on the charge transport process has been studied by Fukuma *et al.* [86], who ascribed a barrier height for characterizing the blocking effect at the interface. This potential barrier is quite low (0.1 eV) and for non-blocking contact its value should be set to zero.

As for the decay characteristics of surface potential on insulating materials, a variety of mathematical models [34, 37, 40, 93] was developed early for elucidating experimental data. Most of the models yield mathematical expressions of the potential decay, but they are usually applicable only for the time shorter than the transit time, *i.e.* the duration for the charge front traversing through the sample thickness. Sahli *et al.* [94], on the other hand, treated the problem in the entire measuring time by using a computer model for reproducing the potential decay characteristics on 50 μm thick polypropylene films. The hypothesis of charge injection from the open surface where charges deposited and the concept of the field-dependent mobility developed earlier [34, 93] were used in the model. The authors [94] pointed out that charge de-trapping from deep traps should be included in the model in order to provide the best fitting with the experimental data. Most recently, experimental evidences of charge injection from a counter electrode in contact with ground into PE samples during potential decay were shown [95]. The feature was later on introduced into a numerical model of charge transport in PE for explaining measured potential decay [96]. Such model is known as the bipolar charge injection model, which distinguished itself from the earlier developed mathematical models [34, 37, 40, 93] considering unipolar charge injection only from the air–insulation interface.

It is worth noting that most of the reported simulations were performed for ambient temperatures ~20 °C, which is not the practical working condition of insulations. The actual operating temperatures are usually higher and depend on the application. For example, it may reach 70–80 °C for the insulation of HVDC cables. Moreover, a temperature gradient across the insulation may exist, which affects local characteristics of the material relevant to charge transport. These facts raise a question on the applicability of the existing models for predicting the behavior of insulations in practical situations. This difficulty, in fact, has been dealt with in [90], where the distribution of the electric field and space charges in a cable working under isothermal and temperature gradient conditions were modeled by assuming dependencies of charge carriers' mobility on temperature and electric fields while setting all other model parameters the same as in [46]. The simulated results, however, have not been confirmed by respective experimental data yet.

Simulation of charge transport in nanocomposites is rather limited. To formulate a consistent model for this case, the model of charge transport in pure polymers needs to be extended to account for the formation of traps associated with nanofiller particles. These trapping sites may stimulate specific processes which are not present in pure materials. In particular, the formation of deep traps that capture mobile carriers injected from electrodes, thus preventing further generation of space charges at electrode–material interfaces has been introduced in [69]. One of the approaches is employing the models described above for unfilled polymeric materials taking into account the effective medium approximations of properties of the composites. This has been implemented in [70, 71] utilizing parametric

studies to examine different hypotheses as well as to compare contributions of different elementary processes to charge transport. The model outcomes of these works [70, 71] have not been compared with measured results. Alternatively, Lean and Chu [98] developed a 3D 'particle-in-cell' model of charge transport in polyvinyl-idene fluoride (PVDF) based nanocomposite filled with ferroelectric nanoparticles of $BaTiO_3$. Charge trapping and de-trapping were not considered in the model, instead the attachment/detachment of charges to/from nanoparticle surfaces due to the electrostatic force were assumed. Charge carriers generated in the material were transported along different trajectories depending on the orientation of dipoles with respect to the applied field. Charge accumulation at filler surfaces was observed which is similar to the trapping of charges at the interfacial region between the fillers and polymer matrix. The macroscopic outcome of the model is the time-varying conduction current, magnitude of which depends on the amount of charges reaching counter electrode without being attached to nanofillers. Due to the complexity of the model, the conduction current was obtained within only a short duration (20 s) and this result needs to be validated by matching with experimental data. This topic therefore requires further investigations.

3. Material samples and methods

This chapter provides a description of the used material samples and the experimental arrangements and procedures implemented for investigating their electrical properties. It is followed by an outline of a numerical model of charge generation and transport in insulating materials, which is later on employed for reproducing and analyzing the experimental results. Note that the materials were manufactured at the Department of Fibre and Polymer Technology, Royal Institute of Technology, Sweden.

3.1. Material description and sample preparation

3.1.1. Low-density polyethylene and its nanocomposites

Nanocomposites were prepared using two types of metal-oxide nanofillers, namely alumina (Al_2O_3) and magnesia (MgO). The Al_2O_3 particles had spherical shape with an average diameter of 40 nm, whereas the MgO nanoparticles were in rounded hexagonal shape with an average size of 66 nm and a thickness of 10–20 nm. The transmission electron microscopy image of the Al_2O_3 nanoparticles is illustrated in Figure 3.1, whereas the size distribution of the particles is shown in Figure 3.2. For preparing nanocomposites, a certain amount of nanoparticles and Irganox 1076 (used as antioxidant) were dispersed in heptane solvent and the suspension was added into LDPE powder. The obtained mixture was then shaken for 1h and dried in an oven at 80 °C to evaporate all the solvent. Finally, the dry mixture powder was compounded by thermal extrusion at 150 °C in 6 min. The obtained materials were later on hot pressed at temperature of 130 °C using a force of 200 kN for 20 min to form film samples of 80 μm or 155 μm thick that have square shape with a side of 65 mm. The prepared samples were then kept in a desiccator for preventing the intake of moisture from laboratory air.

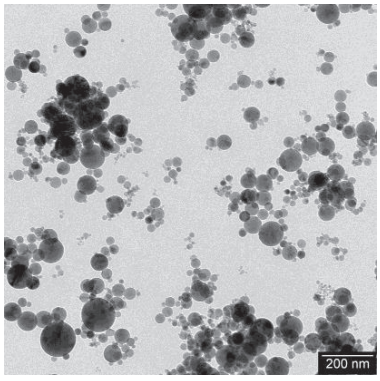

Figure 3.1. Transmission electron microscopy image of Al_2O_3 nanoparticles.

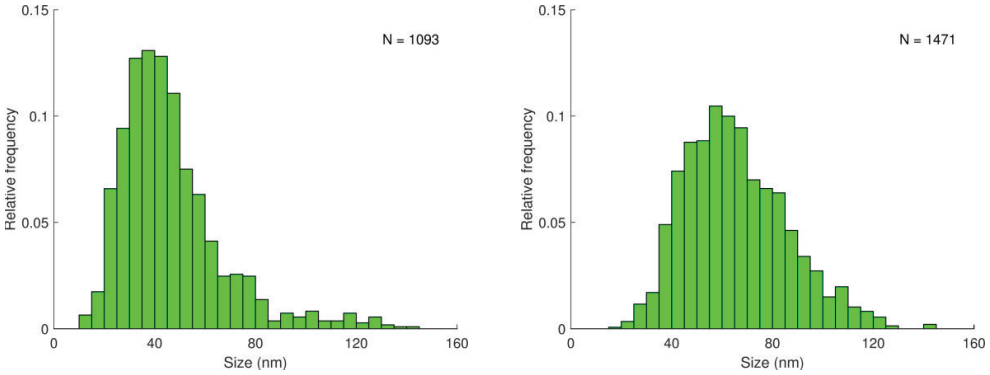

(a) Al_2O_3 particles (diameter) (b) MgO particles (longest cross sectional distance)

Figure 3.2. Size distribution of the nanoparticles. *N* is the total number of particles under consideration.

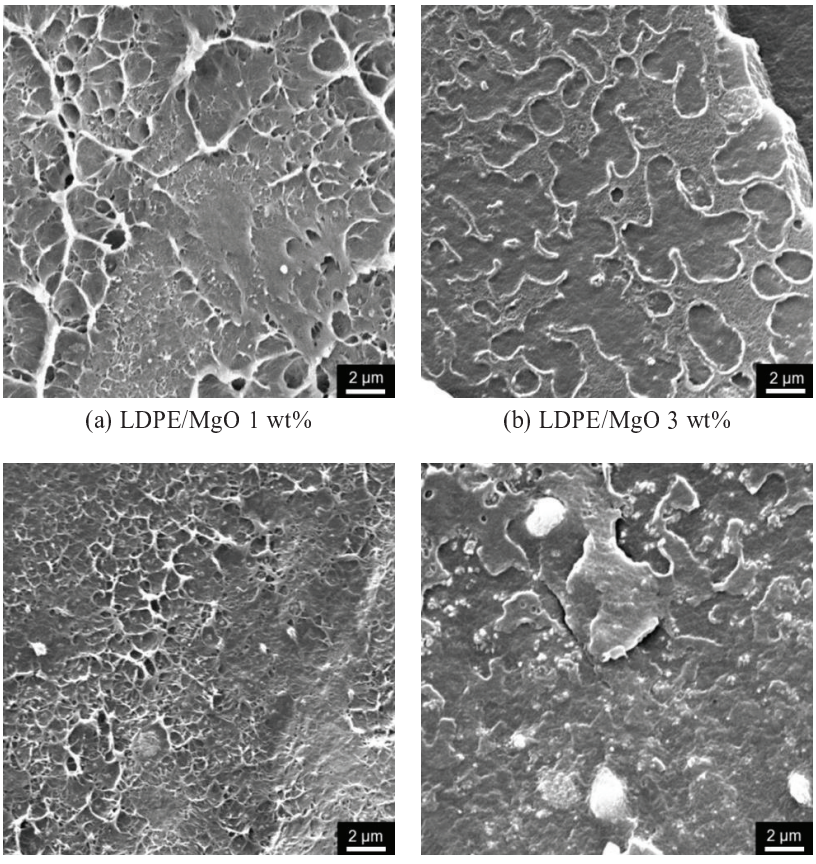

(a) LDPE/MgO 1 wt% (b) LDPE/MgO 3 wt%

(c) LDPE/MgO 6 wt% (d) LDPE/MgO 9 wt%

Figure 3.3. Scanning electron micrographs of LDPE/MgO nanocomposites at different contents of nanofillers.

To study the influence of filler content on material properties, four nanocomposites filled with Al_2O_3 at 1, 3, 5, and 10 wt% as well as five sets of MgO-filled materials with filler content of 0.1, 1, 3, 6, and 9 wt% were prepared. All the materials contained the antioxidant at 0.02 wt% for avoiding degradation by oxidation. Scanning electron micrographs are

demonstrated in Figure 3.3 for LDPE/MgO nanocomposites at different contents of nanofillers. As seen, nanofillers were evenly distributed in LDPE matrix at filler contents up to 3 wt% while at high amounts of fillers, in particular at 9–10 wt%, clustered and agglomerated particles were observed. While the clusters only consisted of several nanoparticles and were less than a micrometer in cross-section, the agglomerates could be several micrometers large and were built up of thousands of nanoparticles. Detailed information on the inter-particle distances and sizes of agglomerates is presented in [99].

3.1.2. Enamel insulations

The insulation coating of an enameled wire usually constitutes a multi-layered structure consisting of at least two layers, for example a polyester-imide (PEI) base coat and a polyamide-imide (PAI) top coat. An individual layer is manufactured by passing the wire through a coating bath with appropriate insulating resin several times until a predefined thickness is reached. Usually, each such passage results in an increase of the thickness by ~5 μm [100]. Thus, each coating layer comprises a number of thinner sheets of the same material.

The cross sections of two types of enameled wires used in the present study are presented in Figure 3.4; one with conventional insulation and the other one with the insulation filled with chromium oxide (Cr_2O_3) powder. The former consists of three layers (a PEI base coat, a PAI over coat, and a modified aromatic polyamide (PA) bonding coat), whereas the latter has two layers (a PEI base coat and a PAI top coat). To form the top coat of the filled enamel, chromium oxide micro-particles were added at the amount up to 26 wt% (equivalent to 8.7 vol%). The size of Cr_2O_3 particles varied between 0.2 and 2 μm and the average size was 0.74 μm. The conductor diameters were 1.18 mm for both wires, while the insulation layers were 50 and 40 μm thick for the conventional and filled enamels, respectively. The base and the top coating layers of the filled enamel were respectively ~25 μm and ~15 μm thick, whereas similar parameters of the conventional one were unknown.

Flat materials samples were also used in the experiments. They were created by depositing a thin insulation layer on top of a copper substrate having a square shape with a side of 100 mm and of 1 mm thick. Two types of insulations were used, namely PAI resin without any fillers and PAI resin containing chromium oxide filler at 14.3 wt% (equivalent to 4.3 vol%). The insulation thickness was 38 and 19 μm for the PAI and Cr_2O_3-filled PAI layers, respectively.

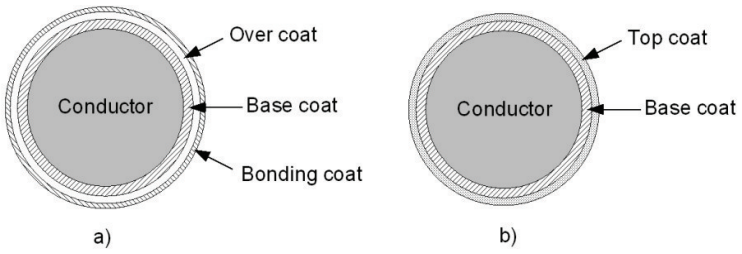

Figure 3.4. Cross sections of (a) conventional and (b) filled enameled wires.

3.2. Experimental techniques

3.2.1. DC conductivity measurements

Measurements of DC conductivity were carried out by using a three-electrode system following a standard procedure [15]. The arrangement of the experimental setup depended upon the geometry of the samples used, as described below.

3.2.1.1. Experiments on LDPE and its nanocomposites

The test setup for experiments on LDPE and its nanocomposites is shown in Figure 3.5. The DC test voltage was generated by a power supply from Glassman (model FJ60R2) and the current was measured using an electrometer Keithley 6517A. The high voltage electrode was a stainless steel cylinder with a diameter of 45 mm, the measuring electrode was 30 mm in diameter, whereas the guard ring allowed for eliminating surface currents. A good contact of the high voltage electrode to the sample was provided by placing between them a layer of conducting silicon rubber (SIR) Elastosil 570/70 having DC conductivity of 28 S/m. The use of the SIR electrode in the measurements resembles the operating conditions of cable insulation that is always in contact with a semiconducting layer.

An oven was used for controlling temperature levels at which the measurements were conducted. In addition, the metallic walls of the oven were grounded constituting a shielding box for avoiding electromagnetic disturbances. Thermal equilibrium at a predefined elevated temperature was attained by keeping the setup inside the oven for ~2h prior to each test. Thereafter, a DC voltage was applied to the high voltage electrode and the current was recorded. Unless otherwise stated, an electric field of 32.5 kV/mm was applied to the samples. The measured data were collected and stored in a personal computer via a data acquisition card (DAQ). Each test was repeated 2–3 times for checking the reproducibility of the results.

3.2.1.2. Experiments on enamel insulations and Cr_2O_3 fillers

DC conductivity measurements on the flat sample of PAI with and without fillers were conducted using a similar setup as described above. On the other hand, for measurements on

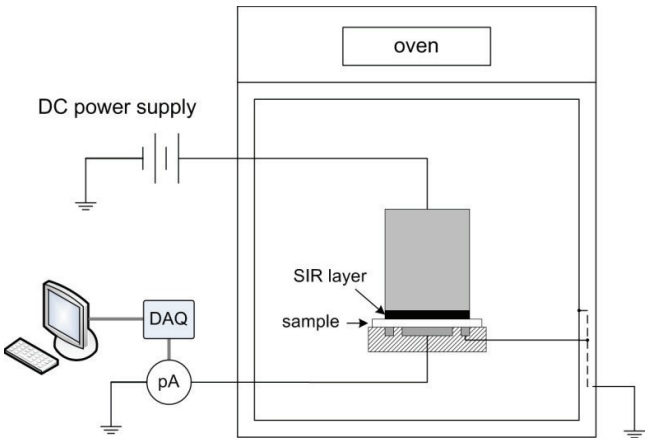

Figure 3.5. Schematic illustration of the test setup for conductivity measurements. DAQ stands for data acquisition card and pA denotes the electrometer.

insulations of enameled wires, a three-electrode system was especially designed. In particular, the high voltage was supplied to the wire conductor, whereas the measuring and the guard electrodes were made of conductive copper tapes attached to the external enamel layer. The measuring and the guard electrodes were 4 cm and 1 cm in length, respectively. The circuit diagram of the setup for measuring DC conductivity of the enamel coating is schematically illustrated in Figure 3.6. The electrode arrangement was placed in a metallic grounded box, which also allowed for controlling temperature and humidity during the measurements. Test temperatures were achieved by using a heater and a thermostat, while a relative humidity was maintained in the range of 30–40% by a saturated salt solution placed inside the test box.

The measurements were also conducted on chromium oxide powder. For this, a specialized test cell (Figure 3.7) resembling the three-electrode system was used. It consisted of two concentric stainless steel cylinders and a guard ring. The inner cylinder acted as the high voltage electrode, while the measuring and the guard electrodes were located in the bottom of the outer cylinder. The diameters of the energized and the measuring electrodes were 30 mm and 13.1 mm, respectively. The investigated powder was first dried at 120 °C for 24 h, and then poured into the cell to form after pressing a thin layer (~1 mm thick) between the voltage and the measuring electrodes.

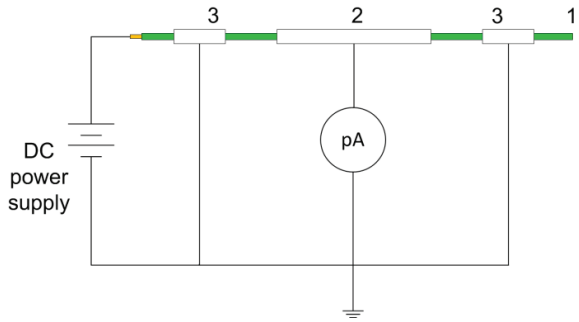

Figure 3.6. Circuit for measuring DC conductivity of enamel coating: (1) enameled wire, (2) measuring electrode, (3) guard electrode.

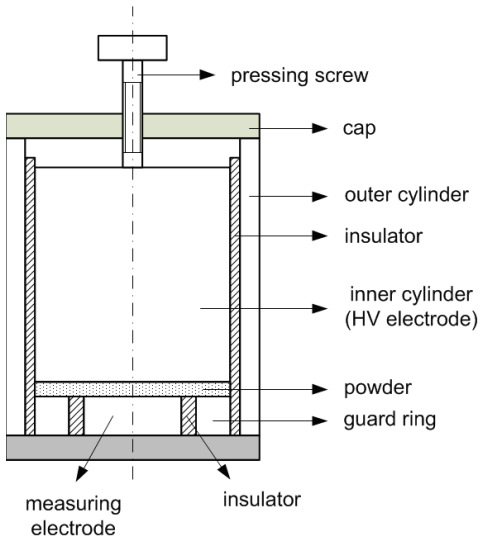

Figure 3.7. Schematic diagram of the test cell for measuring dielectric properties of powder.

3.2.2. Dielectric spectroscopy measurements

The dielectric spectroscopy measurements were carried out only on the enamel coating and chromium oxide. For the enamel wires, a three-electrode system resembling that in Figure 3.6 was made. Unlike the electrodes for DC conductivity tests, the external electrodes were created in this case by depositing thin layers of silver paint for eliminating the influence of glue layer in the conductive tape on the relative permittivity and the loss. After being prepared, the samples were dried at 100 °C during 4h for eliminating the effect of moisture in the silver paint on the results. The measurements were conducted in the frequency range from 1 mHz to 1 kHz by means of an Insulation Diagnostic System IDAX 300. A shielding box was employed for reducing the influence of parasitic capacitances between a sample and the ground potential on the measured capacitance as well as for maintaining temperature and relative humidity at predefined levels during the experiments. Thermal equilibrium inside the shielding box was achieved by keeping it in an oven for ~2h. Thereafter, the experiments were carried out by applying an AC voltage of 100 V_{rms}. The material complex permittivity was obtained by dividing the measured complex capacitance by the geometric capacitance of the electrode system. Besides, experiments on chromium oxide powder were performed using the test cell shown in Figure 3.7 and an applied voltage up to 4 V_{rms}.

3.2.3. Surface potential decay measurements

3.2.3.1. Experiments on LDPE and its nanocomposites

The experimental setup for SPD measurements is schematically illustrated in Figure 3.8. During the experiment, one side of the film samples remained in contact with a grounded copper plate, while the other side was initially exposed to corona discharge in air for 10 s. The corona was generated in a triode electrode system [101], which consisted of a needle and a grid electrodes connected to DC voltage sources. The use of the grid electrode allowed for uniform charging of sample surface as well as for controlling the level of potential on the charged surface. The magnitude of the voltage applied to the grid was selected so that the initial electric field induced in the samples by the deposited charges was close to the electric field applied during the conductivity measurements. The surface potential induced by deposited charges was measured by means of a non-contact technique [102] using a Kelvin probe placed above the sample surface. The probe was connected to an electrostatic voltmeter (Trek model 347B). The positions of the corona triode and the probe were controlled by a positioning system. Surface potential was continuously monitored at the center of the sample and potential distribution was regularly checked by scanning the surface, *i.e.* by moving the probe above the surface along a line passing through the center of the sample. The data were stored for further analyses by using LabVIEW software.

The SPD measurements were conducted on both LDPE nanocomposites filled with 3 wt% of nanoparticles as well as on the reference material at different temperature levels. For test at elevated temperatures, the sample heating was realized by means of a hot plate on which the grounded copper plate rested. Prior to each measurement, the sample was preconditioned at a targeted temperature for ~4h, thus assuring that homogeneous temperature distribution was achieved in the tested thin film.

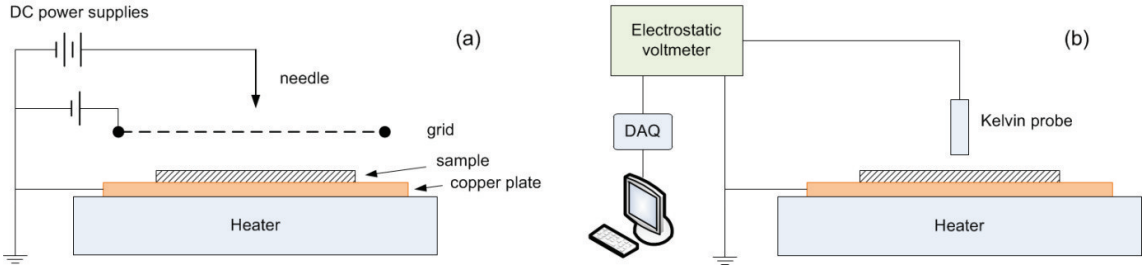

Figure 3.8. Schematic illustration of the setup for (a) corona charging and (b) surface potential decay measurements.

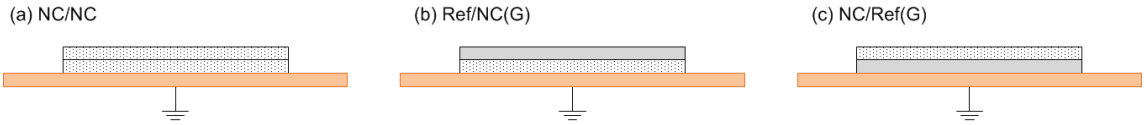

Figure 3.9. Multi-layered sample structures used in SPD measurements: (a) *NC*/*NC*, (b) *Ref*/*NC*(*G*), and (c) *NC*/*Ref*(*G*). *Ref* and *NC* denote respectively the reference LDPE and LDPE/Al_2O_3 3wt% nanocomposite, whereas index (*G*) indicates the layer in contact with the grounded copper plate during the test.

The SPD measurements were also conducted on multi-layered sample structures. For this, three specimen configurations, *i.e. NC*/*NC*, *Ref*/*NC*(*G*), *NC*/*Ref*(*G*) as illustrated in Figure 3.9, were used. The initial electric field induced inside the insulation was kept at the same level as for the measurements on single-layered samples by increasing the voltage applied to the grid electrode. Since surface potential exceeding 3 kV should be detected, a Trek electrostatic voltmeter model 341B was utilized which allowed for measurements up to 20 kV. The tests were conducted at room temperature only by following the same experimental procedure as described earlier. Each SPD measurement was performed 2–3 times for checking the repeatability of the results.

3.2.3.2. Experiments on enamel insulations

Samples used in SPD measurements were prepared as windings with wires positioned closely (turn to turn) around a wooden plate (100 mm×50 mm×6 mm). The sample windings consisted of 40 turns providing surface area of 50 mm×50 mm as shown in Figure 3.10a.

Owing to the complicated geometry of the sample used, the effects of surface charges, *i.e.* the electric field in materials and the potential induced by deposited charges, were calculated and compared with those corresponding to a flat sample (Figure 3.10b). The calculations were performed for samples of the conventional enamel utilizing COMSOL Multiphysics. For this, a surface charge of the density 10^{-6} C/m^2 was assumed to be presented on the gas–insulation interfaces in both systems, while the insulation–metal interfaces were grounded. As dielectric properties of layers of materials differ slightly, the enamel coating was simulated as a single layer of 50 μm in thickness and having relative permittivity of 3.5 (close to the value measured at 1 kHz for the conventional enamel, see section 5.2.1). Thus, the average calculated electric fields in the insulation were ~3.3×10^4 V/m in both cases. The electric field

profiles along straight lines perpendicular to the gas–insulation interfaces are provided in Figure 3.11. As can be seen, a small deviation (max. ~8.5%) was observed. In addition, the induced surface potentials were respectively 1.680 and 1.613 V for the winding and flat samples, yielding a discrepancy of 4.1%. Hence, the winding samples (Figure 3.10a) used in SPD measurements can be considered using equivalent flat samples (Figure 3.10b) with the identical insulation thickness.

A similar measurement system as used for the experiments on LDPE-based samples was utilized. A sealed plastic box was employed for keeping relative humidity stable in the range 25–35%. The winding surface was charged by DC corona of either polarity generated from a needle electrode. The sample was placed on a grounded copper plate and the wire conductor was always grounded during the test. To study the effect of electric field on material properties, three charging levels, varying from 3 to 4.5 kV, were employed. Unlike the measurements on LDPE-based materials, the tests on enamel insulations were conducted at room temperature (22–24 °C) only.

The experimental procedure was as follows. A pre-scan was performed prior to each experiment to assure that the residual charges existing in the sample were negligible. Further, sample surface was exposed to corona from the needle for two minutes. After completing the charging, the needle electrode was removed whereas the probe was placed above the center of the sample for continuously monitoring potential at this position. Potential distribution on the winding was measured at predefined times by scanning its surface in the directions along and across the wires. The duration of the scan was ~20 s. After completing each SPD measurement, the winding surface was grounded during a long period of time for neutralizing the remaining charges, thus preparing it for the next measurement. Additionally, SPD measurements were carried out on the flat samples of PAI with and without Cr_2O_3 micro-fillers described in section 3.1.2. Each experiment was implemented 2–3 times and good reproducibility of the results was achieved.

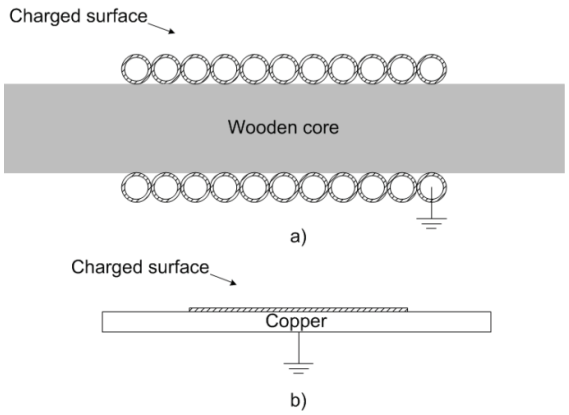

Figure 3.10. Winding of enameled wires used in the experiments (a) and its equivalent representation by a flat layer of insulation on top of a grounded copper plate (b). The winding cross section is enlarged for clarity.

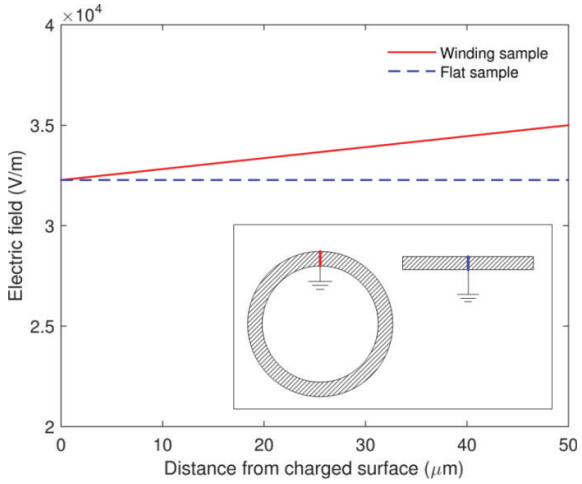

Figure 3.11. Electric field in the insulation of the winding and flat samples having a surface charge density of 10^{-6} C/m^2. The inset shows the cross sections of two samples as well as the directions along which the electric field was calculated.

3.2.4. Thermally stimulated discharge current measurements

Experiments were conducted using 80 μm thick films of LDPE doped with 3 wt% of Al_2O_3 nanofillers and samples of unfilled LDPE. An evaporated aluminum electrode was created on one side of the samples. The specimen was kept in a holder consisting of a metallic plate and a metallic ring (fixed together by screws), as illustrated in Figure 3.12a. The metalized side of the sample was in contact with the grounded plate while the other side was left open. The poling of the sample was performed by corona charging in air at room temperature, which was carried out for five minutes. A triode electrode system was used in which the voltage applied to the needle was 10 kV, whereas the grid voltage was varied in a range 1–3 kV. After poling, the sample holder was placed in a test cell for measuring open-circuit TSD currents by means of a Keithley electrometer (model 6517B), as shown in Figure 3.12b. The diameter of the measuring electrode was 20 mm. The separation between the charged surface and the measuring electrode (air gap g) was 3 mm.

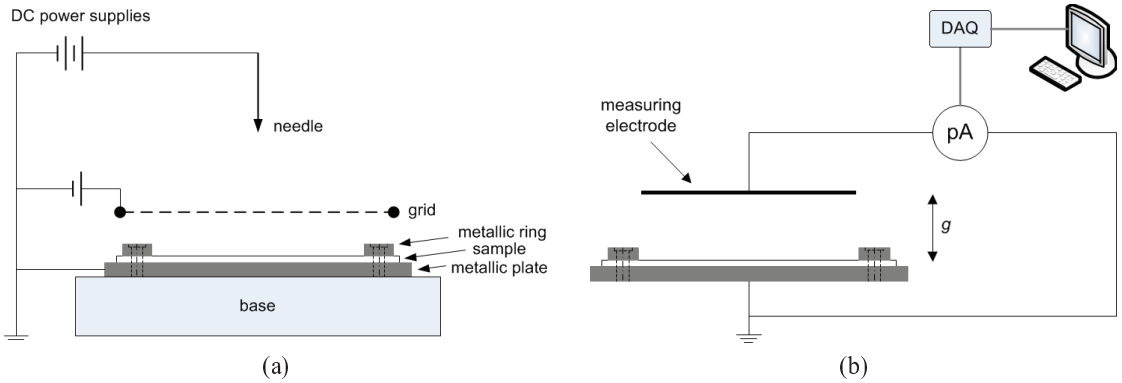

Figure 3.12. Schematic illustration of (a) poling system and (b) experimental setup for open-circuit TSD current measurements.

Appropriate thermal programs were employed for attaining the full TSD spectra as well as TSD currents under partial heating cycles. In the former case, the sample was after poling cooled down to –20 °C and then heated up to 100 °C. For the partial heating cycles, the process was implemented in a stepwise manner, so that the final temperature of a consecutive step was always 10 °C higher than that of the previous one. A rapid cooling to temperature of –20 °C was implemented between two partial heating steps. The final temperatures of the steps were 40 °C, 50 °C, *etc.*, and 100 °C. The highest temperature (100 °C) that is lower than the melting point of LDPE (110–115 °C) was selected in both thermal programs for avoiding modifications of samples during the tests. The heating rate of 3 K/min was set in the tests.

3.3. Computer simulations

3.3.1. Model of charge transport in insulating materials

In this section, we provide the description of a model of charge generation and transport in a flat insulating material of thickness L that is sandwiched between two electrodes for applying a DC electric field. A positive voltage V_0 is applied to the anode at zero time, while the cathode is grounded. In general, the radii of the electrodes are much larger than the thickness of the material sample, thus the edge effect can be neglected. Therefore, the study of charge transport in the flat sample can be reduced to a one-dimensional (1D) domain. In such a case, most of the parameters described below are functions of coordinate x along insulation thickness and time t (note that these dependencies are usually omitted in mathematical expressions).

To describe conduction process under given conditions, the bipolar charge transport model [44, 46] is employed. In the model, charge carriers are generated in the material due to the injection of holes at the anode and of electrons at the cathode. The injected charge carriers drift through the bulk due to the electric field and their movement is affected by two types of localized states, namely shallow and deep traps. Charge carriers transported between shallow traps are referred to as mobile electrons and holes, whereas the ones being captured in the deep trapping centers are referred to as trapped electrons and holes. In the model parameters, mobile electrons and holes, trapped electrons and holes are respectively denoted by subscripts e and h, etr and htr. Charge species captured in deep traps can be released back to the transport state through a de-trapping process. Furthermore, the drift of charge carriers through the material is also associated with their irreversible losses due to various types of recombination.

As mentioned, charge carriers can be injected into the insulation through both electrodes as a high DC electrical field is applied. By assuming Schottky's mechanism, the densities of injected currents can be expressed as:

$$j_e(0,t) = AT^2 \exp\left(-\frac{q(\varphi_K - \Delta\varphi_K)}{kT}\right), \tag{3.1}$$

$$j_h(L,t) = AT^2 \exp\left(-\frac{q(\varphi_A - \Delta\varphi_A)}{kT}\right). \tag{3.2}$$

Here, the coordinates of the cathode and anode are respectively 0 and L, m; parameters A, T, k, q, φ have the same meaning as in eqn. (2.4); subscripts A and K denote the anode and cathode, respectively; $\Delta\varphi_{A,K}$ are the field-lowered barrier heights for charge injection due to the electric field $E_{A,K}$ at corresponding electrodes:

$$\Delta\varphi_{A,K} = \sqrt{\frac{qE_{A,K}}{4\pi\varepsilon_0\varepsilon_r}}, \tag{3.3}$$

where $\varepsilon_0 = 8.854\times10^{-12}$ Fm^{-1} is the permittivity of vacuum and ε_r being material relative permittivity.

Transport of injected charge carriers through insulating materials is governed by a system constituting transport equation (3.4), current continuity equation (3.5), differential equation (3.6) describing dynamics of trapped charges, and Poisson's equation (3.7):

$$j_{e,h}(x,t) = q\mu_{e,h}n_{e,h}(x,t)E(x,t), \tag{3.4}$$

$$\frac{\partial n_{e,h}(x,t)}{\partial t} + \frac{1}{q}\frac{\partial}{\partial x}\left(j_{e,h}(x,t)\right) = S_{e,h}(x,t), \tag{3.5}$$

$$\frac{\mathrm{d}n_{etr,htr}(x,t)}{\mathrm{d}t} = S_{etr,htr}(x,t), \tag{3.6}$$

$$\nabla\left(\varepsilon_0\varepsilon_r E(x,t)\right) = \rho\left(x,t\right). \tag{3.7}$$

Note that in the transport equation (3.4) only the drift current is accounted for, whereas the diffusion current is neglected following commonly used approach [44-46, 84] discussed in the chapter above. We also revealed the insignificant contribution of the diffusion current through additional simulations performed using models with and without considering this component. For the sake of clarity, the results obtained in these calculations will not be presented. The conduction current through the material bulk is associated with hopping between shallow traps with the apparent effective mobilities $\mu_{e,h}$, as already defined in eqn. (2.12). The source terms on the right hand sides of eqns. (3.5) and (3.6) are introduced below. The term $\rho(x,t)$ on the right hand side of eqn. (3.7) denotes the total space charge density:

$$\rho = q\left(n_h + n_{htr} - n_e - n_{etr}\right). \tag{3.8}$$

The intensity of trapping process is characterized by trapping coefficients $t_{e,h}$ which reflect the probability of capturing of charged species per unit of time. The total trapping rates are quantified as:

$$T_{e,h} = t_{e,h}n_{e,h}\left(1 - \frac{n_{etr,htr}}{N_{etr,htr}}\right), \tag{3.9}$$

where $n_{e,h}$ and $n_{etr,htr}$ are the densities of the charge carriers, $N_{etr,htr}$ are the total densities of deep traps in the insulating material.

The rates of de-trapping from deep traps, which are considered as potential wells with barrier heights $\varphi_{etr,htr}$, are introduced as:

$$DT_{e,h} = \nu_0 n_{etr,htr} \exp\left(-\frac{\varphi_{etr,htr}}{kT}\right)\frac{n_{etr,htr}}{N_{etr,htr}}, \tag{3.10}$$

where $\nu_0 = kT/h$ [45] being the attempt-to-escape frequency, and h indicating Planck constant. The dynamics of filling/releasing traps are described by eqn. (3.6).

In the model, it is assumed that recombination of charges of opposite polarities is mainly between trapped and mobile charges and takes place at trapping sites acting as recombination centers. Probability of recombination between two types of mobile charges is significantly lower [44, 89] and can be neglected. In general, the recombination processes lead to the losses in quantity of charged species that are expressed using the rates:

$$\begin{aligned} R_{eh} &= r_{eh} n_e n_h, \\ R_{etrh} &= r_{etrh} n_{etr} n_h, \\ R_{ehtr} &= r_{ehtr} n_e n_{htr}, \\ R_{etrhtr} &= r_{etrhtr} n_{etr} n_{htr}. \end{aligned} \tag{3.11}$$

Here, r indicates recombination coefficient and the subscripts *eh*, *etrh*, *ehtr*, *etrhtr* represent recombination between mobile electrons and mobile holes, trapped electrons and mobile holes, mobile electrons and trapped holes, trapped electrons and trapped holes, respectively.

Thus, the total rates of generation and losses of mobile and trapped charges in eqns. (3.5) and (3.6) above can be expressed as:

$$\begin{aligned} S_e &= -R_{eh} - R_{ehtr} - T_e + DT_e, \\ S_h &= -R_{eh} - R_{etrh} - T_h + DT_h, \\ S_{etr} &= -R_{etrh} - R_{etrhtr} + T_e - DT_e, \\ S_{htr} &= -R_{ehtr} - R_{etrhtr} + T_h - DT_h. \end{aligned} \tag{3.12}$$

Note the signs of the terms in eqns. (3.12) which indicate generation (positive rate) or loss (negative rate) mechanisms. Thus, the mobile charges are lost through trapping and recombination and are gained through de-trapping while the latter is the sink of trapped charges.

Finally, the measurable time-dependent conduction current density through the sample summarizing the contributions from both types of charge carriers is found as:

$$J_{cond}(t) = \frac{1}{L}\int_0^L \left[j_h(x,t) + j_e(x,t)\right] \mathrm{d}x. \tag{3.13}$$

It is well-known that the measured charging current constitutes two components, namely the displacement and conduction currents. Since the first component arising due to the application of a DC voltage on material sample is a non-zero value only within a transient process, its contribution to the charging current measured in a long-time range is negligible. Hence, the simulated current density $J_{cond}(t)$ is used below for comparison with experimentally obtained current density.

The initial and boundary conditions are as follows. Since the application of a high electric field to the insulation is considered, the density of charge carriers in the material corresponding to thermal equilibrium prior to the voltage application is assumed to be insignificant as compared to the density of injected carriers. Therefore, the densities $n_{e,h}$ and $n_{etr,htr}$ are set to zero at $t = 0$. Additionally, if charge carriers of certain polarity reach the counter electrode, no extraction barrier for their ejection is specified in the model. In other words, all electrons arriving to the anode and holes arriving to the cathode disappear from the insulation domain. For this, the outward current densities at corresponding electrodes (*i.e.* j_e at the anode and j_h at the cathode) are determined in accordance to eqn. (3.4).

3.3.2. Implementation of the model

The model was implemented in finite element software COMSOL Multiphysics. Numerical solutions of the equation system (3.5)–(3.7) were obtained in a 1D computational domain. Suitable application modes provided in the software were selected for solving the continuity equation (3.5), ordinary differential equation (3.6), and Poisson's equation (3.7). The coupling of different application modes was implemented so that the densities of charge carriers obtained as solutions of eqns. (3.5) and (3.6) at every time step were updated in eqn. (3.8) for gaining the total space charge density. This was further utilized in Poisson's equation (3.7) for deriving the electric field distribution. The external conduction current density through the sample was calculated by substituting the transport equation (3.4) into (3.13). A non-uniform mesh was created with extremely small elements in the vicinity of both electrodes (the smallest element size 0.1 μm), whereas a coarser mesh was kept in the middle of the sample. A small artificial diffusion was introduced for providing numerical stability and better convergence while solving eqn. (3.5).

4. Charge transport in low-density polyethylene and its nanocomposites

This chapter presents experimental study and computer simulations of charge transport in LDPE and its nanocomposites in a comparative manner focusing on the contribution of nanofillers to material properties. Three experimental techniques, namely, measurements of DC conductivity, surface potential decay, and thermally stimulated discharge currents were employed and the obtained results are reported in this order. Both single- and multi-layered insulations were utilized in the experiments that allows for examining the role of the internal interface between two insulating layers in charge transport. Finally, a numerical model was applied for reproducing experimental results as well as for analyzing the influence of different factors on charge transport processes in both types of the studied insulations.

4.1. Results of DC conductivity measurements

4.1.1. Currents in single-layered samples

This section focuses on studying material DC conductivity under electric fields exceeding 10^7 V/m. The influences of antioxidant and nanofillers as well as their content on the material property were examined. Effects of temperature and electric field on electrical conduction of the materials were considered by modifying the experimental conditions accordingly.

4.1.1.1. Effect of antioxidant

As mentioned above, a small amount (0.02 wt%) of the antioxidant was added to LDPE during manufacturing for avoiding the oxidation of the material. The measurements were conducted on LDPE with and without the antioxidant to study its impact on material DC conductivity. The tests were performed on ~155 μm thick samples at 40 °C and 60 °C by applying a DC voltage of 5.0 kV. Experimental results illustrated in Figure 4.1 show that the shapes of the current curves were preserved and the current magnitudes changed slightly. Thus, the presence of such a small amount of the antioxidant in LDPE did not cause noticeable variation in the material DC conductivity. LDPE doped with the antioxidant is therefore utilized as a reference material throughout this study.

4.1.1.2. Effect of filler content

Experiments were conducted on 80 μm thick films at 60 °C by applying a DC voltage of 2.6 kV. Figure 4.2 illustrates the time variations of the measured current densities, which can be represented by power functions with various values of factor *n*

$$j(t) \propto t^{-n}. \tag{4.1}$$

As seen, the currents through the reference LDPE and LDPE/MgO 0.1 wt% materials decreased gradually and their time dependences in the log–log scale are close to straight lines with a single slope $n \approx 0.4$. It is notable that these currents did not reach a steady state during the measuring time (~11h). It has been suggested in [24] that such slowly decaying currents can be attributed to the effect of space charge build-up in the bulk rather than to slow dipole orientation. This hypothesis has been supported by the fact that the discharging current is remarkably lower than the charging counterpart, which indicates insignificant dipole depolarization [24]. Note that even though PE is well-known as a non-polar polymer, dipolar substances such as impurities or by-products of oxidation may still exist in the material, resulting in the apparent polarization. In light of the proposed premise [24], since the charging currents obtained in the present study for $t \geq 10^3$ s were at least two orders of magnitude higher than the discharging ones (see Figures 4.6–4.7, section 4.1.1.4), the space charge

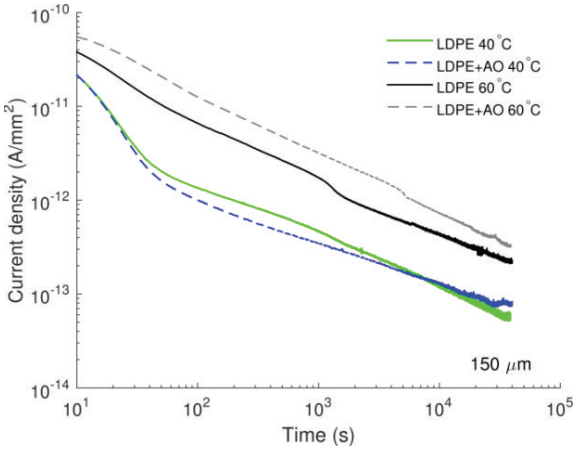

Figure 4.1. Densities of charging currents measured on LDPE with and without antioxidant.

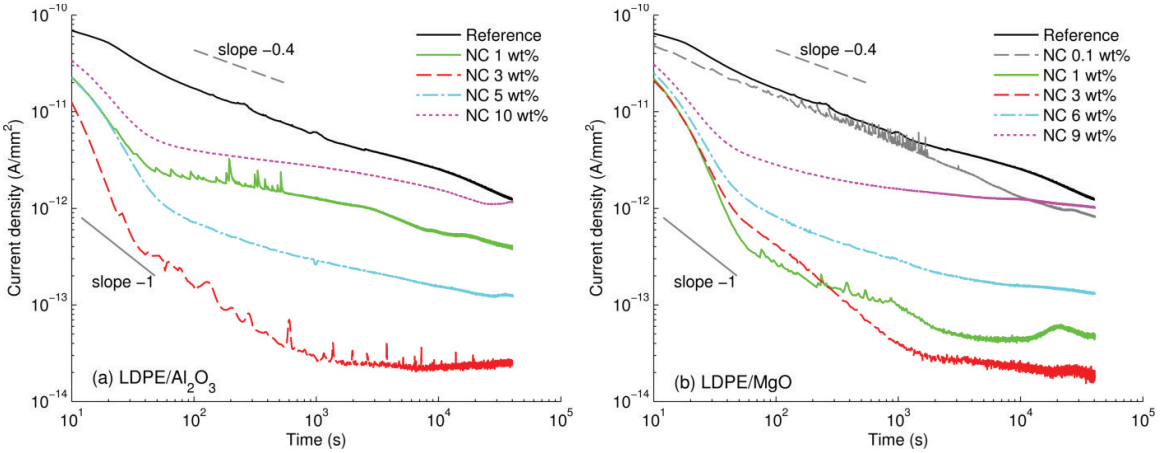

Figure 4.2. Densities of charging currents as functions of time measured at 60 °C for reference LDPE and both nanocomposites: (a) LDPE/Al_2O_3 and (b) LDPE/MgO.

accumulation in the insulation bulk should be dominant over the polarization in the considered materials.

The shape of the recorded current traces changes significantly in cases of nanocomposites with filler content of 1 wt% or higher. A knee point at ~50–70 s after the voltage application can be seen in the characteristics of these materials. Within the initial 50–70 s, the currents decayed rapidly with the slope *n* exceeding 1 that is more likely due to the slow polarization as suggested in [24]. Thereafter, as the polarization process ceases, the conduction currents became prevailing and the power factor *n* in eqn. (4.1) is getting closer to zero that corresponds to a steady state, *i.e.* DC conduction mode. In the following, the quasi-steady state conduction currents observed at $\sim 4\times10^4$ s are used for comparisons. Overall, the measured currents are commonly lower for the nanocomposites as compared to the reference material, indicating a weakening of the charge transport. Thus, for LDPE/Al_2O_3 nanocomposite at the nanofiller content of 3 wt% the current was reduced by almost two orders of magnitude. A less pronounced reduction was found in case of 1 wt% and 5 wt% of nanofiller load, while the filler content of 10 wt% resulted in the same current magnitude as for the unfilled LDPE. Similarly, a significant drop was also exhibited at the filler loading of 3 wt% for LDPE/MgO nanocomposite, whereas lower (0.1 wt%) or higher (9 wt%) amounts of this nanofiller did not result in noticeable changes of the property.

The materials' DC conductivities calculated by utilizing the charging currents at 4×10^4 s are shown in Figure 4.3. For LDPE, the outcome is in good agreement with data reported in literature, *e.g.* [65]. For both nanocomposites, similar dependences of DC conductivities on filler content can be noticed, which is featured by a threshold-like behavior at ~3 wt%. As seen from the plot, after reaching this point, further addition of nanoparticles causes a negative effect, *i.e.* the DC conductivity increases remarkably with higher filler loading that can be explained by a formation of agglomerations of nanoparticles in the base material [103]. Note that the agglomerated structures of nanoparticles were actually observed in the studied composites at high wt-percentages, as shown in Figure 3.3. The obtained results for the LDPE/MgO nanocomposite are in line with earlier reported investigations [66, 103], where a decrease in the DC conductivity in more than one order of magnitude and a threshold of filler loading at ~2 wt% were observed.

4.1.1.3. Effect of temperature

Further investigations focused on analyzing the temperature dependence of the DC conductivity. The study was carried out on the nanocomposites showing the greatest reduction in the DC conductivity, *i.e.* the materials with filler loading of 3 wt%. Experimental results obtained for both nanocomposites are presented in Figure 4.4 in comparison with those for unfilled LDPE. It is noteworthy to mention that the time-dependent current density measured at room temperature on the reference LDPE was in a good agreement with the corresponding result reported in [46]. As it is seen in Figure 4.4, the reduction in the current density associated with the introduction of nanofillers is the most remarkable at 60 °C, whereas it is lower at room temperature.

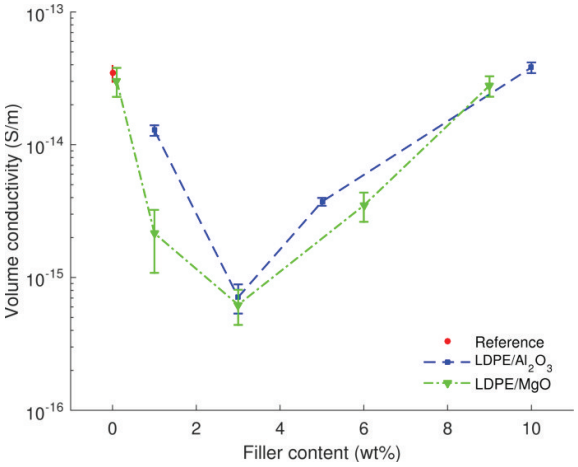

Figure 4.3. Dependence of DC conductivity (at 60 °C) of the studied nanocomposites on filler content.

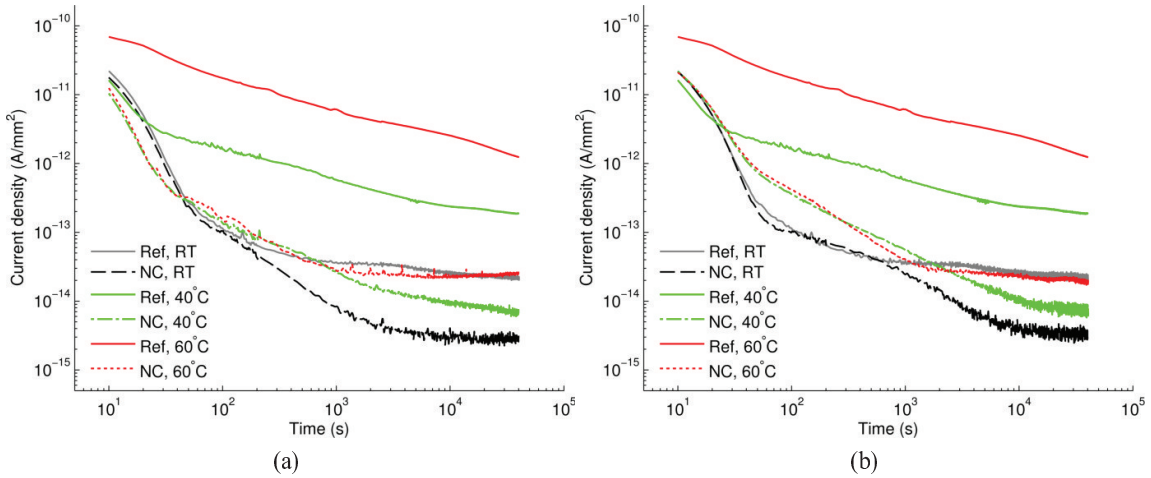

Figure 4.4. Densities of charging currents as functions of time measured at room temperature (RT) ~20–22 °C, 40 °C, and 60 °C for the reference LDPE (*Ref*) and LDPE nanocomposites 3wt% (*NC*): (a) LDPE/Al_2O_3 and (b) LDPE/MgO.

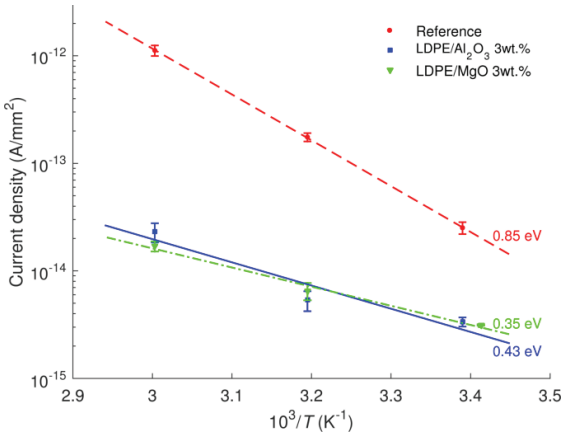

Figure 4.5. Temperature dependences of the current densities of LDPE and its nanocomposites at 4×10^4 s. The calculated activation energies are indicated.

The current densities obtained at 4×10^4 s as functions of the reciprocal of the absolute temperature are shown in Figure 4.5. The activation energies W_a for the studied materials can be derived by assuming Arrhenius type of the temperature dependence:

$$J_C(T) = J_0 \exp\left(-\frac{W_a}{kT}\right), \tag{4.2}$$

where $J_C(T)$ denotes measured current densities at various temperatures, J_0 is a constant. The calculated values are indicated in the figure. The activation energy is higher for the reference LDPE as compared to the nanocomposites. The outcome therefore suggests that at temperatures higher than 60 °C, the reduction in the DC conductivity due to the introduced nanoparticles would be even more pronounced and the associated charge transport is strongly suppressed.

4.1.1.4. Effect of electric field

The influence of an electric field on the electrical conduction in the studied materials was examined by varying the field strength in the range of 20–60 kV/mm. The measurements were conducted on 80 μm thick samples of LDPE and LDPE/Al_2O_3 3wt% nanocomposite at temperatures of 40 °C, 60 °C, and 80 °C. A polarization–depolarization protocol used in the experiments comprised polarization within ~3h which was followed by depolarization process of at least 6h, while the corresponding responses *i.e.* the polarization/depolarization or charging/discharging currents were recorded. A consecutive polarization–depolarization cycle was performed with an increment of the electric field of 2.5 kV/mm.

Examples of charging currents obtained in the described procedure are shown in Figure 4.6. Note that for the nanocomposite, the tests conducted at electric fields lower than 25 kV/mm showed low signal-to-noise ratios so they are not reported here. As seen, the shape of the current curves for LDPE was preserved with a knee point observed at ~50 s while the current magnitude increased gradually with the applied electric field. For LDPE/Al_2O_3 nanocomposite, the charging currents measured at 80 °C for electric fields below 30 kV/mm exhibited the change in their polarity. This observation suggests that the currents comprised two components: one decayed quickly due to the polarization process and the other rose slowly due to the conduction process. For higher electric fields, the steady-state of the charging currents in the nanocomposite was well established at 10^4 s.

The measured discharging currents on two materials are illustrated in Figure 4.7. Discharging currents usually flow in the opposite direction as compared to the charging alternatives. For presenting the negative discharging currents in the logarithmic scale, their absolute values were taken. For the sake of clarity, fewer current curves are presented in Figure 4.7 as compared to Figure 4.6. As seen, the discharging currents were at least two orders of magnitude lower than the charging counterparts. For LDPE at 60 °C, the shapes of the curves were similar while the magnitude of discharging currents increased monotonically and slightly with the applied field. Two knee points corresponding to the change of the slopes of the curves can be observed at ~50 s and ~10^3 s. At the applied electric fields below 50 kV/mm, the polarity reversal of the discharging currents happened twice; in particular,

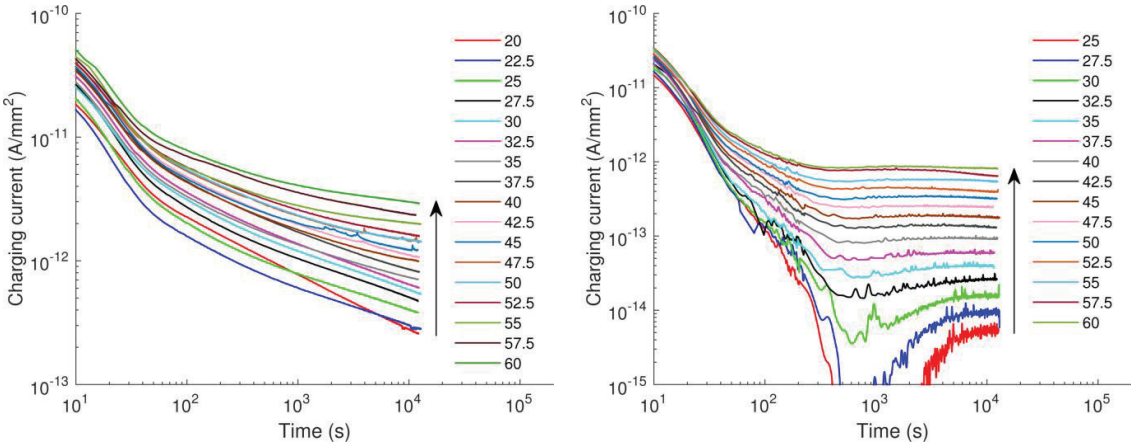

(a) LDPE, 60 °C (b) LDPE/Al_2O_3 nanocomposite, 80 °C

Figure 4.6. Densities of charging currents measured at electric fields indicated in the legend (in kV/mm). Arrows show the variation of quasi-steady state currents with increasing field strength.

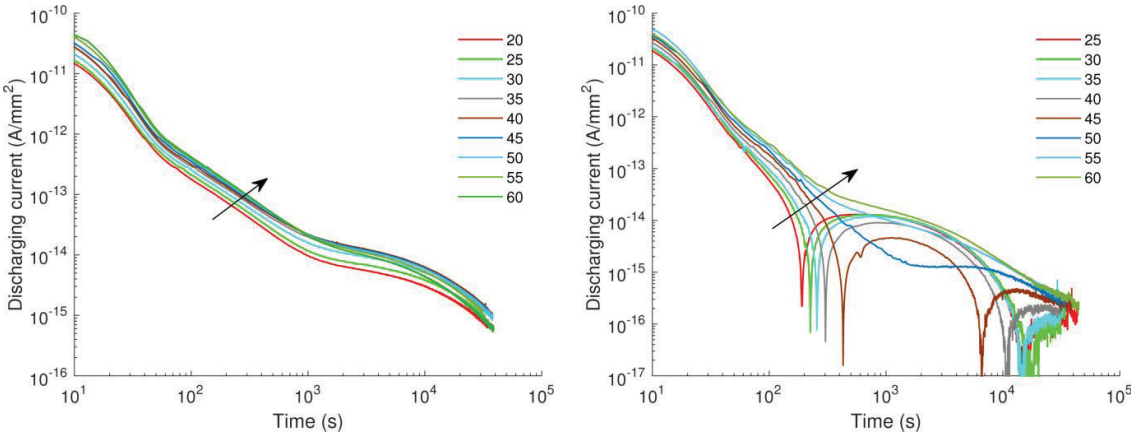

(a) LDPE, 60 °C (b) LDPE/Al_2O_3 nanocomposite, 80 °C

Figure 4.7. Densities of discharging currents measured after polarization at the indicated electric fields (in kV/mm). Arrows show the variation of the currents with increasing field strength.

Table 4.1. Electric field strength (in kV/mm) for observing ADC in LDPE and its nanocomposite in the present study.

Temperature, °C	40	60	80
LDPE	–	–	20–60
LDPE/Al_2O_3 nanocomposite	–	25–35	25–47.5

the currents changed to positive values at 200–400 s and then became negative again at 10^4–2×10^4 s. The polarity reversal of discharging currents has been observed for several polymers such as PE and EVA and was referred to as the anomalous discharging current (ADC) [104]. In the present investigation, ADC was detected under certain conditions, which are provided in Table 4.1. The observation in the present study is consistent with the reported results [104] claiming that ADC arises in PE at elevated temperatures (50–70 °C) rather than at room temperature. However, the phenomenon was detected at the applied electric field lower than

10^8 V/m, which is contradictory to the assumption that the indicated field strength is the threshold for ADC (the phenomenon only occurs at higher fields) [104]. By analyzing results obtained from a simplified numerical model of charge transport, Kitani *et al.* [105] pointed out that the phenomenon should be attributed to bipolar charge injection into insulation. The latter yields the build-up of both positive and negative space charges in the bulk during the polarization phase. Under short-circuit conditions, as the integral of the electric field over the sample thickness is zero, regions of positive and negative fields can be distinguished in the bulk. Transport of space charges in positive and negative field regions towards electrodes gives rise to currents of the respective signs, the sum of them is nothing else but the discharging current measured in an external circuit. The positive discharging current resulted when the positive current dominated over the negative one. The authors [105] also indicated that ADC may not be attributed to the blocking electrode, as it was previously explained in [106].

Field dependence of the conduction currents

Figure 4.8a presents a log–log plot of the current densities recorded at 3h after charging *versus* electric field in reference LDPE. At temperatures 40 °C and 60 °C, the slope m (provided in Table 4.2) of the dependency $J \propto E^m$ is close to 2, indicating that SCLC is the most likely dominant conduction mechanism in the material. At 80 °C, the dependence exhibits a knee point at the electric field strength of 35 kV/mm at which the slope changes. The reason behind this is unclear, but a possible explanation could be a change in the conduction mechanism. For the field strength below 35 kV/mm, the factor m is close to 1 indicating that ohmic conduction may be dominant. At stronger fields, as the factor m is larger than 2, the conduction probably follows the SCLC mechanism according to eqn. (2.19). Further, Schottky and Poole–Frenkel plots for reference LDPE are illustrated in Figures 4.9a and 4.10a, respectively. As seen, the values of the relative permittivity used to get best fit (Table 4.2) are generally different from the value 2.3 commonly reported for PE (except for the field above 35 kV/mm and temperature 80 °C). The results suggest that neither Schottky injection nor Poole–Frenkel mechanisms explain satisfactorily the behavior of the conduction current at all considered temperatures. A similar analysis was conducted in [63] and it was found that Schottky injection dominated in LDPE at room temperature, but not at elevated ones.

The field dependencies of the current densities in LDPE/Al_2O_3 nanocomposite are illustrated in Figures 4.8b–4.10b and the derived parameters m and ε_r are provided in Table 4.2 for comparison. As seen, the power factor m in the dependency $J \propto E^m$ is significantly higher for LDPE/Al_2O_3 nanocomposite as compared to that of reference LDPE. The results also indicate that SCLC mechanism followed eqn. (2.19) appears to be the dominating conduction mechanism in the nanocomposite, while both Schottky injection and Poole–Frenkel mechanisms cannot adequately explain the experimental data of the nanofilled materials under consideration.

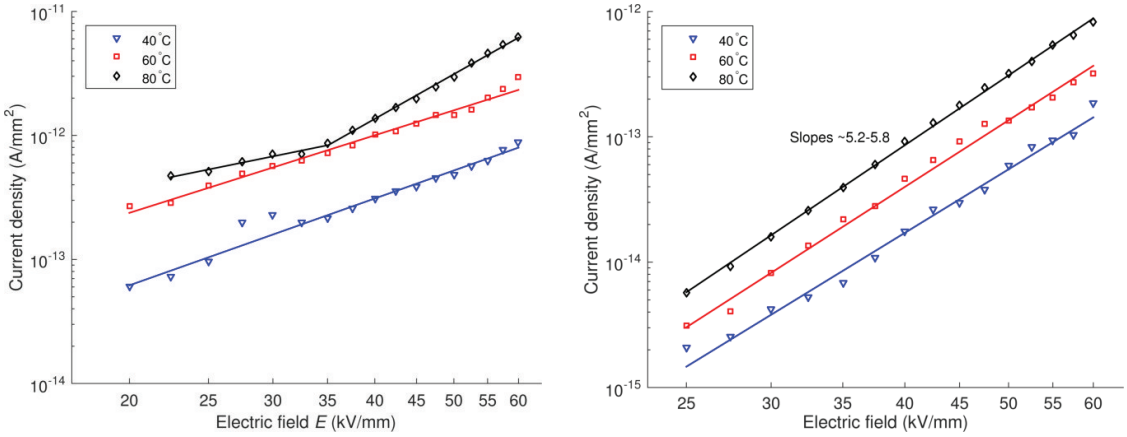

(a) LDPE (b) LDPE/Al_2O_3 3wt% nanocomposite

Figure 4.8. Log–log plots of *J vs. E* for (a) reference LDPE and (b) LDPE/Al_2O_3 3wt% nanocomposite at various temperatures.

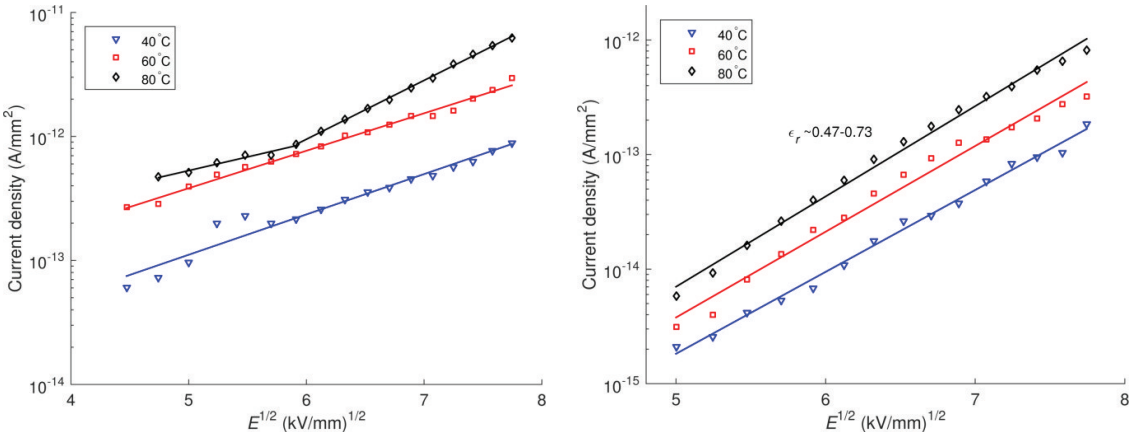

(a) LDPE (b) LDPE/Al_2O_3 3wt% nanocomposite

Figure 4.9. Schottky plots for (a) reference LDPE and (b) LDPE/Al_2O_3 3wt% nanocomposite at various temperatures.

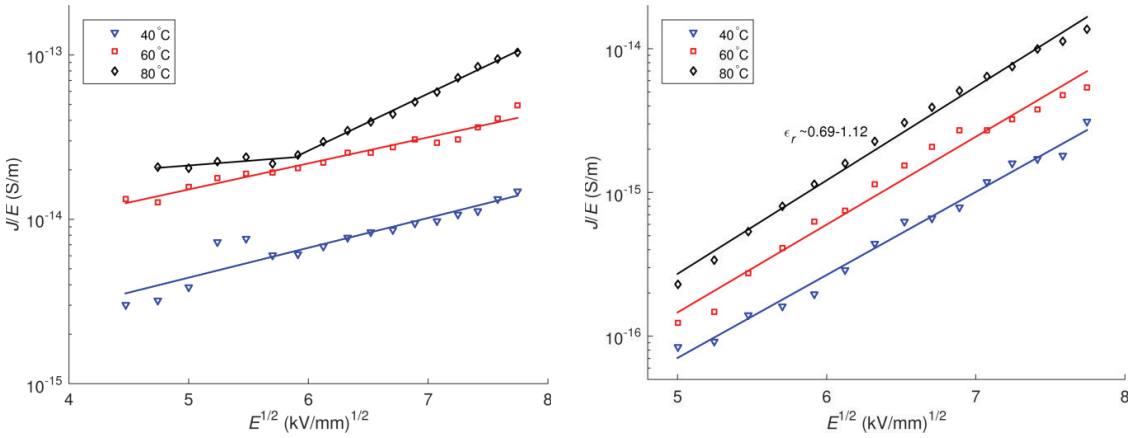

(a) LDPE (b) LDPE/Al_2O_3 3wt% nanocomposite

Figure 4.10. Poole–Frenkel plots for (a) reference LDPE and (b) LDPE/Al_2O_3 3wt% nanocomposite at various temperatures.

Table 4.2. Calculated parameters in characteristics of J *vs.* E. Note that the obtained values of ε_r below 1 do not have physical significance.

Characteristics	Calculated parameters	LDPE				$LDPE/Al_2O_3$ NC		
		40 °C	60 °C	80 °C		40 °C	60 °C	80 °C
$J \propto E^m$	m	2.33	2.08	1.34	3.72	5.23	5.49	5.75
Schottky	ε_r	3.52	3.60	6.05	1.30	0.73	0.59	0.47
Poole–Frenkel	ε_r	11.3	13.1	91.7	2.43	1.12	0.88	0.69

The temperature dependencies of the currents on $LDPE/Al_2O_3$ 3wt% nanocomposite recorded at 3h for different applied fields are presented in Figure 4.11. The activation energies calculated using Arrhenius dependence, eqn. (4.2), are illustrated in Figure 4.12. As seen, the obtained values vary in a narrow interval (0.35–0.45 eV) that is close to the activation energy (0.43 eV) calculated in section 4.1.1.3 using the current recorded at 4×10^4 s.

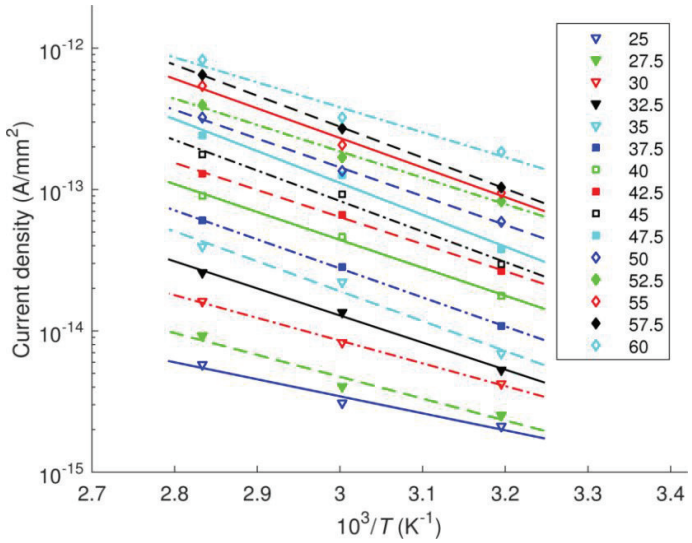

Figure 4.11. Temperature dependencies of current densities recorded at 3h (1.08×10^4 s) for $LDPE/Al_2O_3$ 3wt% nanocomposite at different applied electric fields indicated in the legend (in kV/mm).

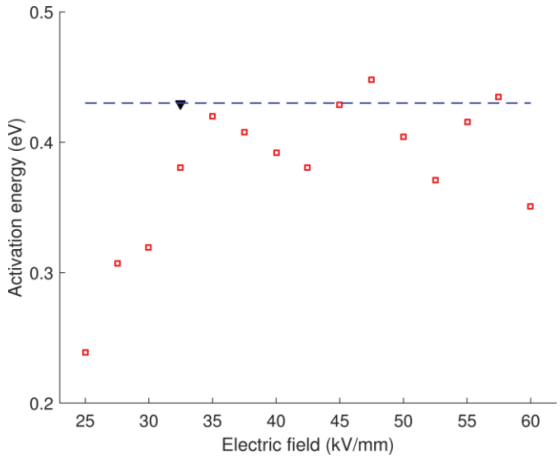

Figure 4.12. Activation energies of $LDPE/Al_2O_3$ 3wt% nanocomposite calculated using charging currents measured at 1.08×10^4 s (open square) and at 4×10^4 s (solid triangle).

4.1.2. Currents in multi-layered samples

Experiments were also conducted on multi-layered samples for checking the influence of the internal interface on the charge transport process. Investigations were carried out on four double-layered structures that are *Ref*/*Ref*, *NC*/*NC*, *Ref*(*A*)/*NC*, and *NC*(*A*)/*Ref*, where *Ref* and *NC* respectively denote the pure LDPE and LDPE/Al_2O_3 3wt% nanocomposite, (*A*) indicates the layer in contact with the anode. As the films were ~80 μm thick, double-layered samples of ~160 μm were formed. A DC voltage of 5.2 kV was applied that resulted in the magnitude of the electric field (32.5 kV/mm) identical to that used in the measurements on single-layered insulations. For making a good contact between two insulating layers as well as between them and the electrodes, the samples were pressed at 60 °C using the weight applied on the high voltage electrode (~1 kg) for at least 6h. The targeted temperature was thereafter set for ~12h so that the thermal equilibrium in the oven was well established.

Charging currents obtained for the multi-layered insulations at 60 °C are presented in Figure 4.13a. To highlight the contributions of the internal interface to electrical conduction, experimental results on single-layered specimens obtained at the same conditions (electric field and temperature) are also provided for comparison. Note that according to the SCLC mechanism, the conduction current is strongly affected by specimen thickness. For example, according to eqn. (2.18), the conduction current is doubled by reducing sample thickness in two times assuming that the material properties (μ, ε) and the applied electric field are unchanged. This effect was thus eliminated by using in the tests 155 μm thick single-layered samples, which are of similar thickness as for the multi-layered counterparts. A DC voltage of 5.0 kV was applied on these specimens. As seen, the measured currents usually reached a quasi-steady state at time exceeding 10^4 s and these current values are therefore used for comparison. Comparing the data obtained for *Ref 155μm* and *Ref*/*Ref*, *e.g.* curve (1) *vs.* curve (2), as well as for *NC*/*NC* and *NC 155μm*, *e.g.* curve (5) *vs.* curve (6), one can find that the currents on multi-layered insulations of the same materials were lower than the corresponding ones in the single-layered material. This observation indicates that the interface between two insulating layers strongly prevented charge transport through the materials. This result is consistent with the hypothesis that the insulation–insulation interface gives rise to deep surface traps that capture mobile carriers reaching it, which eventually results in the barrier effect hindering charge transport through the interface [12]. Further, by noting that the nanofilled layer suppresses charge generation and transport to a great extent as compared to the unfilled LDPE, it can be expected that the conduction current is lower for *Ref*(*A*)/*NC* than for *Ref*/*Ref*, see curve (3) *vs.* curve (2). Similar correlation is also true while comparing the current response for *NC*/*NC* with that for *NC*(*A*)/*Ref*, see curve (5) *vs.* curve (4). The most interesting observation is that the measured currents were clearly different for *Ref*(*A*)/*NC* and *NC*(*A*)/*Ref*, see curve (3) *vs.* curve (4). As these samples comprising identical components and only their position with respect to the electrodes was altered, it can be anticipated that the generation of charge carriers in the bulk, *e.g.* by Poole–Frenkel mechanism, would result in similar amount of charges in the both systems thus yielding the same conduction currents under the same applied electric field. The experimental evidence suggests, however, that this was not the case in our measurements. Charge generation should therefore be mainly due to the injection at the anode and cathode. As the measured currents were higher for *Ref*(*A*)/*NC*

than for *NC*(*A*)/*Ref*, the suppression of charge generation was stronger in case of the nanofilled layer in contact with the anode. This implies that the anode seemed to play a more important role in the injection of charge carriers into the insulation. The results also suggest that charge injection from the anode into LDPE layer is substantially stronger than that from the cathode. The currents measured at 40 °C are illustrated in Figure 4.13b. Similar correlations between charging currents were observed; in particular, they also reduced in following order of the studied samples: *Ref 155µm*, *Ref*/*Ref*, *Ref*(*A*)/*NC*, *NC*(*A*)/*Ref*, *NC*/*NC*. However at this temperature, the barrier effect in limiting the charge transport through the internal interface appeared to be weak in case of *Ref*/*Ref*, whereas it was still significant for *NC*/*NC* structure.

Discharging currents measured on the considered specimens are presented in Figure 4.14. It is noteworthy that ADC was observed only at 60 °C on the nanocomposite and the multi-layered samples with at least one *NC* layer. Thus, ADC is most likely associated with the transport of charge carriers injected into the *NC* film back to the electrodes during the depolarization phase. As will be shown by computer simulation in section 4.4 that the space charge layer occurs in the nanocomposite is much thinner than that in the unfilled material, the occurrence of ADC seems to depend on the penetration depth of injected charges in insulations as suggested in [105].

The effect of temperature on the measured currents in two multi-layered samples *Ref*(*A*)/*NC* and *NC*(*A*)/*Ref* is illustrated in Figure 4.15. While the charging currents in these structures were at the same level in the tests at room temperature, they were lower for *NC*(*A*)/*Ref* at elevated temperature. This indicates that the suppression of charge injection from the anode to the nanocomposite layer *NC* was more pronounced at higher temperature. This is consistent with the results obtained for single-layered insulations (section 4.1.1.3) showing that the reduction in the DC conductivity of the nanocomposites as compared to the unfilled LDPE increased significantly with temperature. The discharging currents, on the other hand, were not strongly different for the two samples and ADC was observed only at 60 °C.

4.2. Results of surface potential decay measurements

As shown in the previous section, the most significant reduction in the DC conductivity was observed for LDPE filled with 3 wt% of nanofillers (either Al_2O_3 or MgO). This section concentrates on investigating the electrical properties of the nanocomposites at the indicated filler content using SPD measurements.

4.2.1. Potential decay on single-layered samples

A distribution of surface potential measured on LDPE/Al_2O_3 nanocomposite sample is illustrated in Figure 4.16 and represents typical results obtained at all considered temperatures on the studied materials. The initial surface potential distribution is relatively homogeneous in the central part of the sample and the profile remains generally preserved during the measurements. Thus, a lateral spreading of the surface potential/charge is not noticed indicating a negligible contribution of surface conduction to the decay process. As the

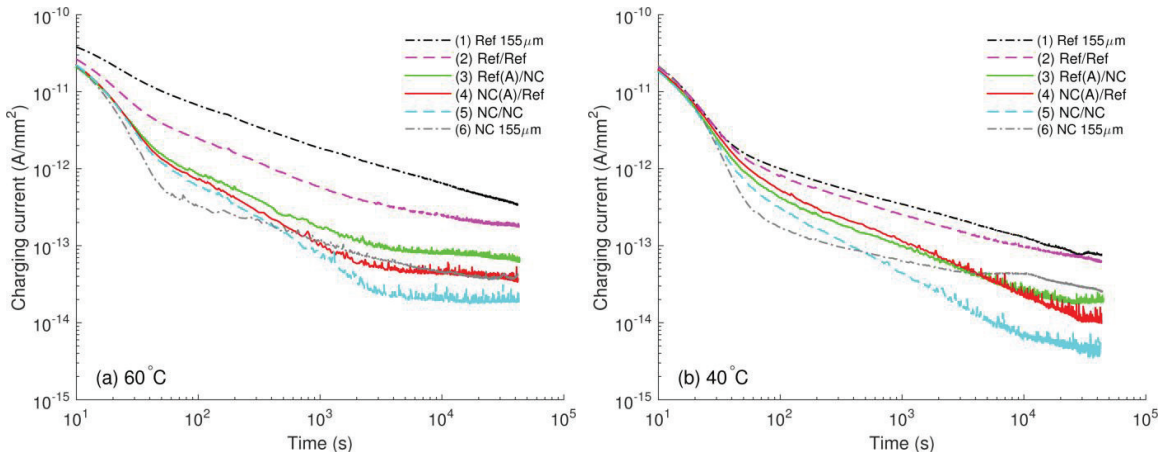

Figure 4.13. Densities of charging currents as functions of time for multi-layered samples at different temperatures and their comparison to the corresponding on single-layered insulations.

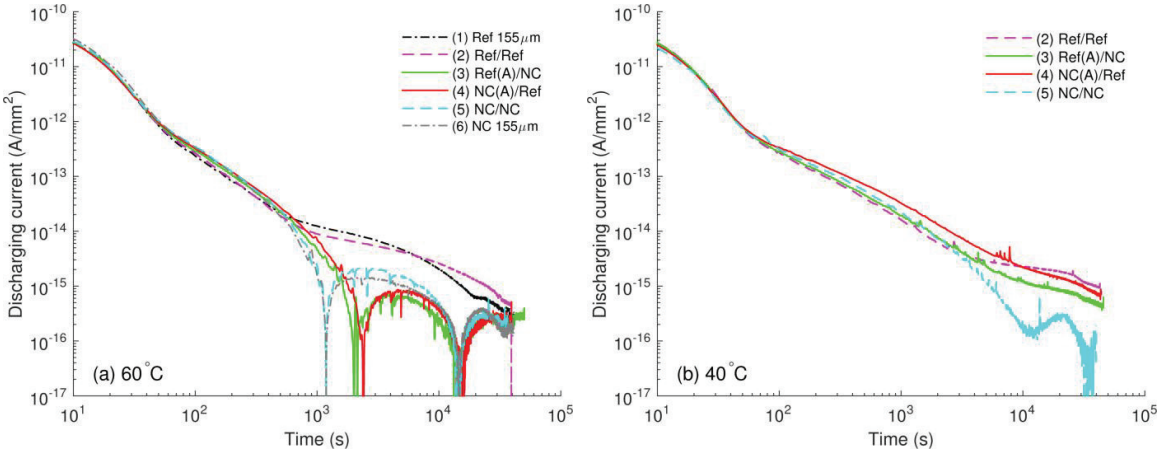

Figure 4.14. Densities of discharging currents as functions of time for multi-layered samples at different temperatures and their comparison to the corresponding on single-layered insulations.

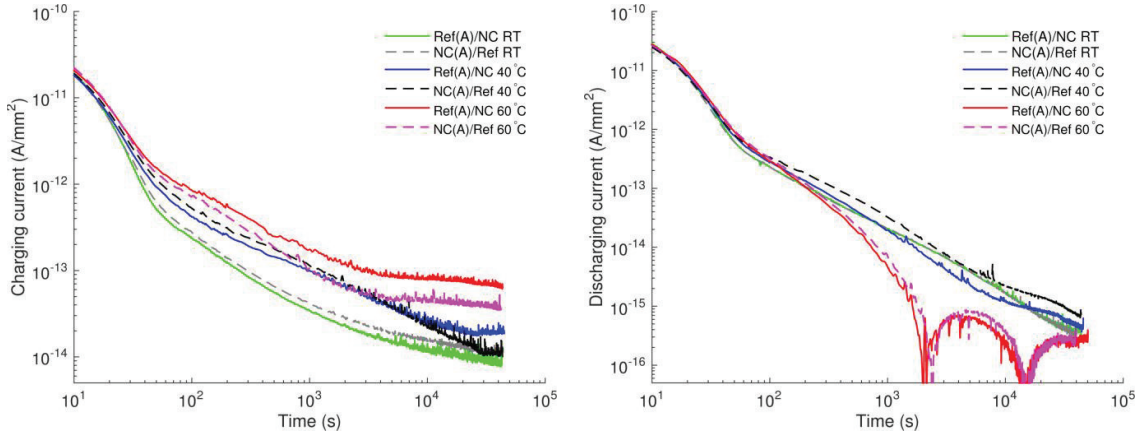

Figure 4.15. Densities of (a) charging and (b) discharging currents as functions of time for multi-layered samples at different temperatures.

Kelvin probe was always kept above the center of sample surface, zero electric field was maintained in the air gap between the surface center and the probe. Thus, neutralization by ionic species from air was to a great extent prevented [107]. As a consequence, the decay is believed to be mainly caused by processes in the insulation bulk.

The decays of surface potentials on Al_2O_3-nanofilled and reference LDPE are compared in Figure 4.17a, where zero time corresponds to the end of corona charging. The initial potentials were recorded at ~4–5 s afterwards and they are close to the value of grid potential, except for reference LDPE at 60 °C. The decay appears to be considerably slower for the nanofilled LDPE as compared to the reference LDPE, especially at higher temperatures. Since SPD is attributed to the conduction through the bulk, *i.e.* the transport of charge carriers within the material driven by the field of deposited surface charges, the experimental data imply significant limitation of charge transport due to the introduced nanoparticles.

The decay rates of the surface potentials (Figure 4.17b) can be represented as power-law functions of time. As temperature increases, a remarkable distinction in decay rates is observed at the initial stage, for the reference LDPE within the first 100 s of the decay. Note the initial decay of the potential was so high at 60 °C that the first measured potential point was ~0.2 kV lower than the grid potential. However, after 10^3 s, the decay rates became similar for the samples exposed to different temperatures. This observation should not be misinterpreted as indicating a similarity in the charge transport process. It is due to the difference in the magnitude of the electric field induced in the material at certain time, in particular, the highest field strength presented in the sample subjected to the lowest temperature, so that the apparent decay rates are comparable. As the main features in the SPD characteristics are similar for both nanofilled LDPE, measured results on LDPE/MgO nanocomposite are not presented here.

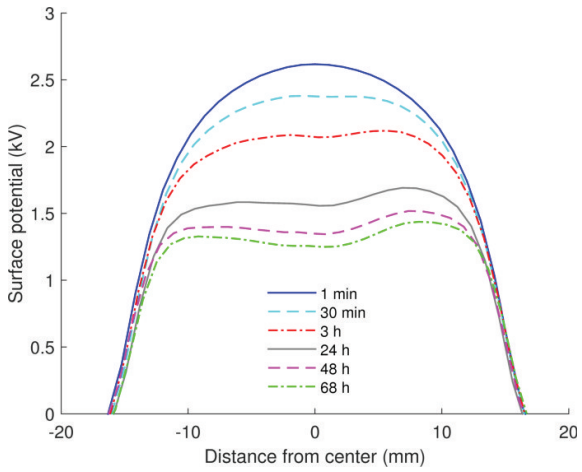

Figure 4.16. Distribution of surface potential during potential decay measurement on LDPE/Al_2O_3 3wt% nanocomposite at 60 °C.

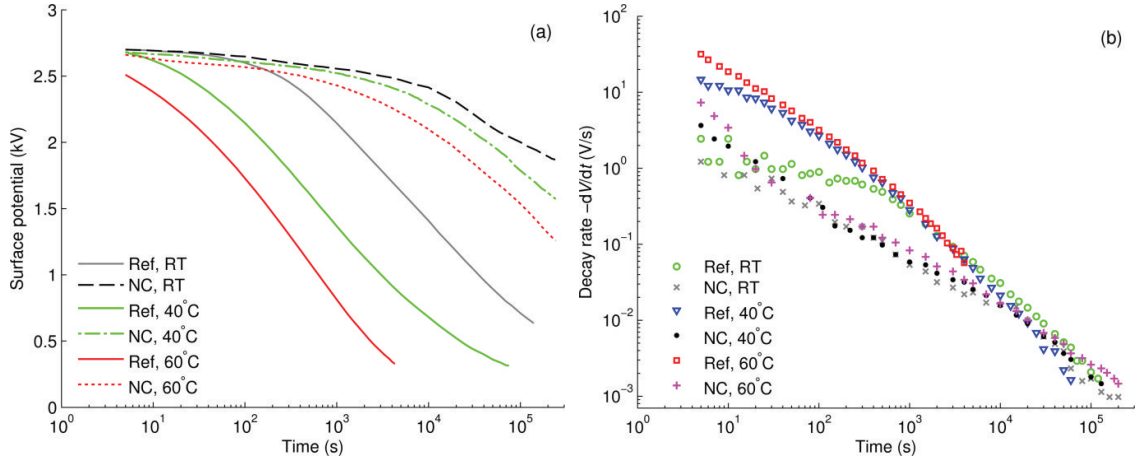

Figure 4.17. Measured surface potentials (a) and calculated decay rates (b) for reference LDPE (*Ref*) and LDPE/Al_2O_3 3wt% nanocomposite (*NC*) at different temperatures.

4.2.2. Potential decay on multi-layered samples

Measurements of surface potential decay on multi-layered samples were conducted with the aim of revealing contributions of different processes to the decay under the considered conditions. Before presenting and discussing experimental results, we would like to provide a brief summary of physical processes that may take place during SPD measurements in the bulk and at interfaces of flat samples. First of all, a high electric field induced by ionic charges created by corona and deposited on the sample surface may stimulate the charge generation in the insulation bulk according to, for example, Poole–Frenkel mechanism. Secondly, electronic charges can be injected into the bulk from the metal–insulation interface [95]. Furthermore, other processes may occur at the air–insulation interface. A commonly used assumption is that deposited charges are trapped in deep surface traps and their release yields the decay of measured surface potential [50]. This potential decay process controlled by surface traps is referred to as the surface de-trapping mechanism. On the other hand, it has been suggested in [39] that an electron transfer process between the deposited ionic charges and the surface states that results in the appearance of either holes or electrons in the latter, depending on the polarity of corona source. In other words, charges are apparently injected into insulation at the air–insulation interface. These injected charge carriers participate in the transport driven by the induced electric field that is reflected in the decaying surface potential. This hypothesis is commonly referred to as the charge injection and transport model and has been used to explain results of SPD measurements in a variety of works, *e.g.* [34, 40, 93]. Even though an electric field exceeding 10^7 V/m may be considered as sufficient enough for charge injection, a threshold value corresponding to its onset is not clearly indicated in literature. It is noteworthy to mention that in general both the surface de-trapping and charge injection mechanisms may take place during SPD. The former seems to be dominating on thin dielectric layers of a few μm [50, 51] in which extremely deep surface traps exist, whereas the latter is considered to be prevailing on relatively thicker samples, usually of a few tens of μm [34, 39, 40], provided that the induced field is strong enough.

Results of SPD measurements on multi-layered samples are presented in Figure 4.18. They exhibit a resemblance in the potentials measured within the first 200 s. Thereafter, the

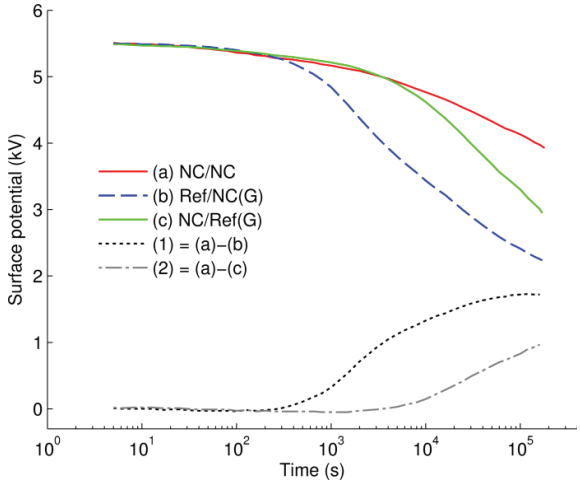

Figure 4.18. Surface potential decay on multi-layered samples. Decay curves (a)–(c) are respectively obtained on samples (a)–(c) illustrated in Figure 3.9. Curve (1) is a difference in surface potential measured on samples (a) and (b), whereas curve (2)—the difference for samples (a) and (c).

fastest decay can be observed on *Ref*/*NC*(*G*) sample, whereas the slowest one—on *NC*/*NC* sample. If charge generation in the bulk (*e.g.* by Poole–Frenkel mechanism) is assumed to be the sole contributor to the decay, the same amount of electrons and/or holes would arise in the conduction and/or valence bands due to excitation from donors and acceptors in samples *Ref*/*NC*(*G*) and *NC*/*Ref*(*G*). This would eventually lead to similar potential decay characteristics on these specimens. As the latter is contradictory to the experimental results, this assumption can be ruled out. Combination of charge generation in the bulk and charge injection at the metal–insulation interface is also unlikely the dominating processes as this would lead to a faster decay on *NC*/*Ref*(*G*) sample than on *Ref*/*NC*(*G*).

By comparing the decay curves (a) and (c), one can observe that the reference LDPE as the bottom layer in *NC*/*Ref*(*G*) sample slightly alleviates the decay as compared to the *NC* bottom counterpart in *NC*/*NC* sample. The difference in the decay is thus most likely due to an enhanced charge injection from the grounded copper plate into the LDPE layer. This can be related to the difference in the DC conductivity measured on these materials. In contrast, significant difference in potential decays was obtained on samples *NC*/*NC* and *Ref*/*NC*(*G*) (the decay curves (a) and (b) in Figure 4.18). Since charges injected from the grounded copper plate were strongly prevented in both structures by the highly resistive *NC* bottom layer, the observed difference should mainly be attributed to the intensity of charge (hole) injection into the top layers of either *NC* or *Ref*.

The possibility of charge injection at the air–insulation interface can be supported by appearance of return voltage [108] obtained in our experiments after short-circuiting the multi-layered samples at the end of the SPD tests. The short-circuiting was done by placing a metallic electrode that was connected to ground on the sample surface for 10 s. The return voltage is understood here as a potential build-up after temporarily short-circuiting the previously charged object. In the measurements, the return voltages were built up on all the three considered samples (Figure 4.19), but it was most considerable on *Ref*/*NC*(*G*) sample.

According to a simplified model proposed in [109], the appearance of the return voltage can be explained by the movement of charge carriers back to the open surface. A schematic distribution of charges on the surface and in the bulk of *Ref*/*NC*(*G*) sample is proposed in Figure 4.20. Holes that are initially injected into the top layer and transported into the bulk accumulate at the interface between reference LDPE and nanocomposite as well as in the insulation bulk (Figure 4.20a). The proposed charge distribution resembles the results of space charge measurements reported in [56]. It is thus postulated that the injection of electrons into the bottom layer is strongly impeded due to its low DC conductivity and presence of these electrons is not shown in the figure. After neutralization, ionic charges on the insulation surface cease and the electric field within the top layer is mainly created by the hole space charges. Hence, the corresponding induced field should be strongly reduced as compared to that before neutralization and its direction is altered (Figure 4.20b). The charge transport driven by this weak field requires more time to reach an equilibrium distribution inside the sample. As an illustration, the measured return voltage did not reach a steady state level even after 18h. Removal of the top LDPE layer led thereafter to an abrupt increase of the measured return voltage from ~570 V to ~660 V, as shown in the inset of Figure 4.19. This implies that the measured return voltage would increase further if the top layer was not removed. In contrast, the return voltage build-up for *NC*/*NC* sample was very small (~10 V), which can be explained by the reduced charge transport in the nanocomposite. For *NC*/*Ref*(*G*), the return voltage was ~100 V, which is most likely associated with the transport of negative space charges in the bottom layer of LDPE.

By comparing the results of SPD measurements on samples *Ref*/*NC*(*G*) and *NC*/*Ref*(*G*), see decay curves (b) and (c) in Figure 4.18, one can claim that the contribution of injected positive charges to the decay outweighed by far that of the injected negative charges. The experimental results are also consistent with the hypothesis that positive holes dominate the charge transport in LDPE [43]. In addition, it can be suggested that this feature is preserved in LDPE nanocomposites, even though the introduction of nanofillers strongly weakens the transport of both the injected holes and electrons.

An additional interesting outcome from the study is presented in Figure 4.21, where the decay rates of surface potential measured on single-layered reference LDPE sample and on multi-layered *Ref*/*NC*(*G*) are compared. As can be seen, the results for both cases are very similar and show a knee point at ~10^3 s, where the slope of the decay rate characteristic changes. The knee point can be attributed to the arrival of the charge carriers injected at the air–insulation interface [108] to the counter electrode or to the materials' interface. Consequently, the corresponding time ~10^3 s may be treated as a transit time of injected holes in the single-layered LDPE sample or that in the *Ref*/*NC*(*G*) sample.

In summary, the results of SPD measurements on multi-layered samples provide convincing evidence that bipolar charge injection takes place under the experimental conditions of this study, though the positive charge carriers (holes) dominate the transport in reference LDPE. This conclusion can also be extended to the case of single-layered samples, as a similar magnitude of the initial field strength is induced inside the material bulk.

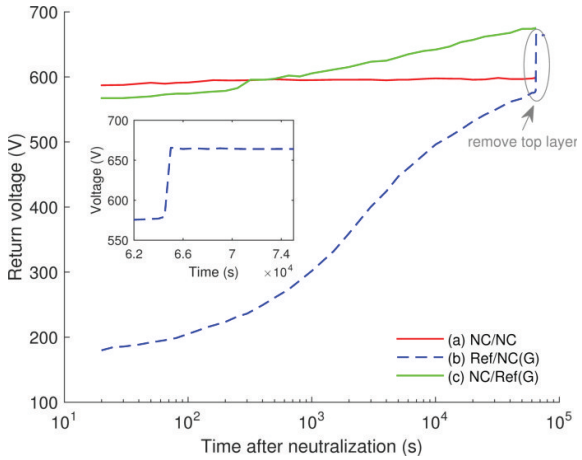

Figure 4.19. Return voltages measured after short-circuiting multi-layered samples for 10 s at the end of SPD measurements. The inset shows the measured potential before and after removal of the top layer of sample *Ref/NC*(*G*).

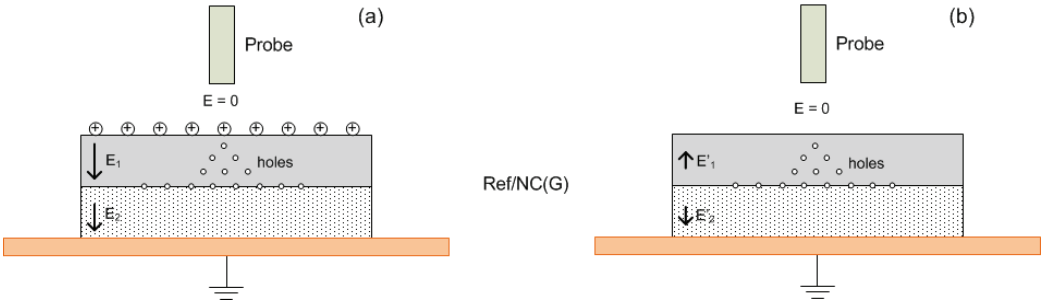

Figure 4.20. Schematic illustration of charge distribution and electric field (a) prior to and (b) immediately after short-circuiting the *Ref/NC*(*G*) sample.

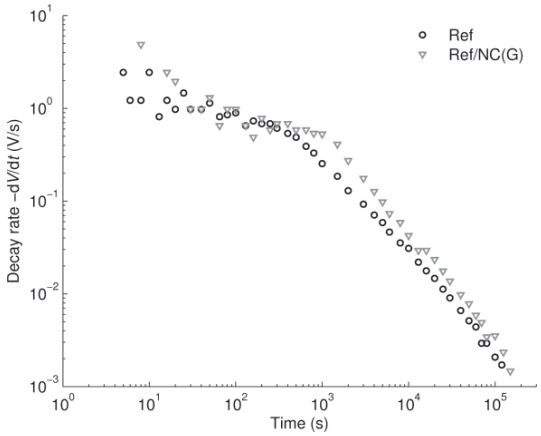

Figure 4.21. Decay rate of surface potential on reference LDPE and *Ref/NC*(*G*).

4.2.3. Charge mobility evaluations

Dated back to the 60s and 70s of the last century, the main interest of SPD measurements was related to the explanation of the crossover phenomenon that was first reported by Ieda *et al.* [110]. The crossover phenomenon is referred to a faster decay process recorded on dielectric materials being charged to a higher surface potential, so that decay curves cross

over each other if their initial surface potentials are different. The crossover phenomenon can be attributed to the non-linear behavior of the dielectric exposed to high electrical fields. One of the models that provide a reasonable explanation for this was developed by Sonnonstine and Perlman in 1975 [93]. It accounts for the injection of charge carriers from the air–insulation interface and their transport in the bulk of the dielectric. By using the model, the authors derived the effective mobility of charge carriers [38] which is proportional to the initial decay rate and inversely proportional to the square of the initial field:

$$-\left(\frac{\mathrm{d}V}{\mathrm{d}t}\right)_{t=0} = \frac{\mu}{2}\left(\frac{V}{L}\right)^2_{t=0}. \tag{4.3}$$

Thus, this method can be applied to attain mobility of holes in reference LDPE where they are injected from the air–insulation interface and dominate in charge transport as discussed in section 4.2.2 (the same seems to be also valid for the studied LDPE nanocomposites). An alternative way relies on the observation of the knee point in the decay rate characteristics, being attributed to the transit time of charges through the bulk [108]. However, since a knee point is only discernible for reference LDPE at room temperature (Figure 4.17b), this method is solely applicable in this particular case.

Values of the effective mobility of holes in LDPE at room temperature calculated by the two described methods are respectively 4.2×10^{-15} and 2.4×10^{-15} $m^2\ V^{-1}s^{-1}$, which can already be considered as fairly agreeing with each other. The hole mobility in PE within the range $(1-5)\times10^{-15}$ $m^2V^{-1}s^{-1}$ at electric fields of $(2-4)\times10^7$ V/m was obtained in numerous investigations of surface charge decay [34, 37, 39, 40], space charge measurements [43] as well as measurements of transient currents [25]. Marginally higher values of mobility can also be found in literature [38].

The results obtained by the procedure proposed by Sonnonstine and Perlman are illustrated in Figure 4.22. As seen, the effective mobility of holes is lower for the nanocomposites, and this difference exaggerates at higher temperatures. The reduction in charge mobility in nanofilled materials has also been reported in [64, 103]. Lewis [68] has recently explained the reduced mobility of charge carriers in nanocomposites by modifications of the energy structure of the amorphous phase in semi-crystalline PE induced by nanoparticles. The author attributes the hole transitions in unfilled PE to tunneling between donor and acceptor sites in the interfacial regions of the amorphous phase [47]. Thereby, the presence of nanoparticles in the amorphous phase of nanometer size modifies the height of the energy barrier for tunneling as well as the tunneling distance. As a consequence, the time for hole transitions is lengthened and charge carrier mobility decreases [68].

The activation energy $W_{a\mu}$ for carrier mobility can be obtained by using Arrhenius dependence similar to eqn. (4.2):

$$\mu(T) = \mu_0 \exp\left(-\frac{W_{a\mu}}{kT}\right), \tag{4.4}$$

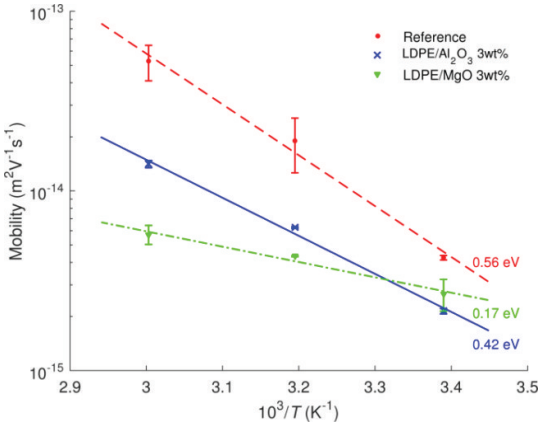

Figure 4.22. Temperature dependences of charge carrier (hole) mobility derived based on Sonnonstine and Perlman model.

Table 4.3. Activation energies (in eV) derived from current density and carrier mobility for reference LDPE and its nanocomposites.

Materials	Derived from current density	Derived from charge mobility
LDPE	0.85	0.56
LDPE/Al_2O_3 3wt%	0.43	0.42
LDPE/MgO 3wt%	0.35	0.17

where $\mu(T)$ represents charge mobility at temperature T and μ_0 is a constant. The respective calculated activation energies are indicated in Figure 4.22 and provided in Table 4.3. The latter also provides activation energies derived earlier from the DC conductivity measurements. It is noteworthy to observe that the values of the activation energies for LDPE/Al_2O_3 nanocomposite obtained by both methods are close to each other. However, this is not the case for reference LDPE and LDPE/MgO nanocomposite. By recalling the expression for the current density j

$$j = qE\sum_i n_i\mu_i \,, \tag{2.1}$$

it is suggested that for the latter two materials, the density n_i of mobile charge carriers also increases with temperature.

The electrical conduction in PE has been discussed in a variety of works. A short summary provided in [35] shows that different conduction mechanisms may dominate in the material, depending on experimental conditions. Although the presented values of activation energy vary broadly, a range of 0.84–1.2 eV appears common and the activation energy gained in this study is close to the lower limit of the indicated interval. On the other hand, not much information can be found on the activation energy for conduction in PE nanocomposites. The lower values of the activation energy for the nanofilled LDPE presented here indicate that the conduction processes are less temperature-dependent, which would lead to less pronounced field enhancement and space charge accumulation in HVDC cable insulation, which is a positive aspect brought about by the nanofillers.

4.2.4. Plot of −tdV/dt *vs.* log(t)

The plot of $-t\mathrm{d}V/\mathrm{d}t$ *vs.* $\log(t)$ has been widely employed for representing data of SPD measurements as it may reveal information about charge trapping and transport in disordered solids. As pointed out in [51], for the case of an exponential potential decay $V = V_0\exp(-t/\tau)$, the peak in this plot corresponds to the characteristic time τ. The exponential potential decay is however rarely observed in practice. The peak of the curve $-t\mathrm{d}V/\mathrm{d}t$ *vs.* $\log(t)$ for a general decay shape can be related either to an average transit time of charge carriers, provided that charge injection takes place, or to an average residence time of charges in trapping sites in case of dominating surface de-trapping [51]. The later hypothesis has been linked to the demarcation energy model [49], according to which the release of charges from traps at particular time t yields potential decay $\mathrm{d}V/\mathrm{d}t$ and, hence, the plot of $-t\mathrm{d}V/\mathrm{d}t$ *vs.* $\log(t)$ shows a dynamic border between the filled (deeper) and the emptied (shallower) localized states. Thus, the energy depth of traps E_t is determined by time t that charges spend in them:

$$E_t = kT\ln(\upsilon_0 t). \tag{4.5}$$

Since $-t\mathrm{d}V/\mathrm{d}t$ is proportional to the trap density and time t is related to the trap depth, the characteristic $-t\mathrm{d}V/\mathrm{d}t$ *vs.* $\log(t)$ provides an image of trap energy distribution in considered materials.

The model of demarcation energy developed earlier [49] has been recently reconsidered [111]. It has been suggested in the latter work [111] that the trap density at a certain energy level E_t can be quantified as:

$$N(E_t) = \frac{\varepsilon_0\varepsilon_r}{kTf_0(E_t)\delta Lq}\frac{t\mathrm{d}V}{\mathrm{d}t}, \tag{4.6}$$

where $f_0(E_t)$ is the rate of initial occupancy of traps that is assumed to be ½; δ is the thickness of injected charge layer; L, k, T, and q have the same meaning as defined earlier. The authors [111] presumed that the injected charges are homogeneously distributed within a thin layer of 2 μm without providing convincing experimental evidences. This assumption therefore needs to be verified. To avoid this ambiguity, we utilize here the plots of $-t\mathrm{d}V/\mathrm{d}t$ *vs.* $\log(t)$ and $t\mathrm{d}V/\mathrm{d}t$ *vs.* E_t for presenting the image of the trap energy distribution.

The plots of $-t\mathrm{d}V/\mathrm{d}t$ *vs.* $\log(t)$ for reference LDPE obtained at different temperatures are shown in Figure 4.23a. At room temperature, the characteristic shows a broad peak with a shoulder. The time corresponding to the shoulder (~10^3 s) is close to the transit time of charge carriers, whereas the peak time (~10^4 s) is longer and appears to be the average residence time of charges in deep traps. As temperature rises, the peaks become narrower and the shoulder is less pronounced. One can derive the value of the attempt-to-escape frequency ν_0 by using the characteristics of $-t\mathrm{d}V/\mathrm{d}t$ *vs.* $\log(t)$ obtained at different temperatures with an assumption of temperature-invariant distribution of trap energy [50]. The calculation provides a value $\nu_0 \approx 4\times10^8$ s^{-1} and the trap depth at maximum density is $E_t \approx 0.72$ eV (Figure 4.23b). Both the derived values appear to be much lower than the commonly accepted parameters (ν_0 in order of 10^{12} s^{-1} and $E_t \approx 1.0$ eV). This discrepancy might be attributed to the fact that the decay is

controlled by more than a single mechanism. It should be underlined that by using the same procedure [50] even lower levels of the attempt-to-escape frequency ($v_0 = 2\times10^5$ s^{-1}) and of the trap depth ($E_t \approx 0.36$ eV) have also been found for polypropylene [51].

In Figure 4.24, the energy distributions of traps are compared for the reference LDPE and LDPE/Al_2O_3 nanocomposite by using the attempt-to-escape frequency $\nu_0 \approx 6\times10^{12}$ s^{-1}, which is estimated assuming $v_0 = kT/h$ [45] with h being Planck's constant. For the reference material, the distribution is characterized by a peak at ~1.0 eV, which may be associated with trapping centra revealed by measurements of TSD currents and attributed to physical defects in amorphous–crystalline interfaces as well as in crystalline region of PE [112]. For the nanofilled material, the image of trap distribution shifts to deeper trap energy. A shoulder is also found at ~1.0 eV, suggesting an identical origin of traps as for those in reference LDPE. In addition, the trap energy distribution of the nanocomposite implies a peak arising outside of the measurement window (at time exceeding 4.2×10^5 s) that can be associated with a deeper trap level ($E_t > 1.1$ eV). The appearance of this trapping level is most likely caused by the presence of nanofillers in the material; in particular in the interfacial region between nanofiller

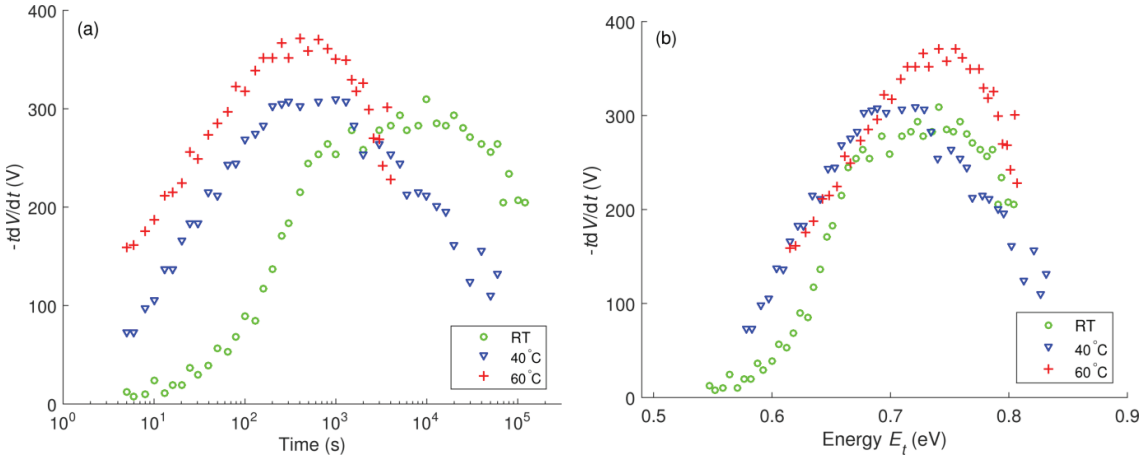

Figure 4.23. Plots of (a) $-t\mathrm{d}V/\mathrm{d}t$ *vs.* log(t) and (b) $-t\mathrm{d}V/\mathrm{d}t$ *vs.* E_t obtained at different temperatures for reference LDPE.

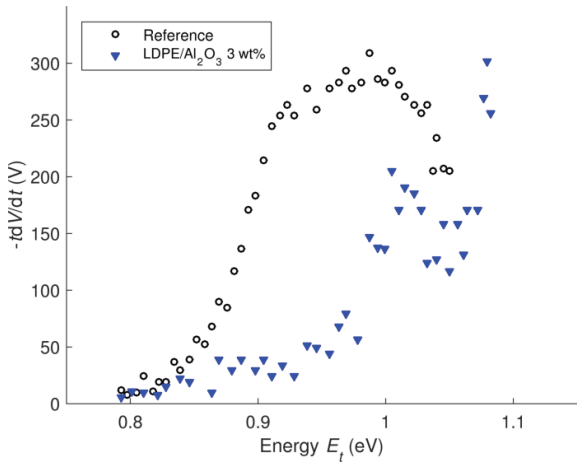

Figure 4.24. Trap energy distributions in reference LDPE and LDPE/Al_2O_3 3wt% nanocomposite.

particles and the polymer base. Further study on the trap depth in LPDE and LDPE/Al_2O_3 nanocomposite is to be presented in section 4.3 by using TSD current measurements.

4.2.5. Calculations of external current densities

During SPD measurement under open circuit configuration, the total current density in an elementary volume of a dielectric is zero:

$$j(x,t)+\frac{\partial\left(\varepsilon E\left(x,t\right)\right)}{\partial t}=0\,. \tag{4.7}$$

Here, $j(x,t)$ is space- and time-dependent conduction current density and the second term represents the displacement current. The externally measurable conduction current density through the insulation can be defined as:

$$J(t)=\frac{1}{L}\int_0^L j(x,t)\,\mathrm{d}\,x\,. \tag{4.8}$$

By substituting eqn. (4.7) into eqn. (4.8) and noting the flat frequency response of the permittivity ε for LDPE and its nanocomposites [113], one obtains

$$J(t)=-\frac{\varepsilon}{L}\int_0^L\frac{\partial E\left(x,t\right)}{\partial t}\mathrm{d}x=-\frac{\varepsilon}{L}\frac{\mathrm{d}V(t)}{\mathrm{d}t}\,. \tag{4.9}$$

Equation (4.9) establishes a relationship between the conduction current density in SPD experiments and the decay rate of the measured potential. The current density is thus calculated and its dependence on electric field is examined in this section. Here, the average magnitude of the electric field induced in the insulation $E = V/L$ is used.

By presenting the obtained transient current density *versus* electric field in log–log plot, Schottky, and Poole–Frenkel plots, one may examine the conduction mechanism in the studied materials in a similar manner as shown in section 4.1.1.4. As exhibited in Figures 4.25a–4.27a, SCLC appears to be the most suitable conduction mechanism in LDPE, whereas neither Schottky injection mechanism nor Poole–Frenkel mechanism satisfactorily explain the behavior of the conduction current density J at all considered temperatures.

The field dependencies of the current densities in both nanocomposites are similar and thus only results on LDPE/Al_2O_3 are illustrated (Figures 4.25b–4.27b). The derived parameters m and ε_r of these dependencies are provided in Table 4.4 for comparison. For the nanocomposites, the current density curves show a knee point at which the slope changes and, hence, the characteristics can be divided into two regions as indicated in the figures. It is noteworthy that the time corresponding to the observed knee point is close to the transit time calculated by using the hole mobility deduced in section 4.2.3. Thus, the rapid decrease of the current densities within the first region can be explained by a transient process followed the charge injection at the air–insulation surface. As the injected charges reach the counter electrode, the field dependence of the current densities become less pronounced, as shown in

the second region. Parameters m and ε_r are thus calculated only in the latter region for avoiding the effect of the fast transient process at the initial stage. As seen, the power factor m in the dependency $J \propto E^m$ is significantly higher for both nanocomposites as compared to that of reference LDPE, indicating the impact of the fillers on the conduction. Nevertheless, similarly to LDPE, the electrical conduction in the nanocomposites might be governed by SCLC mechanism rather than Schottky injection or Poole–Frenkel mechanisms.

Table 4.4. Calculated parameters in characteristics of J *vs.* E. Note that the obtained values of ε_r below 1 do not have physical significance.

Characteristics	Calculated parameters	LDPE			LDPE/Al_2O_3 NC			LDPE/MgO NC		
		RT	40 °C	60 °C	RT	40 °C	60 °C	RT	40 °C	60 °C
$J \propto E^m$	m	4.3	3.9	2.4	9.8	9.9	8.9	11.5	9.6	5.6
Schottky	ε_r	0.48	0.35	0.64	0.15	0.13	0.14	0.12	0.14	0.30
Poole–Frenkel	ε_r	0.8	0.6	1.7	0.18	0.16	0.18	0.14	0.17	0.44

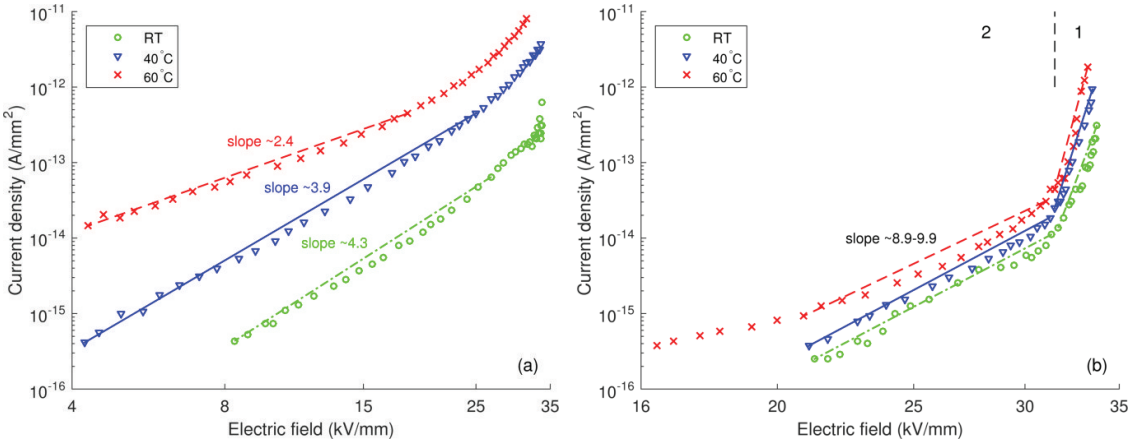

Figure 4.25. Log–log plot of J *vs.* E for (a) reference LDPE and (b) LDPE/Al_2O_3 3wt% nanocomposite at various temperatures. Regions 1 and 2 in figure (b) are featured by different slopes of the dependencies.

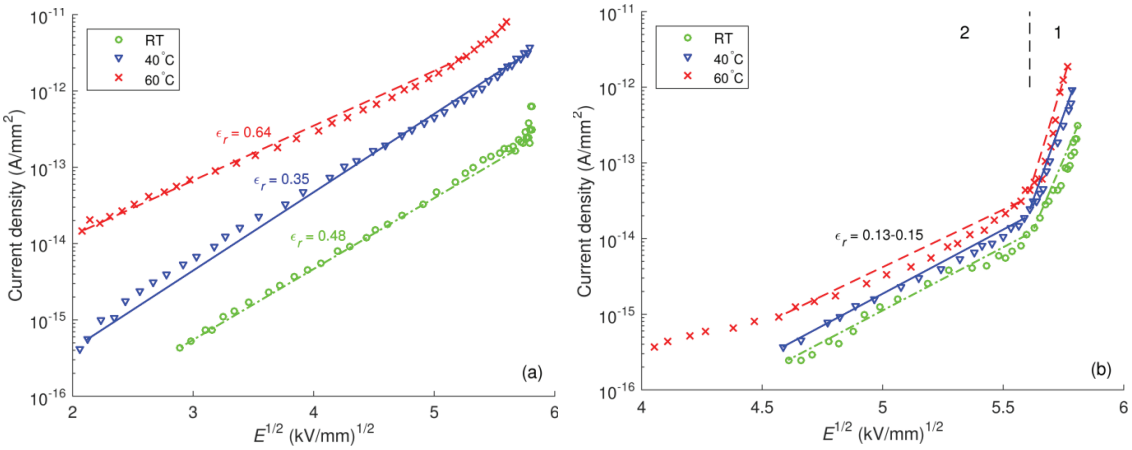

Figure 4.26. Schottky plot for (a) reference LDPE and (b) LDPE/Al_2O_3 3wt% nanocomposite at various temperatures. Regions 1 and 2 in figure (b) are featured by different slopes of the dependencies.

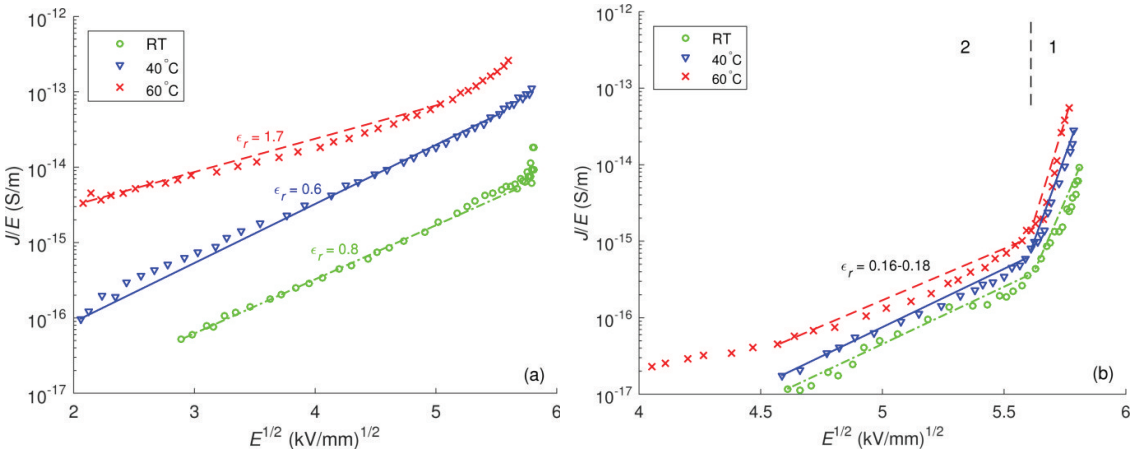

Figure 4.27. Poole–Frenkel plot for (a) reference LDPE and (b) LDPE/Al_2O_3 3wt% nanocomposite at various temperatures. Regions 1 and 2 in figure (b) are featured by different slopes of the dependencies.

4.3. Results of thermally stimulated discharge current tests

As revealed by the demarcation energy model, LDPE is featured by trap depth ~1.0 eV while deeper traps should be present in Al_2O_3-nanofilled LDPE. Since it was not possible to detect the deepest level of traps for the latter material by using isothermal experimental conditions, the investigations were complemented by measurements of discharging currents in thermally stimulated conditions focusing on determining trap depth in LDPE/Al_2O_3 3 wt% nanocomposite.

4.3.1. Background

Measurements of TSD currents comprise an application of an external electric field to a material sample thus causing polarization build-up and/or charge generation in the material. Subsequently, the sample is heated up while removing the poling field, stimulating this way the reorientation of dipoles and/or the release of charge carriers from traps. The resulting current density due to the dipole reorientation is defined as [114]:

$$J(T) = \frac{N_d u^2 E_p}{3kT_p\tau_0}\exp\left[-\frac{W_{at}}{kT} - \frac{1}{\beta\tau_0}\int_{T_0}^{T}\exp\left(-\frac{W_{at}}{kT}\right)\mathrm{d}T\right], \tag{4.10}$$

where N_d and u denote dipole concentration and moment, respectively; E_p and T_p are poling field and temperature, respectively; τ_0 is a time constant; W_{at} is an activation energy; and β being a heating rate. This equation can be rewritten as:

$$J = B_1\exp\left[-s + B_2\int_{s_0}^{s}\exp(-s)s^{-2}\mathrm{d}s\right], \tag{4.11}$$

where $s = W_{at}/kT$, $B_1 = N_d u^2 E_p/3kT_p\tau_0$, and $B_2 = W_{at}/k\beta\tau_0$. The discharging current caused by de-trapping of charge carriers can also be described by eqn. (4.11) with some modifications in the expressions for parameters $B_{1,2}$, see [115].

For the low temperature tail of the TSD current, the second component in the square bracket of eqn. (4.11) is close to zero so that the current density becomes

$$J = J_0 \exp\left(-\frac{W_{at}}{kT}\right), \tag{4.12}$$

where J_0 is a constant. Thus, one may determine W_{at} using the initial increase of the TSD currents that is referred to as the initial rise method [116]. Alternatively, the fitting of experimental data can be performed using the theoretical TSD current relation (4.11) [117].

Provided that the dipole reorientation dominates during the depolarization process, the relaxation time τ of this process can be found from measurements [114] as:

$$\tau = -P(T)/J(T) = \int_{t(T)}^{\infty} J(t')\,\mathrm{d}t'/J(T). \tag{4.13}$$

Thus, the activation energy W_{at} can be attained from the temperature dependence of $\tau(T)$:

$$\tau = \tau_0 \exp\left(\frac{W_{at}}{kT}\right), \tag{4.14}$$

which is also known as Bucci plot [118].

4.3.2. Experimental results and discussion

The full TSD current obtained for the unfilled LDPE is presented in Figure 4.28 together with the currents measured during partial heating cycles. As seen, the TSD spectrum of LDPE is characterized by two peaks of opposite polarities, which were observed at ~30 and ~64 °C. Similar TSD peaks have been reported in [112] within temperature range 30–60 °C and were associated with the release of charges from traps. As the peak temperatures are close to that of the α relaxation in PE, charge de-trapping is probably related to or enhanced by the motion of PE chains [112]. In contrast, the TSD currents obtained with partial heating show only negative peaks, thus contributing to the peak at ~64 °C in the full TSD spectrum. The positive current of the full TSD spectrum within the temperature interval 20–40 °C appears to be a superposition of the positive partial heating currents rather than being a separate TSD peak. It is noteworthy to mention that polarity reversal in the open-circuit TSD currents was observed in [119] for polyethylene terephthalate (PET) and it was correlated with the change in the polarity of surface charges. Since surface charges and surface potentials are directly proportional, we tested this hypothesis by recording the latter using conditions with the same heating rate (3 K/min). In contrary to the result reported in [119], it appeared that no polarity change was found in our measurements, see Figure 4.29. Hence, the reason for the polarity reversal of TSD currents in the unfilled LDPE is still unclear. In other work [106], similar change in the polarity of TSD currents has been attributed to the accumulation of space

charges and the blocking electrodes. This hypothesis needs to be verified for LDPE used in the present study and that requires further investigation. Note that the magnitudes of the currents at partial heating are much lower than that of the full TSD spectrum that can be attributed to the fast decay of surface potentials at elevated temperatures, as shown in Figure 4.29.

According to eqn. (4.10), the magnitude of TSD currents due to polarization is linearly proportional to the applied electric field. However, this relationship is not applicable in case of TSD currents caused by the release of charges from traps [115]. The difference in the TSD characteristics can thus be utilized for examining whether polarization is the main contributor to the observed process [120] and was implemented in this study by varying the grid voltage for the corona charging from 1 to 3 kV. The poling field can be quantified based on the surface potentials attained immediately after charging. The shape of TSD spectra was found

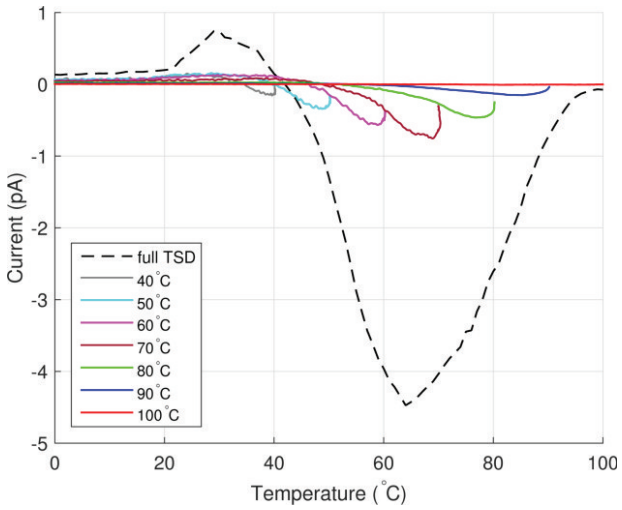

Figure 4.28. Full TSD spectrum (dashed curve) and TSD currents obtained in partial heating cycles (solid curves) for pure LDPE. Final temperatures of heating cycles are indicated in the legend. The grid voltage during poling was 3 kV.

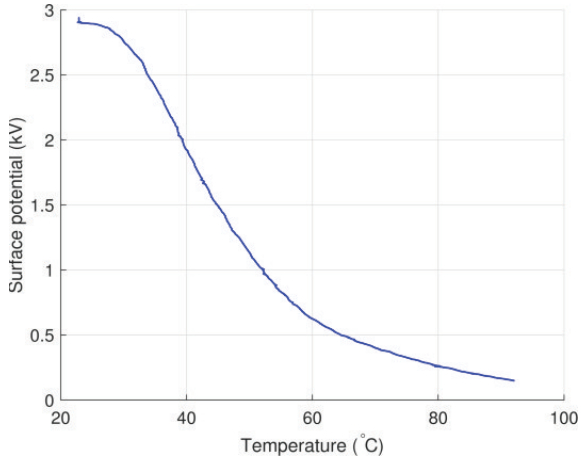

Figure 4.29. Decay of surface potential under thermally stimulated conditions with the heating rate of 3 K/min. The whole test lasted for ~25 min.

to be preserved at different grid voltages. The amount of released charges corresponding to the TSD current is calculated by its integration over time:

$$Q = \int_{t_1}^{t_2} J dt = \frac{1}{\beta} \int_{T_1}^{T_2} J(T) \mathrm{d}T . \tag{4.15}$$

The magnitudes of the charge Q obtained for the second peak in TSD spectrum of LDPE are shown in Figure 4.30 as a function of the poling field. It is notable that the dependence is non-linear suggesting that polarization is not the dominating contributor to the TSD current in the studied LDPE. This is in contrast to the results presented in [121], where a linear relationship between the applied field and the charges released was detected during the thermally stimulated process in oxidized PE using poling fields up to 6 kV/mm. Hence, the TSD current was attributed to the dipole reorientation rather than to the de-trapping process. Based on the results of the present study, it can be postulated that the high field strength (10–28 kV/mm) utilized in our experiments triggers the injection of charges into the material, see section 4.2.2. These charges are further trapped in localized states and released during the TSD process. Thus, the TSD currents obtained in this work are associated with the charge de-trapping.

Data presented in Figure 4.28 yield the activation energies (calculated by the initial rise method) of 1.11 and 1.28 eV for the TSD peaks at ~30 and ~64 °C, respectively. This outcome is in agreement with the trap depth in PE detected earlier by TSD measurements in short-circuit configuration [112].

The TSD currents measured on LDPE/Al_2O_3 nanocomposite are presented in Figure 4.31. By comparing the results with the data for the unfilled LDPE from Figure 4.28, one may notice that the magnitude of full TSD currents is lower and the spectrum is broader for the nanocomposite. The latter may comprise contributions of several TSD peaks. To separate individual peaks, experiments with partial heating were conducted. The currents recorded at the initial rise of partial heating cycles are provided in Figure 4.32 as a function of the reciprocal of temperature. From this plot, the slopes of the dependencies yield the activation energies varying mainly in the range between 1.7 and 2.3 eV.

A result of the alternative approach based on applying the fitting procedure described in [117] is illustrated in Figure 4.33 by considering the first peak of Figure 4.31. It can be noticed that the measured current profile featured by the peak at 33 °C and the shoulder at 35.5 °C. However, a fairly well agreement was still observed when using a single TSD peak at 35.5 °C for fitting the experimental data, noting that the steep front of the peak at 33 °C is hardly reproducible. The fitting procedure provided the activation energy of 2.2 eV for the considered current profile. By applying the method for the remaining partial heating currents, the activation energies of 1.7–2.2 eV were obtained, which are similar to the range derived from the initial rise method.

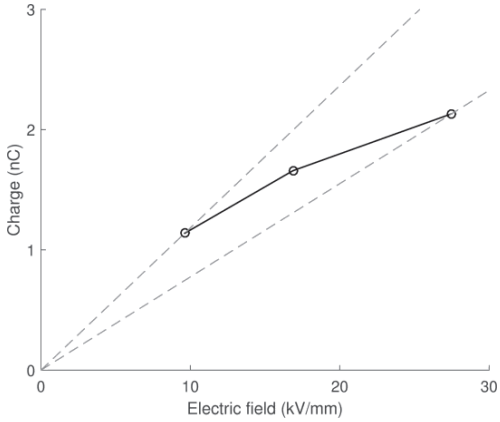

Figure 4.30. Amount of charges released as a function of the poling field for LDPE. The dashed lines show linear proportion.

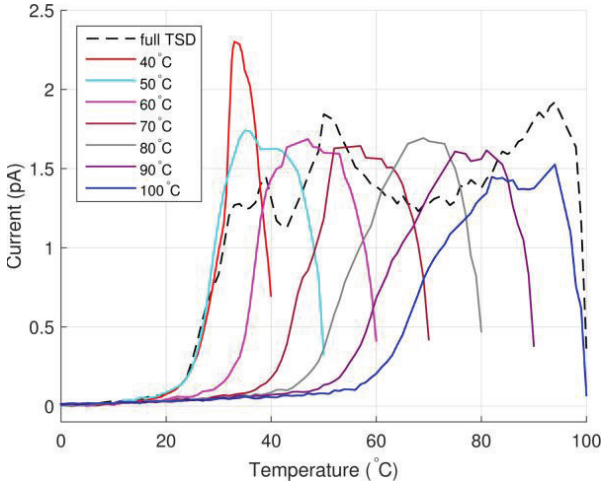

Figure 4.31. Full TSD spectrum (dashed curve) and TSD currents in partial heating (solid curves) for LDPE/Al_2O_3 nanocomposite. Final temperatures of heating cycles are indicated in the legend. The grid voltage during poling was 3 kV.

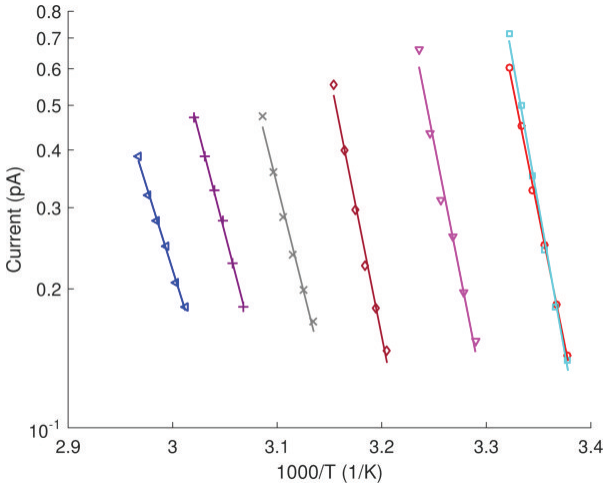

Figure 4.32. Temperature dependence of TSD currents in initial rise obtained in partial heating cycles. The calculated activation energies (from left to right) are respectively 1.44, 1.74, 1.80, 2.26, 2.28, 2.24, and 2.52 eV.

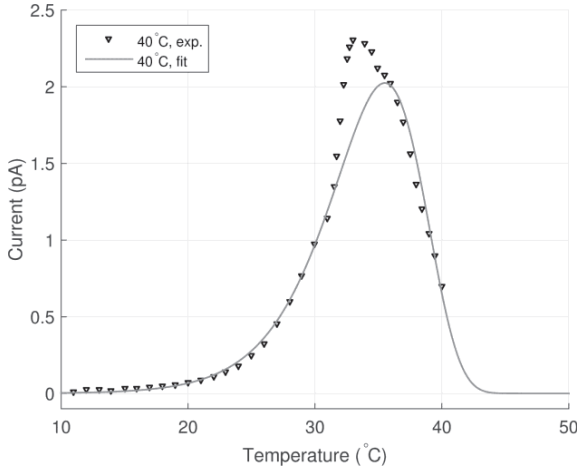

Figure 4.33. Example of fitting the TSD current measured at partial heating with the final temperature of 40 °C (marker) by using Cowell and Woods's method. For the fitting curve (solid): activation energy E_a = 2.2 eV, temperature corresponding to maximum current T_m = 35.5 °C.

It is suggested that the charge de-trapping is the major contributor to the TSD currents in the LDPE nanocomposite. This is because of the restriction in the movement of polymeric chains introduced by the presence of nanofillers [8] (exhibited also by reduction of material's permittivity). The range of trap depth is thus much higher in the LDPE/Al_2O_3 nanocomposite as compared to the unfilled material and this conclusion is in line with the results derived from the measured SPD using the demarcation energy model, see section 4.2.4. The deep traps in polymer nanocomposites are usually assumed to be located within the interaction zone, *i.e.* the interfacial region between the nanofillers and the polymer matrix [8]. It has been suggested in [69] that owing to the difference in dielectric permittivity of inorganic nanofiller and the base polymer in LDPE/MgO nanocomposite, potential wells (as charge traps) are formed at the filler–polymer interfaces when the material is exposed to an external electric field. The trap depth greatly depends on the applied electric field and they are usually deeper than traps inherently existing in the unfilled polymer. The trap energy of the LDPE/Al_2O_3 nanocomposite revealed in this study is in agreement with the proposed hypothesis [69].

4.4. Simulations of charge transport in insulating materials under DC electric field

This section focuses on analyzing the generation and transport of charge carriers in LDPE and its nanocomposites using the numerical model described in section 3.3. In this model, charges are assumed to be generated in insulating materials by injection at both electrodes and by de-trapping from traps, while they are lost through trapping and recombination processes. Charge transport is characterized by an effective mobility controlled by hopping between shallow traps.

4.4.1. Charge transport in low-density polyethylene

The set of input parameters which provided a closest match between the computed and measured results is presented in Table 4.5. The mobility of holes was set close to the values deduced from the measurements (section 4.2.3), while the effective mobility of electrons was

approximately one order of magnitude higher than the mobility of holes (as has been found in [40, 43]). It should be noted that the potential barrier height at the anode was set to be lower than that at the cathode as the injection of holes from a semiconducting anode was alleviated as compared to the electron injection from a metal cathode [43]. Furthermore, the barrier heights for de-trapping ~1.0 eV were selected in accordance to trap depth level revealed by the results of TSD currents [112, 121] and in our investigations (sections 4.2.4 and 4.3). These levels of trap depth are also in agreement with the values used in other numerical model [46]. The trap densities ~10^{21} m^{-3} were set based on the results obtained in [122]. The recombination coefficients were adopted from [46]. Finally, the trapping coefficients were adjusted to achieve the best fit. The commonly accepted relative permittivity $\varepsilon_r = 2.3$ was used for LDPE.

The results of the simulations are presented in Figure 4.34 together with experimental data. Note that the rapid reduction of the measured currents within first 50–70 s, particularly prominent at room temperature and 40 °C in the figure, is most likely associated with the decaying displacement current arising due to the application of a step voltage. The conduction current component becomes dominating only at longer instants after voltage application ($t \geq 10^2$–10^3 s) and, hence, simulated and experimental currents can be compared only in this stage. As seen in the figure, the current density at room temperature (~22 °C) predicted by the model agrees well with the measured one. At higher temperatures, the computed characteristics are still in line with experimental data but the agreement is getting worse.

Table 4.5. Parameters used in models for fitting the measured conduction currents on LDPE and its nanocomposites at various temperatures.

Parameters	LDPE			LDPE nanocomposites		
	RT	40 °C	60 °C	RT	40 °C	60 °C
Effective mobilities						
μ_e, $m^2V^{-1}s^{-1}$	3.0×10^{-14}	1.5×10^{-13}	5.5×10^{-13}	1.0×10^{-14}	3.0×10^{-14}	7.0×10^{-14}
μ_h, $m^2V^{-1}s^{-1}$	2.5×10^{-15}	1.2×10^{-14}	5.0×10^{-14}	2.0×10^{-15}	6.0×10^{-15}	1.4×10^{-14}
Trapping coefficients						
t_e, s^{-1}	0.02	0.08	0.25	0.002	0.022	0.13
t_h, s^{-1}	0.01	0.03	0.08	0.002	0.022	0.13
De-trapping barrier heights						
φ_{etr}, eV	0.93	0.96	1.00		1.00	
φ_{htr}, eV	0.93	0.96	1.00		1.00	
Deep trap densities						
N_{etr}, m^{-3}		1.25×10^{21}			6.25×10^{21}	
N_{htr}, m^{-3}		1.25×10^{21}			6.25×10^{21}	
Schottky injection barriers						
φ_K, eV		1.22			1.31	
φ_A, eV		1.16			1.26	
Recombination coefficients						
r_{etrhtr}, m^3s^{-1}		6.4×10^{-22}			6.4×10^{-22}	
r_{etrh}, m^3s^{-1}		6.4×10^{-22}			6.4×10^{-22}	
r_{ehtr}, m^3s^{-1}		6.4×10^{-22}			6.4×10^{-22}	
r_{eh}, m^3s^{-1}		0			0	

Broad maxima appear in the simulated currents and the peaks are shifted to a shorter time as the temperature rises.

Distributions of space charges in the material bulk obtained from the simulations at room temperature are illustrated in Figure 4.35. As seen, the positive carriers dominated over the negative ones throughout the simulated time interval. The dynamics of the space charges in the material can be characterized by their transit times determined as the time duration required for charges traversing through the insulation bulk. The arrival of holes to the cathode and electrons to the anode can be traced by using the profiles of mobile charge density shown in Figure 4.36. Based on that, the transit times of ~100 s for electrons and of ~1000 s for holes can be identified that is consistent with the higher (almost one order of magnitude) mobility of electrons as indicated in Table 4.5. Additionally, the obtained transit times of charge carriers are very close to values calculated as $t_{tr} = L^2/(\mu V_0)$ assuming insignificant accumulation of space charges in the bulk. As it is observed in Figure 4.35c, the latter is true for the time shorter than the transit time.

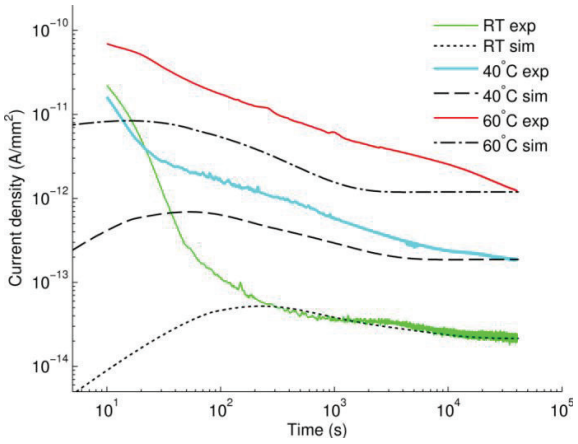

Figure 4.34. Simulated (referred as "sim" in the legend) and experimental (exp) current densities on LDPE at various temperatures.

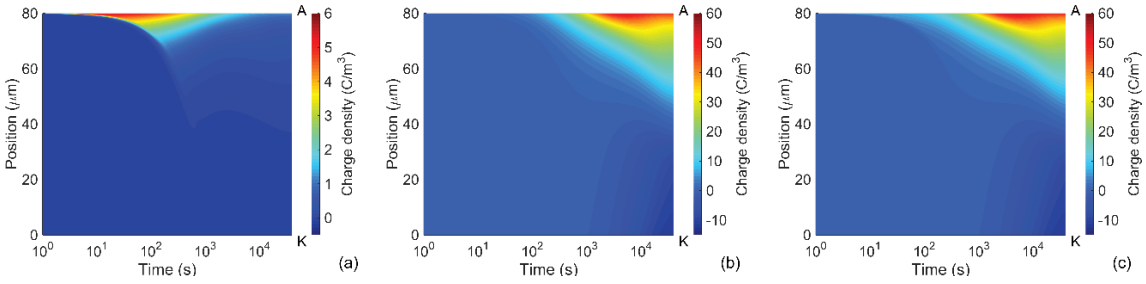

Figure 4.35. Computed charge density distributions in LDPE at room temperature: (a) mobile charges, (b) trapped charges, and (c) total space charges. Positions of the anode and cathode are indicated by letters A and K, respectively.

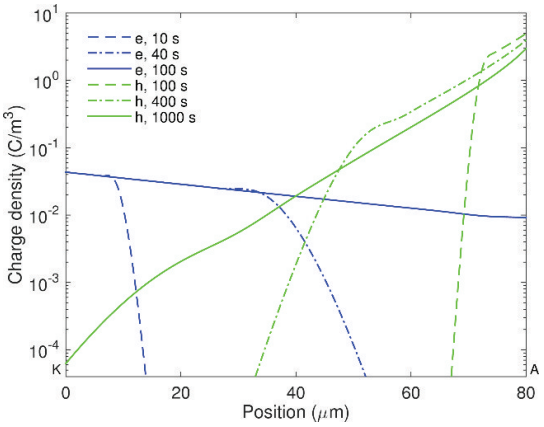

Figure 4.36. Density profiles of mobile electrons (e) and holes (h) in LDPE at room temperature computed at indicated time.

During the transport of injected holes towards the cathode, their density reduces remarkably due to the trapping process and most of the mobile carriers concentrate within a thin layer (5–10 μm) at the vicinity of the anode (Figure 4.35a). The accumulation of mobile positive carriers in the bulk takes place mostly within first 100 s; thereafter, a reduction in their density can be observed. As seen in Figure 4.35b, immobile positive charges are gradually built up in the vicinity of the anode within the time interval 10^2–10^3 s and its density becomes much higher after 10^3 s. Thus, the immobile charges are strongly dominating over the mobile ones in the material bulk. The dynamics of positive charge accumulation are controlled by charge injection before 10^2 s and by charge trapping after 10^3 s, while a transition process takes place in the time interval 10^2–10^3 s. A similar tendency is also observed for the negative charges. In particular, the onset of negative charge accumulation in trapping sites close to the cathode is observed at ~10^3 s, which results in a considerable amount of trapped electrons in the bulk after 10^4 s. The variation in the density of the mobile charges leads to the corresponding changes in the simulated conduction current and, hence, a broad maximum appears at time 200–300 s. It should be emphasized that the contribution of mobile electrons to the conduction current cannot be neglected in spite of their remarkably lower density as compared to that of mobile holes. This is because of the higher mobility of electrons than that of holes.

The distribution and evolution of space charges in LDPE at elevated temperatures are not shown here as the main features presented above are preserved. However, one should mention three distinctions, namely, (a) higher levels of charge densities owing to a larger amount of charges injected at elevated temperatures; (b) faster charge transport processes as charge carriers become more mobile with increasing temperature; and (c) the saturation in the computed conduction currents (see Figure 4.34) observed at ~10^4 s for 40 °C and at 2×10^3 s for 60 °C. The last feature is not observed within the considered time interval (up to 4×10^4 s) in the simulation at room temperature.

4.4.2. Charge transport in low-density polyethylene based nanocomposites

In this section, charge transport in LDPE filled with 3 wt% of Al_2O_3 and MgO nanoparticles is studied. Since the respective volume fractions of the nanofillers are low (0.7–

0.8 vol%), the model used in section 4.4.1 can also be employed for heterogeneous materials taking into account the effective medium approximations of properties of the composites. As the experimental results are very close for both nanocomposites under consideration, current densities obtained on LDPE/Al_2O_3 3 wt% are employed for comparison with the simulated ones.

4.4.2.1. Model parameterization

The substantial decrease in the measured DC conductivity of LDPE filled with 3 wt% of nanofillers as compared to the unfilled LDPE is believed to be associated with the weakened charge transport in the nanofilled materials. By recalling the well-known expression for the conduction current, eqn. (2.1), the reduction in the DC conductivity of nanocomposites can be quantitatively related to the decrease in the density of charge carriers and/or the effective mobility.

Despite the density of mobile charge carriers cannot be monitored separately from trapped carriers in space charge measurements, the concentration of mobile charges is anticipated to be lower in nanocomposites. Significant suppression of space charge accumulation in PE nanocomposites observed in various works [56, 67, 70] has been interpreted by the presence of deep traps. As an example, the trap depth in LDPE/MgO nanocomposite may be 1–5 eV with the highest level corresponding to the applied field strength of ~200 kV/mm [69]. Analyzing the measured TSD currents, we found the trap depth in LDPE/Al_2O_3 nanocomposite varying in a range ~1.7–2.3 eV and these deep traps have been attributed to the presence of nanofillers. Based on these findings, the trap depth should be set higher than that for unfilled LDPE. In addition, increased concentrations of traps has been found in nanofilled PE [122]. Such modifications are expected to enhance the capturing of charge carriers injected from the electrodes that may result in thinner layers of homocharges in the vicinity of the electrodes as compared to the case of pure material. These, in turn, reduce the field strength at the interfaces and so decrease the injected currents [122]. This phenomenon can be identified as a screening effect produced by accumulated homocharges. According to the analysis [70], the screening effect yields a higher barrier height for charge injection at electrodes in case of PE-based nanocomposites as compared to the unfilled counterpart. Considering these modifications in material properties brought about by nanofillers, the barrier heights for charge injection at both electrodes were increased by up to 0.1 eV and the density of deep traps rose in five times for the nanocomposites as compared to the reference LDPE (see Table 4.5). As regards the mobility of charge carriers in nanocomposites, the reduced values found experimentally (section 4.2.3) were taken into account in the simulation.

According to results of the dielectric spectroscopy measurements [113] conducted on LDPE and LDPE/Al_2O_3 3 wt% nanocomposite in frequency range 10^{-4}–10^{3} Hz and at three temperatures considered in the model, the relative permittivity was slightly higher (maximum 5%) for the nanocomposite than for reference LDPE. Additionally, the frequency dependencies of the relative permittivity were weak for both materials. The relative permittivity of LDPE nanocomposite was therefore set to 2.3 as for the unfilled LDPE, albeit the experimental results are not shown here for the sake of brevity.

4.4.2.2. Simulated results

The experimental and computed currents in the nanomaterial are compared in Figure 4.37. Unlike the case of pure LDPE, the conduction current densities predicted by the model show good agreement with the measured ones at all three considered temperatures. At each temperature, the localized peak in the simulated conduction current appears later for the nanocomposite as compared to reference LDPE (Figure 4.34) due to the lower mobility of charge carriers in the nanofilled material.

Distributions of charge densities in the bulk of the nanocomposite are shown in Figure 4.38 for room temperature. Similarly to the reference LDPE, positive charge carriers are dominating in the material and they are mainly concentrated in a thin layer at the vicinity of the anode. As expected, the amount of charges accumulated in the bulk of LDPE nanocomposite is significantly smaller as compared to that in the reference material. Thus, the maximum density of mobile carriers is almost 50 times lower (compare Figures 4.35a and 4.38a), while the total space charge density is less than 5 C/m^3 in most part of the nanocomposite (positions 0–70 μm) and its maximum at the anode is below 9 C/m^3, Figure 4.38c. In contrast, the space charges with density exceeding 5 C/m^3 propagate deeply into the bulk of the unfilled LDPE and its maximum is at least six times higher (~55 C/m^3), see Figure 4.35c. As a result, the electric field is strongly enhanced inside the reference material, but this is not the case for the nanocomposite. As it is seen in Figure 4.39, the distortion in the electric field distribution in the nanofilled material is negligible at 1h after voltage application and only small (~7%) field enhancement is observed at the vicinity of the cathode at 4×10^4 s. On the contrary, an appreciable enhancement (~25%) can be noticed in the middle of the sample of the unfilled LDPE at 4×10^4 s.

The quantity of accumulated positive space charges (dominating carriers) calculated as

$$Q(t) = \int_0^L q\left[n_h(x,t) + n_{htr}(x,t)\right] \mathrm{d}x \tag{4.16}$$

is presented as a function of time in Figure 4.40 for all three temperatures. As seen, the amount of charge steadily rises with time and eventually reaches a saturation level ~10^{-3} C/m^2. The charge magnitudes are lower in the LDPE nanocomposite for all studied temperatures and the differences are more than one order of magnitude in the short time intervals, whereas they become smaller at longer time. For simulations at elevated temperatures and time exceeding 10^4 s, the total positive charges are comparable in both materials.

4.4.2.3. Influence of different physical processes on charge transport

As discussed above, the weakening in charge transport in nanofilled LDPE as compared to the unfilled counterpart can be attributed to the reduced charge injection at electrode–insulation interfaces, to the decreased charge carrier mobility, to the increased probability of charge capturing in and to the decrease of charge releasing from deep traps. However, it is unclear which process among the above-mentioned mainly contributes to the reduced

conductivity of the LDPE nanocomposite. In other words, what behavior of the insulation is changed most noticeable due to the addition of nanofillers into LDPE?

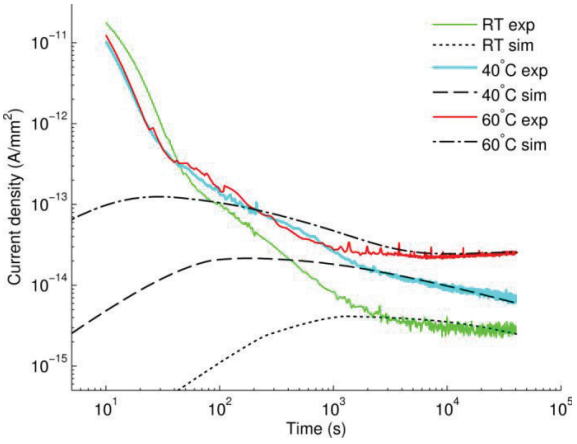

Figure 4.37. Current densities obtained from simulations (sim) and experiments (exp) on LDPE/Al_2O_3 3wt% nanocomposite at various temperatures.

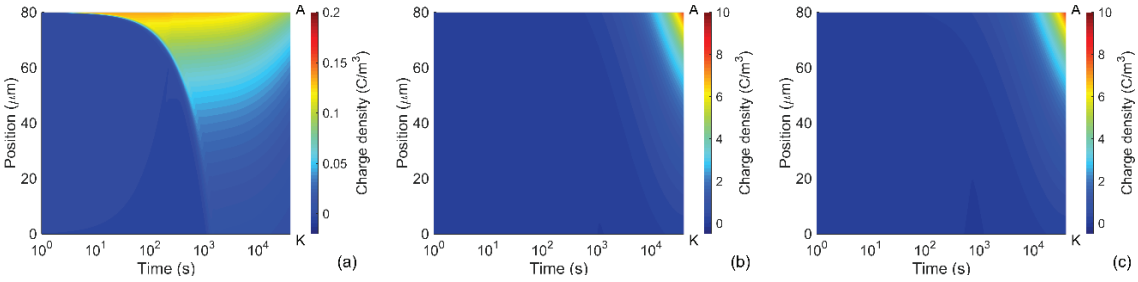

Figure 4.38. Distributions of charge densities in LDPE nanocomposite obtained from simulations at room temperature: (a) mobile charges, (b) trapped charges, and (c) total space charges. Positions of the anode and cathode are indicated by letters A and K, respectively.

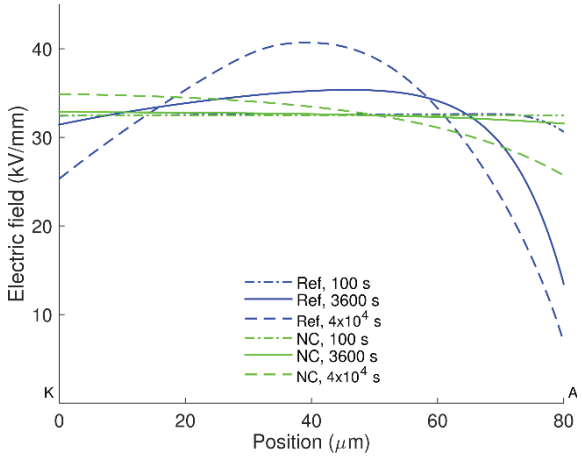

Figure 4.39. Electric field distributions in LDPE without (*Ref*) and with (*NC*) nanofillers at room temperature.

To address this question, we assume that only one type of parameters incorporated in the model for pure LDPE and associated with a certain physical process is modified at a time to the values used in the model of LDPE nanocomposite (Table 4.5), while all other parameters are kept unchanged. Thus, four scenarios are considered as described in Table 4.6 and the obtained results (conduction currents at temperature 40 °C) are illustrated in Figure 4.41, where the simulated currents in LDPE and its nanocomposite are also shown for comparison. As can be seen, the conduction current drops significantly down to the level close to that in the nanocomposite while increasing the injection barriers alone and less pronounced decline is observed in three other situations. The effect of charge mobility on the conduction current is almost the same in the studied time interval, whereas the influence of trap energy (φ_{tr}) and trap density (N_{tr}) is remarkable only at times exceeding 10^4 s. Based on the results of the analysis, we found that the decrease in charge injection at the electrodes mainly accounts for the weakening of conduction in LDPE nanocomposite and so for the suppression of space charge build-up in the bulk.

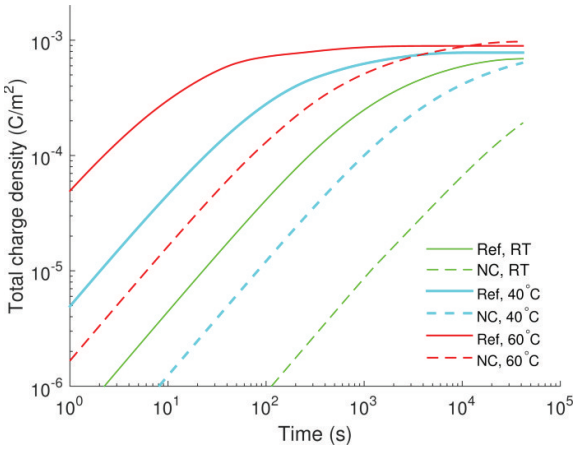

Figure 4.40. Amount of positive charges accumulated in the bulk of LDPE (*Ref*) and LDPE nanocomposite (*NC*).

Table 4.6. Scenarios for simulations with varying parameters. Model parameters of each scenario are the same as for simulating charge transport in LDPE, except for those provided in the right column. Charge mobilities (in $m^2V^{-1}s^{-1}$) are listed in order of increasing temperature (RT, 40 °C, 60 °C).

Scenario	Description	Model parameters	Modified parameters
#1	Reduction of charge injection at electrodes	Charge injection barrier heights as for the nanocomposite, all other parameters as for LDPE	φ_K = 1.31 eV φ_A = 1.26 eV
#2	Reduction of charges released from deep traps	De-trapping barrier heights as for the nanocomposite, all other parameters as for LDPE	φ_{etr} = 1.00 eV φ_{htr} = 1.00 eV
#3	Reduction of charge carrier mobility	Mobility of electrons and holes as for the nanocomposite, all other parameters as for LDPE	$\mu_e = 1\times10^{-14}$; 3×10^{-14}; 7×10^{-14} $\mu_h = 2\times10^{-15}$; 6×10^{-15}; 1.4×10^{-14}
#4	Increase of trap densities	Trap densities as for the nanocomposite, all other parameters as for LDPE	$N_{etr} = 6.25\times10^{21}$ m^{-3} $N_{htr} = 6.25\times10^{21}$ m^{-3}

The contribution of charge recombination to the conduction current is examined by considering charge transport models with and without accounting for this particular process. The simulated conduction currents in both materials are compared in Figure 4.42. As it is found, charge recombination is essential in pure material and in the nanocomposite at 60 °C. Neglecting this process yields a rapid rise of the simulated currents, especially at elevated temperatures. The marked increase in the conduction currents obtained in the model without recombination is due to the excess of mobile charges in the bulk, which would be neutralized if recombination is included. In this context, it is interesting to observe that such neutralization is not of importance for the nanofilled material at room temperature and at 40 °C. The differences in the simulated outcomes for LDPE with and without nanoparticles can be attributed to the strong distinctions in the amount of charge carriers generated in these materials. The obtained results also indicate that charge recombination cannot be underestimated in the charge transport model at elevated temperatures, even though its contribution is minor at room temperature.

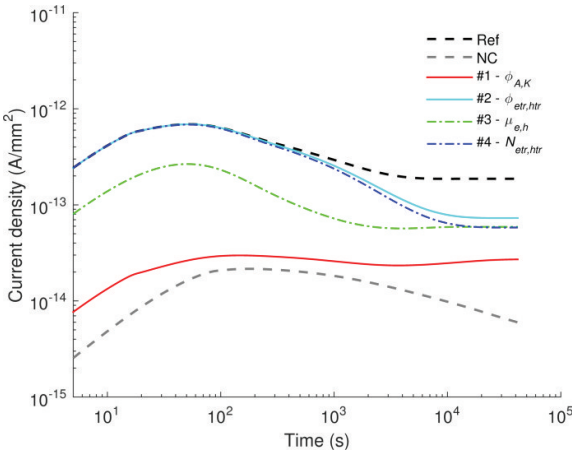

Figure 4.41. Simulated conduction currents at 40 °C obtained by varying model parameters. Four scenarios are considered as shown in Table 4.6. The parameters being changed are indicated in the legend.

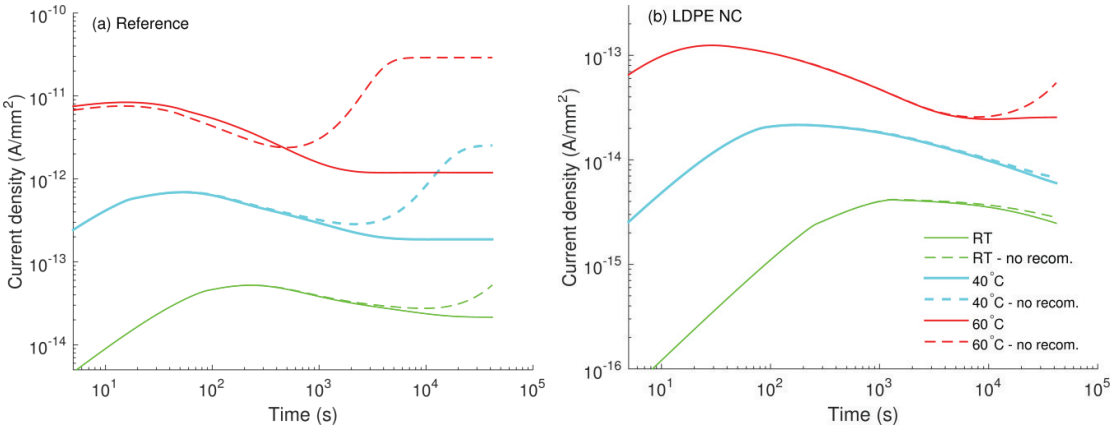

Figure 4.42. Simulated conduction currents obtained from models with (solid curves) and without (dashed curves) charge recombination.

4.4.3. Discussion

As mentioned above, broad maxima are observed in the simulated time variations of the current densities and the time t_p corresponding to the current peaks is temperature-dependent (see Figures 4.34 and 4.37). These localized peaks are not exhibited in our experimental results. Indeed, localized peaks are often detected in time-domain currents measured on oxidized LDPE [23] rather than on the non-oxidized counterpart [25]. Their appearance has been explained by the high concentration of carbonyl groups (–C=O) in the former material as compared to the latter. The carbonyl groups give rise to the hopping transport of mobile charge carriers in the bulk that eventually increases the conduction current [23]. Current maxima are therefore observed as a consequence of the build-up of a significant density of mobile charges in the bulk [123]. In contrast, lower conduction currents are detected for the non-oxidized PE and the peaks are most probably hidden by the displacement current. The latter arises in transient processes activated by the voltage application and is due to orientation of polar groups existing in PE. In LDPE samples used in this investigation, the presence of the antioxidant is anticipated to suppress the formation of carbonyl groups that explains the absence of the current maxima in the measured charging currents. Nevertheless, the current maxima in the simulated characteristics are of interest. According to the analysis by Many and Rakavy [123] for a single-carrier model in trap-free materials, the peak of the transient current corresponds to the arrival of charges at the counter electrode. The peak time t_p can be found as $t_p = 0.787 t_{tr}$, where $t_{tr} = L^2/(\mu V_0)$. Unlike the case of trap-free materials, different features are noted in the bipolar charge transport model for materials with traps. As charge trapping strongly reduces the density of mobile carriers, their total density and the current density achieve maxima well before the arrival of the dominating charge carriers at the counter electrode. Thus, in a correlation between t_p and t_{tr} established by using results obtained in sections 4.4.1 and 4.4.2.2, the multiplication factor should be much lower than 0.787.

Another noteworthy feature is that the accumulation of trapped charges in the unfilled LDPE at elevated temperatures becomes saturated after certain time, *e.g.* at 2×10^3 s at 60 °C. As the trapped charges constitute the main part of the space charges, the same tendency is observed for the latter, yielding an unchanged electric field distribution in the insulation bulk afterward. This eventually causes the steady state of simulated current density as seen in Figure 4.34. In order to avoid the early saturation in the simulated external current density, the trapping coefficients have been adjusted as increasing with temperature (see Table 4.5), which can be interpreted as the increased probability of charge trapping due to the presence of an increased amount of charges generated at higher temperatures. However, we realized that the steady state in the current density is persistent for simulations at elevated temperatures and it is unavoidable for the described model of charge transport. In fact, the saturation in the simulated trapped charges has been noted in [88] at 9×10^3 s and the saturated conduction currents are clearly illustrated in [71]. In both cases, the simulations of charge transport were implemented for the conditions of ambient temperature. Note that at room temperature, the steady state in the simulated characteristics is not exhibited within the considered time range in the present study; it only arises at elevated temperatures. The effect of temperature on the saturation of the simulated characteristics could be attributed to the fact that the injected currents described by Schottky's law, eqns. (3.1) and (3.2), may not fully reflect the physical

processes at the electrodes. According to Schottky's law, the amount of injected mobile carriers at the electrodes increases substantially with temperature and, hence, the traps in the insulation bulk can be filled more easily at higher temperatures, yielding the premature saturation in the density of trapped charges and so for the simulated conduction currents.

The applicability of Schottky's mechanism for charge injection at electrode–insulation interfaces is in fact questionable [84]. First of all, the distance x_{max} from the electrode corresponding to the maximum of potential barrier is too long so that an electron may be thermalized by collisions before reaching the barrier [84]. Secondly, the barrier height for injection used in simulations (~1.1–1.3 eV) is much smaller than that at metal–PE interfaces obtained by using DFT calculations, *e.g.* [124]. Taylor and Lewis [21] analyzed currents measured on thin films of PET and PE exposed to a wide range of applied electric field at various temperatures and proposed an alternative to Schottky's mechanism where a general form followed eqn. (4.17) instead of the coulombic form by eqn. (2.2) of the potential barrier at electrodes is utilized:

$$\Phi_G(x) = -\frac{Kq}{(ax)^n}, \tag{4.17}$$

$$\Phi_C(x) = -\frac{q^2}{16\pi\varepsilon x}. \tag{2.2}$$

In eqn. (4.17), K, a, and n are positive constants, K accounts for contributions of the charge q and material permittivity ε presented in the coulombic form (2.2), and x is the distance from the electrode in both equations. The widely used Schottky injection law with the coulombic form (2.2) of the potential barrier is a special case of the general form (4.17) when the exponent n equals unity. For PET and PE, it has been found that the constant n is much lower than unity. The departure from the image-law potential barrier according to eqn. (2.2) has been explained by space charge build-up at the interfaces and in the insulation bulk as well [21]. Additionally, zero-field activation energies derived for PET and PE were respectively 2.58 and 2.14 eV, which were interpreted as the potential barriers of the general law [21]. These values are closer to the results of DFT calculations obtained recently [124] as compared to the commonly used ones in the simulations. It should be mentioned that transient processes due to charge trapping, de-trapping, and recombination in the bulk have not been considered in these analyses [21] and, hence, the proposed approach should be reconsidered by taking into account the bulk processes. This may provide better explanation of experimental data obtained for the reference LDPE at elevated temperatures.

5. Charge transport and dielectric relaxation in enamel insulations

This chapter focuses on characterization of electrical properties of enamel insulations without and with chromium oxide filler. Electrical DC conductivity and dielectric permittivity were measured on the enamel insulations as well as on the filler in the form of powder. Contributions of different processes such as dipolar relaxation, interfacial polarization, hopping conduction, and DC conduction to the dielectric response of the considered enamels were analyzed. Study of charge transport in the multi-layered dielectrics was thereafter performed through measurements and simulation of the surface potential decay.

5.1. Results of DC conductivity measurements

5.1.1. DC conductivity of PAI flat samples

Measurements were conducted at room temperature and at low electric fields (~10^6 V/m). Charging currents measured on these materials reached their steady state after 4×10^4 s. The material volume conductivities were therefore calculated using the currents obtained at the end of this process as:

$$\sigma = \frac{IL}{US}, \tag{5.1}$$

where I is the measured current, U is the applied voltage, S is the area of the measuring electrode, and L is the insulation thickness. The calculated results are presented in Table 5.1, showing the increase in the conductivity due to the addition of chromium oxide. However, it was noticed that once the applied electric field was further enhanced, the shape of the charging currents changed drastically. Thus, for the Cr_2O_3-filled PAI resin, the time-dependent charging current was not reducing gradually as expected, but instead, several peaks were observed in the current trace. An analysis showed that these might not be attributed to the polarization process in the material and appeared, most probably, due to the imperfection of the material samples, *i.e.* their uneven thickness. It is noteworthy that an evenly distributed layer of PAI insulations on a metal substrate was hardly achieved during sample preparation. Since the measurements of volume conductivities on flat samples at high electric field were found to be unreliable, investigations were not conducted further.

5.1.2. DC conductivity of enameled wires' insulations

The tests on the insulation coating of enameled wires were conducted at numerous temperatures (room temperature RT ~22 °C, 40 °C, 60 °C, and 80 °C). A DC voltage of

Table 5.1. Volume conductivity of PAI and Cr_2O_3-filled PAI.

Material	Applied electric field, V/m	Volume conductivity, S/m
PAI	1.05×10^{6}	3.9×10^{-15}
Cr_2O_3-filled PAI	0.53×10^{6}	7.8×10^{-15}

100 V was applied, corresponding to the electric stress of ~10^6 V/m. Typical measured currents for both types of the enamels are shown in Figure 5.1. For the sake of clarity, only the results obtained at the lowest (22 °C) and highest temperatures (80 °C) are presented. One may observe that the measured currents decayed with time. They were practically independent of the material type and temperature within the first 50 s. This could be explained by the dominance of a displacement current component during the initial stage, governed by similar capacitances of the two types of samples. After ~10^3 s however, the measured currents were significantly different and the temperature effect was pronounced. Thus, the current increased by one order of magnitude as the temperature rose from 22 °C to 80 °C for both types of the insulations. To find conductivity values, the conduction current component has to be determined and it can only be achieved after a long measuring time when the displacement current component ceases. As can be seen in this particular case, the current decayed even after 10^5 s (~28h) and its purely conduction level was hardly achievable. Therefore, the measurements were stopped after 10^5 s for practical reasons and the conductivities were calculated from the corresponding current magnitudes.

As seen in Figure 5.2, the obtained volume DC conductivities for both the enamel insulations are in general lower than the values obtained with flat samples (Table 5.1) and obey Arrhenius relation:

$$\sigma(T) = \sigma_0 \exp\left(-\frac{W_c}{kT}\right), \tag{5.2}$$

where σ_0 is a constant parameter, W_c is the activation energy for the conduction. One may notice that the volume conductivity of the two materials is extremely low, but still higher for the filled enamel than for the conventional one. The calculated activation energies are 0.33 eV and 0.46 eV for the conventional and the filled enamels, respectively.

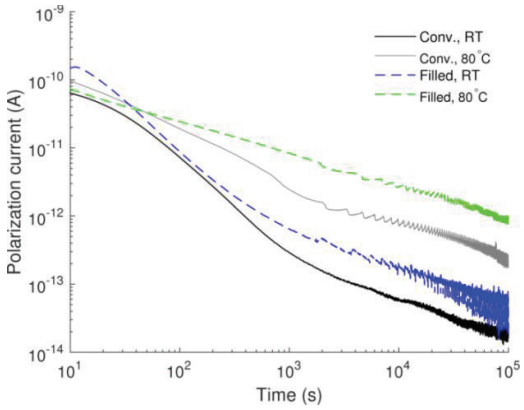

Figure 5.1. Time variations of polarization currents of the conventional and filled enamels at room temperature (RT) and 80 °C.

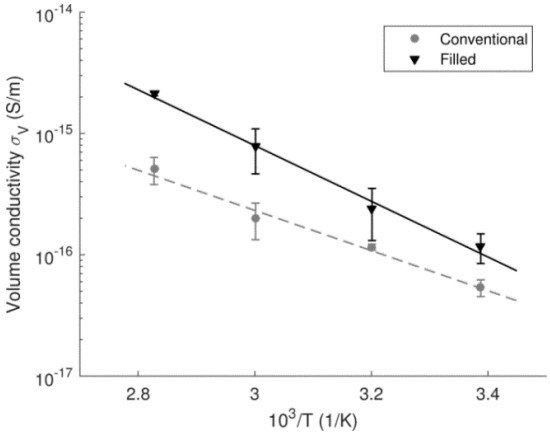

Figure 5.2. Temperature dependence of volume conductivity of the conventional and filled enamels. The conductivity has been calculated based on the current recorded at 10^5 s after test voltage application.

The conventional enamel coating used in this study can be considered as a series connection of three resistors corresponding to three layers in its structure. The volume conductivity of the conventional enamel measured at room temperature is around two orders of magnitude lower than that of Cr_2O_3-filled PAI. For the other two layers, the material conductivity is unknown, but one can expect PEI to be the most resistive, while modified aromatic PA as the most conductive among the three constituents of the considered enamel. Thus, the resistance of three resistors in series will be determined by that of the PEI base coat. In other words, the volume conductivity of PEI should be close to that of the conventional enamel (~6×10^{-17} S/m), while this parameter for PAI and aromatic PA is ~10^{-15} S/m.

The dependence of material DC conductivity on the applied electric field was studied by using different charging voltages (100, 300, and 800 V). Both polarization (charging) and depolarization (discharging) currents were recorded in these experiments and they are presented on Figure 5.3 for the filled enamel. As seen, the polarization and depolarization currents exhibit 'universal law' [125], *i.e.* they follow power-law time dependences with slopes close to –1. A slight change in the slopes can be observed at time t_K ~$(1–2)\times10^3$ s for both types of the measured characteristics. As the current shapes of each type (polarization/depolarization) remain unchanged with increasing applied voltage, the currents measured at higher voltages can be represented by the ones measured at lower voltages applying linear scaling and, therefore, the current can be represented as:

$$i(t)=\begin{cases} B_1 t^{-a_1} & t<t_K \\ B_2 t^{-a_2} & t>t_K \end{cases}. \tag{5.3}$$

Here, $B_{1,2}$ are constant values and $a_{1,2}$ are power factors. The dependencies of the quasi-steady state currents recorded at the end the measurements on the applied voltage are presented in Figure 5.4 for both materials using a log–log scale. As the slopes of the dependencies are close to 1, Ohmic conduction mechanism is most likely dominating in the range of the applied electric field (2×10^6–2×10^7 V/m).

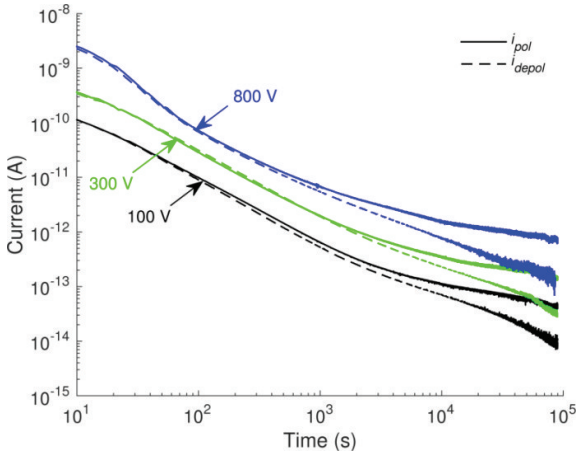

Figure 5.3. Polarization (solid curves) and depolarization (dashed curves) currents measured on the filled enamel at indicated applied voltages.

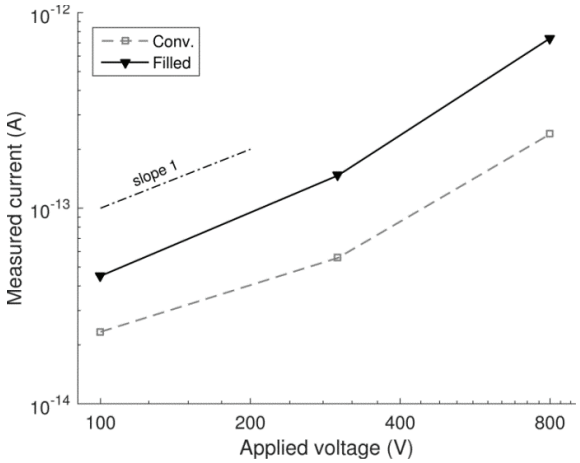

Figure 5.4. Log–log plot of *I–V* characteristics for both enamels.

Table 5.2. Volume conductivity of chromium oxide powder at room temperature.

E, V/m	0.71×10^{3}	1.43×10^{3}	2.86×10^{3}
σ, S/m	0.50×10^{-7}	1.00×10^{-7}	1.24×10^{-7}

5.1.3. DC conductivity of chromium oxide powder

The volume conductivity of chromium oxide powder measured at room temperature and at electric fields ~10^3 V/m is around eight orders of magnitude higher than that of the enamel insulations, as shown in Table 5.2. However, its impact on the conductivity of the filled enamel is limited, as exhibited in earlier studies. The reason is that the filler modifies the property of the PAI top layer only, whereas the resistive PEI base coat remains unchanged.

The electrical conductivity of chromium oxide has been reported in several studies performed for the material in different physical states, such as crystal grown from powder [79], thin film [80], powder [81] and porous specimens [82]. It is commonly emphasized that the exposure of the material to oxygen increases the average valence of surface chromium ions, giving rise to the density of positive charges. The accumulated charges might be reduced

at room temperature, yet they may still contribute to the conduction mechanism. As it is shown in [81], the conductivity of chromium oxide follows the Arrhenius dependence in the temperature range from 140 to 450 °C. Thus, an extrapolation using these data can be performed to obtain the electrical conductivity of chromium oxide at room temperature. This procedure provided a value 7.2×10^{-8} S/m that is in a good agreement with the measured results. This suggests the presence of space charges in the material in experiments of the present study.

5.2. Results of dielectric spectroscopy measurements

5.2.1. Experimental results

5.2.1.1. Complex permittivity of enameled wires' insulations

The measurements of complex permittivity on the insulation coating of enameled wires were conducted at different temperatures (room temperature RT ~24 °C, 40 °C, 60 °C, 80 °C, and 100 °C). Real and imaginary parts of the complex permittivity obtained in experiments are shown in Figures 5.5 and 5.6 for the conventional and filled enamels, respectively. As it is seen, at frequencies below 10 Hz, the imaginary part (dielectric loss) increased more rapidly with reducing frequency, whereas the real part showed a gradual rise in the whole frequency range. On the other hand, temperature affected those parameters differently: while the temperature rise reduced the real part at frequencies above 1 Hz, it considerably increased the imaginary part. It should be emphasized that coefficients of thermal expansion are low for both polymeric materials (less than 4×10^{-5} K^{-1} [126, 127]) and for copper conductor (~1.7×10^{-5} K^{-1} [128]), thus causing the thermal expansion less than 0.3% for the enamel layers and the wire conductor. Apparently, this could not account for the decrement of the real part of the complex permittivity, which was as high as 10% when the temperature increased from 24 to 100 °C. Localized maxima were observed in the loss curves of conventional enamel (Figure 5.5b). They shifted towards higher frequencies and became more considerable as temperature rose. However, such localized peaks were not observed in the loss curves for filled enamel (Figure 5.6b). In general, the magnitudes of the real and imaginary parts of the complex permittivity were higher for the filled enamel than for the conventional counterpart that can be attributed to the influence of highly dispersive and conductive chromium oxide filler.

5.2.1.2. Complex permittivity of chromium oxide powder

The real and imaginary parts of the complex permittivity of chromium oxide powder exhibited a rapid grow with reducing frequency (Figure 5.7). The slopes of the curves for both parameters are around –0.9 indicating the dominance of the low frequency dispersion process, which can be attributed to charge accumulation in the volume and its transport due to hopping between traps [125]. Aside from the low frequency dispersion, the temperature dependence of the complex permittivity of chromium oxide is noteworthy. Both the real and imaginary parts initially rose with temperature, reaching their maxima at around 60 °C, and then decreased again as the temperature continued growing up. This indicates the presence of a relaxation process with a loss peak at this temperature.

The relative permittivity of chromium oxide has also been measured in [83] for a single crystal of 6 mm in diameter and 0.5 mm in thickness. The experiment conducted at room temperature at frequencies of 1 kHz and 2 MHz yielded a practically constant value of 12–13. In spite of the fact that the test object and the electrical stress utilized in our measurements differ from those employed in [83], our measured result at frequency of 1 kHz is in line with that received in [83].

Although chromium oxide is relatively highly conductive and dispersive, its addition into the polymeric insulation does not enhance corresponding properties of the filled enamel drastically, proving that the percolation level is not reached. In particular, for statistically distributed spheres in 3D the theoretical percolation threshold would be ~15 vol% [129], which is larger than the percentage of the additive in the top coat of the filled enamel (8.7 vol%). Thus, molecular chains and amorphous state of PAI isolate micro-particles of chromium oxide one from another; thereby hindering an easy transfer of the space charges. In addition, chromium oxide fillers only modify dielectric properties of the top coat in the filled enamel. Consequently, the low frequency dispersion should be detected in the characteristics of the filled enamel, but it would not be as strong as that presented in the behavior of chromium oxide powder.

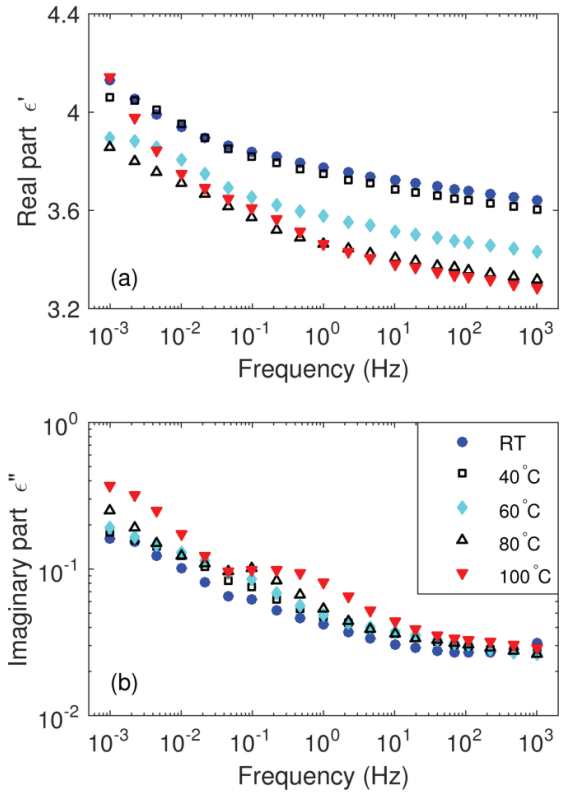

Figure 5.5. Real (a) and imaginary (b) parts of the complex permittivity of the conventional enamel at different temperatures.

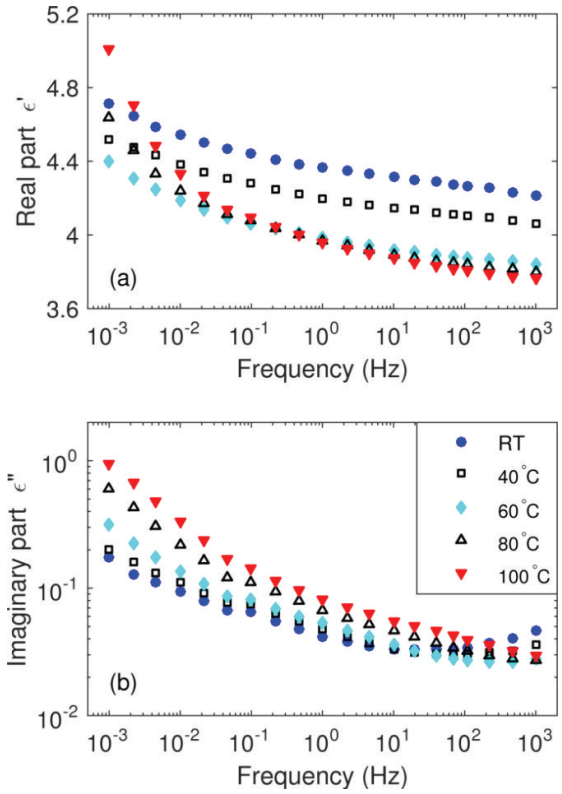

Figure 5.6. Real (a) and imaginary (b) parts of the complex permittivity of the filled enamel at different temperatures.

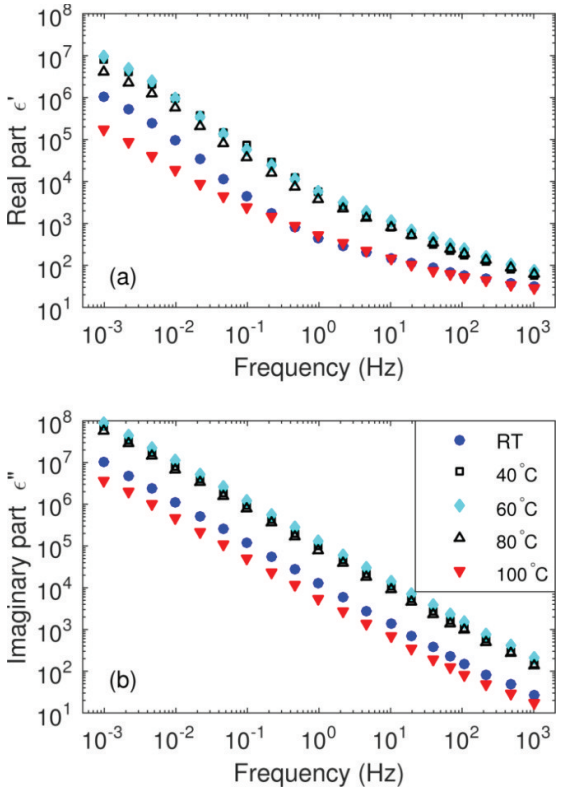

Figure 5.7. Real (a) and imaginary (b) parts of the complex permittivity of chromium oxide powder at different temperatures. Note that measured results at 40 °C, 60 °C and 80 °C are close.

5.2.2. Computer simulations of complex permittivity of the composite material

The influence of chromium oxide on dielectric properties of enamel insulation was studied using simulation tool COMSOL Multiphysics. A 3D model was created, representing the composite dielectric structure in Figure 3.4b. It consists of two layers corresponding to the base and the top coats, whose thickness is 25 and 15 μm, respectively. The top coat contained chromium oxide fillers of 8.7 vol%. Filler particles were considered as spheres of a diameter of 0.74 μm, regularly distributed in the base polymer. The size of the spheres was chosen as a statistical average based on the particle size distribution provided by the manufacturer. Since the dielectric properties of PAI and PEI differ slightly [77, 78], their characteristics could be ascribed to those measured on the conventional enamel. The measured complex permittivity of chromium oxide was also utilized for the simulations. All the input parameters for the model were taken from the experimental data obtained at room temperature (24 °C). The complex permittivity of the filled enamel was then calculated by the method proposed in [130].

The simulated and measured complex permittivities of the filled enamel are compared in Figure 5.8. A good agreement can be noticed in the losses, while a deviation ~7% is observed for the relative permittivity. The discrepancy may be attributed to the simplifications adopted in the simulations, *e.g.* considering fillers as spheres with the identical diameter as well as their regular distribution in the polymeric insulation. It is notable that the measured and simulated relative permittivities are close to the values corresponding to Wiener's lower

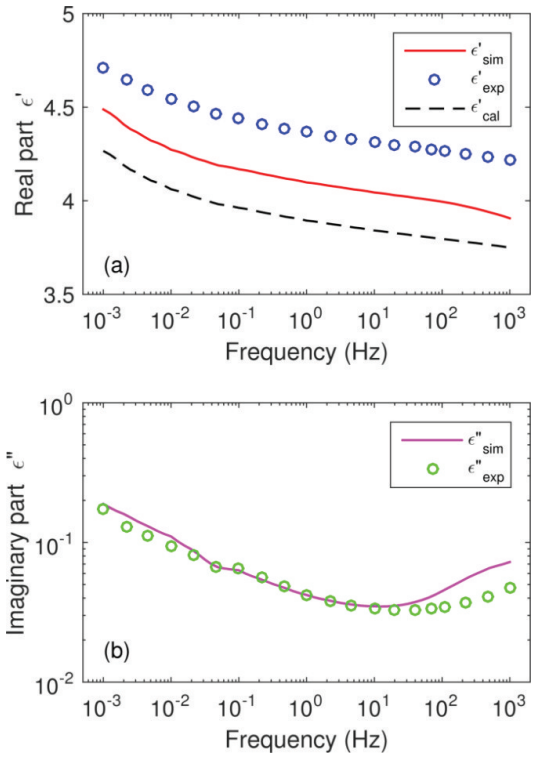

Figure 5.8. Simulated (solid line) and experimental (circles) complex permittivity of the filled enamel. Dashed line indicates the Wiener's lower bound of the relative permittivity of laminar mixtures.

bound [131]. This fact reflects the similarity in physical processes in the considered system and in composite dielectrics containing series connection of their components. However, a substantial difference is that the top layer of the enamel insulation is a composite material itself. Although the significance of interfaces between fillers and polymeric matrix becomes less noticeable when the size of filler particles increases [72], their role cannot be ignored in microcomposites. The simulation results showed that relatively high localized electric fields appear inside the material at interfaces perpendicular to electric field lines. Surface charges are also accumulated in these locations as the continuity of the ration of ε/σ is violated. Thus, the electrical stress is enhanced at the interfaces, while it is weakened in the remaining part of the dielectric. This suggests that if PDs occur on wire surfaces of twisted pairs of the filled enamel, they are likely to erode the stressed interfacial regions close to the surfaces rather than the polymeric material. In other words, PD performance of twisted pairs is governed by the behavior of interfacial regions and the filler. Additionally, highly conductive fillers may allow for rapid dissipation of charges that limit damaging effects of PDs [132]. In contrast, the electric field is quite homogeneously distributed in the conventional enamel and PDs might erode any locations on wire surfaces, which results in enhanced deterioration and thus to premature failure of the insulation. In summary, the alternation of electric field distribution in the filled insulation can be considered as the dominating factor contributing to the increase of its life time as reported in recent investigation [133].

5.2.3. Master curve of dielectric response

One can observe that for each of the materials, the shapes of the frequency-dependent complex permittivities resemble one another when the temperature increased. This is due to the fact that material properties do not change significantly in the studied temperature range which was far below the glass transition temperatures of base polymeric materials (which is ~270 °C [77, 78]). Hence, the data can be normalized for obtaining a master curve representation [134]. In terms of complex dielectric susceptibility χ^*, its frequency dependence at temperature T_1 can be achieved by shifting the corresponding characteristic at temperature T_2 laterally and vertically:

$$\chi^*(\omega : T_1) = k_a \cdot \chi^*(\Theta\omega : T_2). \tag{5.4}$$

Here, $\chi^*(\omega) = \varepsilon^*(\omega) - \varepsilon_{hf}$, $\varepsilon^*(\omega)$ is the complex dielectric permittivity as a function of the angular frequency ω, ε_{hf} is the dielectric permittivity at high frequencies, Θ is the factor of the lateral translation corresponding to the frequency shift, k_a is the factor of the vertical translation (the amplitude shift). Theoretically, the real part of the complex susceptibility at a particular frequency can be estimated by using the Kramers–Kronig relation. The obtained value is then subtracted from the real part of the measured complex permittivity at the same frequency for gaining the permittivity at high frequencies. However, the data measured in the present study (performed within six decades of frequency) do not allow for calculating ε_{hf} by this procedure. Therefore, the master curve was achieved for the complex permittivity rather than for the complex susceptibility. For this, the susceptibility (5.4) was split into the real and imaginary parts:

$$\chi'(\omega:T_1) = k_a \cdot \chi'(\Theta\omega:T_2), \tag{5.5}$$

$$\chi''(\omega:T_1) = k_a \cdot \chi''(\Theta\omega:T_2), \tag{5.6}$$

which can be further represented as:

$$\varepsilon'(\omega:T_1) - \varepsilon_{hf1} = k_a \cdot \left[\varepsilon'(\Theta\omega:T_2) - \varepsilon_{hf2}\right], \tag{5.7}$$

$$\varepsilon''(\omega:T_1) = k_a \cdot \varepsilon''(\Theta\omega:T_2). \tag{5.8}$$

Here, ε_{hf1} and ε_{hf2} are the high frequency permittivities at temperatures T_1 and T_2, respectively. Equation (5.7) can be rewritten:

$$\varepsilon'(\omega:T_1) = k_a \cdot \varepsilon'(\Theta\omega:T_2) + \left[\varepsilon_{hf1} - k_a \cdot \varepsilon_{hf2}\right]. \tag{5.9}$$

The normalization procedure was initially conducted for the loss part. It should be noted that the contribution of DC loss $\sigma_{DC}/\omega\varepsilon_0$ (ε_0 is the vacuum permittivity) in the measured dielectric loss $\varepsilon''(\omega)$ is insignificant (less than 6%). Therefore, the subtraction of the DC loss from the measured total loss before normalization, as described in [125], can be ignored as this introduces just a minor error. The same translation factors used for normalizing the loss were subsequently utilized for normalizing the real part of the complex permittivity. This resulted in a small discrepancy between the curves of the relative permittivities at different temperatures, which is due to the second component on the right hand side of eqn. (5.9). Since this component is independent on frequency, a vertical shift is to be introduced to compensate the influence of the permittivities at high frequencies.

The obtained master curves for the reference temperature of 24 °C are shown in Figure 5.9. The frequency shift Θ of the response can be described as a function of temperature [135]:

$$\Theta(T) = \Theta_0 \exp\left(-\frac{W_p}{kT}\right), \tag{5.10}$$

where Θ_0 is a constant parameter, W_p is the activation energy for polarization, which is 0.60 and 0.63 eV for the conventional and filled enamels, respectively.

The contribution of different processes (dielectric relaxation, DC conduction, low frequency dispersion) to the dielectric properties of the materials can be identified by analyzing the curves. One can observe that for both materials, the studied frequency range can be divided into three intervals limited by characteristic frequencies, at which the behaviors of the curves change. The first characteristic frequencies (f_1) are ~10^{-4} Hz and ~3×10^{-4} Hz for the conventional and filled enamels, respectively, while the second ones (f_2) are ~70 Hz for both materials. Three intervals are marked in Figure 5.9 by vertical lines. In the first interval, the slopes of the loss curves are respectively –0.34 and –0.47 for the conventional and the

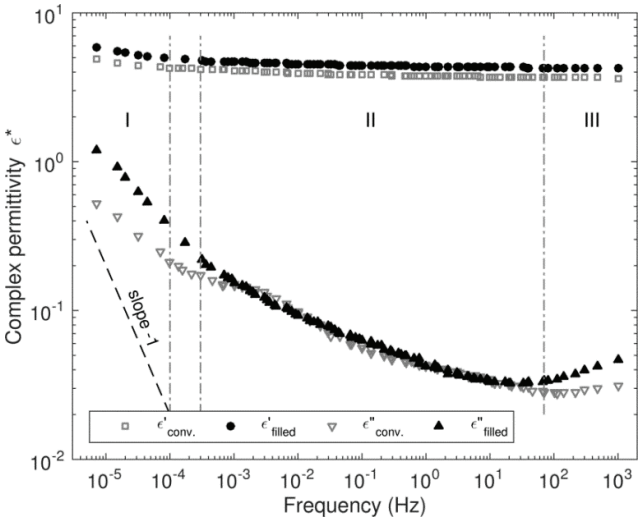

Figure 5.9. Master curves of complex permittivity for both enamels at the reference temperature of 24 °C. A line with slope of –1 is introduced for comparison with the slopes of the dielectric loss curves at low frequencies.

filled enamels, whereas the slopes of the relative permittivity curves are less than –0.08. Hence, as the slopes of the loss curves are far from –1, DC conduction is not the prevalent process in the considered frequency interval [125]. In addition, as the slopes are different for the real and the imaginary parts of the complex permittivities, low frequency dispersion is also not the sole process in both studied materials [125]. This suggests that a dielectric relaxation process with a loss peak at some frequency below f_1 should be present in both enamels, which is superimposed on the above-mentioned processes. In the second interval, a localized loss peak apparent at frequency of ~10^{-3} Hz in the characteristics of the conventional enamel may be attributed to the existence of a relaxation process. At the same time, the loss curve of the filled enamel shows a power-law behavior (with the slope –0.2) without a loss peak that could be owing to the change in the properties of enamel insulation brought about by chromium oxide fillers. In the third interval, an increase in the imaginary part is observed for both materials. This possibly implies the existence of yet another relaxation process with a loss peak at frequencies outside our experimental window. A detailed analysis on the origin as well as the contributions of different relaxation processes is discussed in the following section.

5.2.4. Modeling dielectric susceptibility of enamels

The dielectric susceptibility can be modeled by considering the contributions of dielectric relaxation, DC conduction, and low frequency dispersion [135]. By assuming that three polarization relaxation processes take place in the studied materials, the complex dielectric susceptibility as a function of the angular frequency can be expressed as:

$$\chi^*(\omega) = \sum_{n=1}^{3} \frac{\chi_{sn}}{\left(1+(i\omega\tau_n)^{\alpha_n}\right)^{\beta_n}} + \frac{\sigma_{DC}}{i\varepsilon_0\omega} + \frac{\varsigma}{\varepsilon_0 (i\omega)^{\gamma}}. \tag{5.11}$$

Here, the dielectric relaxation (the first term) is described by the Havriliak–Negami expression, the index n represents relaxation processes (n = 1, 2, 3), χ_{sn} is the dielectric susceptibility at ω = 0 Hz, τ_n is the relaxation time, σ_{DC} is the DC conductivity, α_n, β_n, ς, γ are constant parameters, $0 < \alpha_n, \beta_n, \gamma \leq 1$. The DC conductivity obtained in section 5.1 was used as an input parameter of the model. The obtained master curves were fitted using a nonlinear least-square method, which is achieved by minimizing the relative error θ between the experimental (index *exp*) and modeled (m) values of the real and imaginary parts of the complex susceptibilities:

$$\theta = \sum \left[\left(\frac{\chi'_{\exp} - \chi'_m}{\chi'_{\exp}} \right)^2 + \left(\frac{\chi''_{\exp} - \chi''_m}{\chi''_{\exp}} \right)^2 \right]. \tag{5.12}$$

The results of the fitting are shown in Figures 5.10 and 5.11 for the conventional and filled enamels, respectively. As seen, the low frequency dispersion (hopping conduction) and the third relaxation process appear to be the main contributors to the real part of the dielectric susceptibility for both materials at low and high frequencies, respectively. On the other hand, three polarization relaxation processes and the low frequency dispersion contribute mostly to the imaginary part of the dielectric susceptibility.

The behavior of the first relaxation process is similar in both enamels, yielding peak frequencies ~10^{-5} Hz that allows for suggesting their identical origin. By considering the multi-layered structures of the two insulation systems (see Figure 3.4), one may suggest that this relaxation process is most likely caused by MWS polarization between the PAI and the PEI layers. The loss peak frequencies of the interfacial polarization can be calculated by using dielectric properties of two polymers reported in [77, 78] as well as electrical conductivity measured in this study. The calculated results are ~10^{-5} Hz, which are close to the values gained by the fitting, approving our assumption.

The second relaxation process is obviously different in the two enamels. The relaxation process arising in the conventional enamel is characterized by a broader response (α = 0.81, β = 1) than the Debye relaxation with the loss peak frequency of 2×10^{-3} Hz. It could be associated with the interfacial polarization between the PAI over coat and the aromatic PA bonding coat. Note however, that available data on the electrical conductivity of aromatic PA, PAI, PEI used in enamel insulation are limited and it is assumed that aromatic PA is more conductive than PAI and PEI. This leads to a shift of the loss peak due to MWS polarization between PAI and PA layers to higher frequencies as compared to that of the MWS polarization between PAI and PEI layers. In the filled enamel, the second relaxation process (α = 0.30, β = 1) is much broader than that corresponding to Debye relaxation, which yields the dielectric response without a localized peak. It could be due to the introduction of chromium oxide fillers into the PAI matrix. As their dielectric properties are clearly distinct, charges accumulate in their interfacial regions resulting in a MWS polarization. The highly conductive property of the additives, as shown in the section 5.1, leads to a higher frequency of the loss peak. It should be noticed that the accumulated charges may be trapped in localized states inside the insulation and transferred by hopping between them, thus giving rise to the

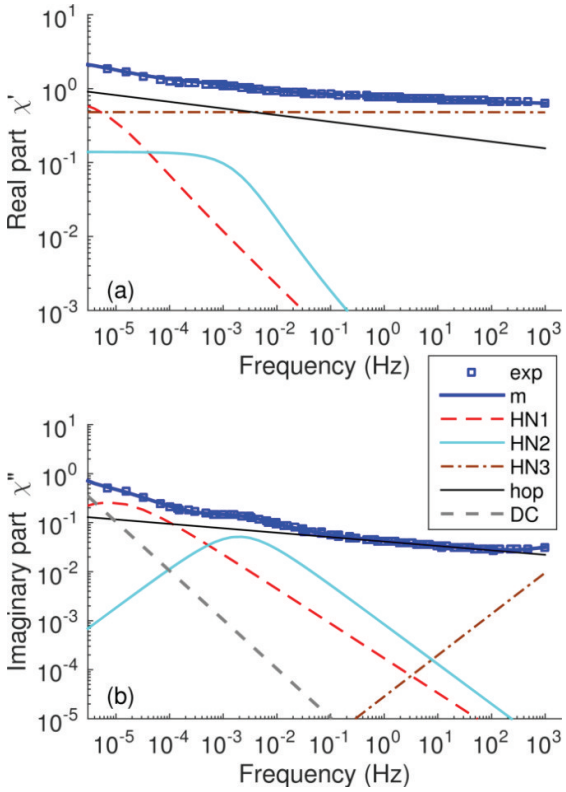

Figure 5.10. Real (a) and imaginary (b) parts of the complex susceptibility of the conventional enamel. The labels *exp*, *m*, *HN*, *hop*, *DC* represent the measured, modeled, Havriliak–Negami, hopping conduction, and DC conduction contributions, respectively.

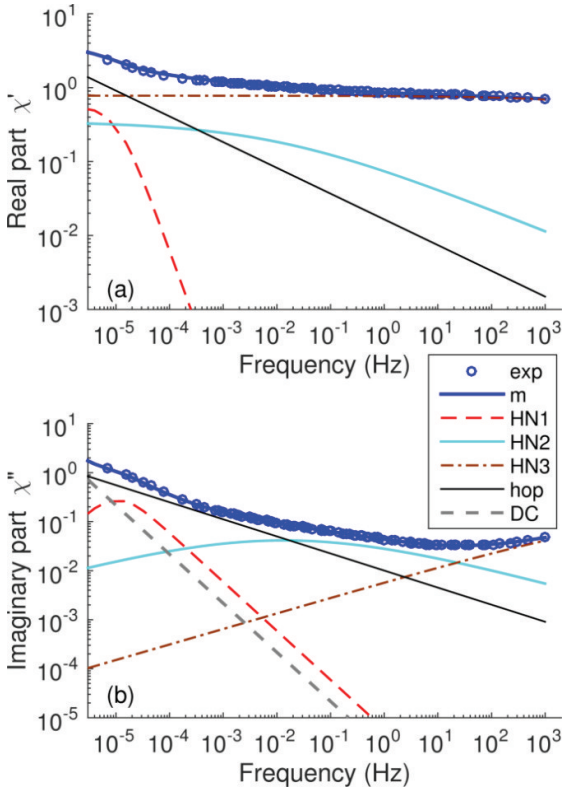

Figure 5.11. Real (a) and imaginary (b) parts of the complex susceptibility of the filled enamel.

hopping conduction in the filled enamel [125]. Accordingly, the hopping conduction is the strongest component at frequencies between 10^{-5} and 10^{-2} Hz for the filled enamel, but it is not the case for the conventional enamel. Besides, as the interfaces in the investigated systems are shortly apart, the interaction of charges accumulated due to MWS polarizations affects both of the relaxation processes.

Further, the third relaxation process in both materials dominates at high frequencies and provides the loss peak at frequency ~10^5 Hz, which is possibly owing to the dipolar relaxation in polymeric materials. Besides, the contribution of the DC loss in the measured dielectric loss becomes considerable only at frequencies as low as 10^{-5} Hz.

In summary, the complex dielectric permittivity of the conventional enamel seems to be determined by the dipolar relaxation at high frequencies and MWS polarizations at the two interfaces in its multi-layered structure at lower frequencies. The addition of chromium oxide fillers to enamel insulation gives rise to hopping conduction and MWS polarization at interfaces between the fillers and the base polymeric material. In addition, three relaxation processes present in the investigated enamel might have different activation energies, yet their value should be close to the results calculated in section 5.2.3. Otherwise, largely diffused master curves may be achieved [125]. Investigations should be further conducted to obtain more experimental evidences of relaxation processes in the insulation coating of the enameled wires.

5.3. Results of surface potential decay measurements

This section presents experimental data of potential decay on surfaces of enameled wires' insulations. The experiments were mainly conducted on multi-layered insulations, while some tests were carried out on the single-layered samples for comparison. The potential decay mechanisms were then discussed in details and charge mobilities were derived from measured outcomes.

5.3.1. Experimental results

5.3.1.1. Potential decay on multi-layered insulations of enameled wires

Initial surface potential distribution

As will be revealed in the following section that the potential distribution on sample surface is symmetrical about the sample center and thus it is sufficient to be represented by the potential profiles in the direction along the wires and across the center. The surface potential profiles obtained at three minutes after charging are shown in Figure 5.12 for the filled enamel exposed to corona at different charging voltages. As seen, the maximum of the potential is located right beneath the charging needle (surface center). Increasing charging voltage gives rise to the radius of surface charged spot and the maximum value for the potential, indicating more charges deposited. A polarity effect is also notable in the characteristics. For example, the lowest charging level for negative polarity at –3 kV yielded a charged spot of 15 mm in radius and a maximum potential of –1.5 kV. Meanwhile, the charging conducted at the same voltage magnitude for positive polarity did not result in

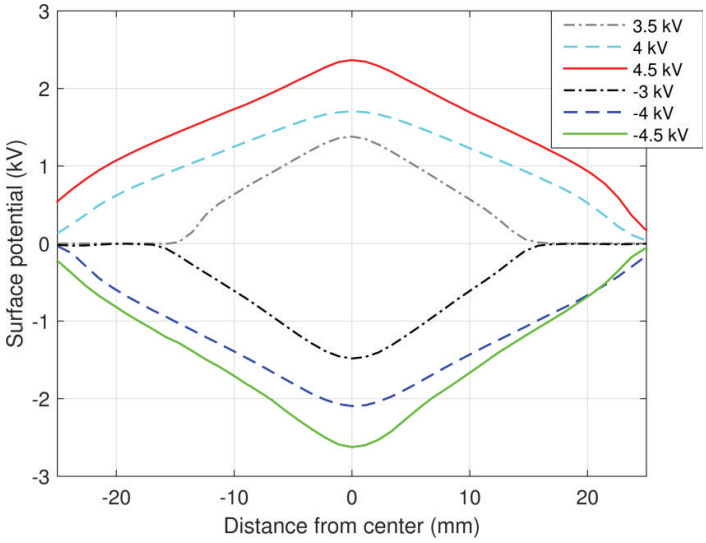

Figure 5.12. Surface potential distribution obtained at three minutes after charging for the filled enamel. The charging needle was positioned at the center. The charging voltages are indicated in the legend.

charge deposition at all that might be due to a low field at the needle tip which was not sufficient to initiate corona discharge. Only by increasing the charging level up to +3.5 kV, a similar amount of surface charges was achieved as for the charging voltage of –3 kV. In addition, at the other two charging voltages (4 and 4.5 kV), the maximum surface potential obtained was higher in case of negative polarity than for positive polarity. This can be attributed to the known fact that corona discharges in a needle–plane configuration are stronger at negative polarity as compared to those at positive polarity [136].

Potential decay on winding samples

Figure 5.13 illustrates the surface potential decay for the filled enamel at the charging voltage of –4 kV in two directions (along enameled wires and perpendicular to them). The difference in sample geometry in the two directions suggests that surface charge leakage is more likely to appear along wires rather than in direction perpendicular to them (the turns of the wires in the sample are separated by small air gaps). However, as can be seen from the figure, similar shapes of surface potential distribution are observed for the two directions and lateral spreading of surface potential is not found, implying a weak charge transport along insulation surface. In other words, the surface charge leakage did not play an important role in charge decay. Apart from the surface leakage, surface charges could decay through bulk transport and charge neutralization by gas ions available in air volume nearby [107]. Taking into account that the experiments were conducted in such a way that zero field was maintained between the probe and the charged surface, negligible gas neutralization can be assumed for the surface part underneath the probe (note that the radius of the probe body was ~11.2 mm). Consequently, bulk neutralization can be suggested as a main process causing surface charge decay. Note also that surface potential decayed faster at the sample center (where the potential was higher) than at its edges that indicates a field-dependent decay behavior. Finally, the surface potential distributions were similar for both investigated

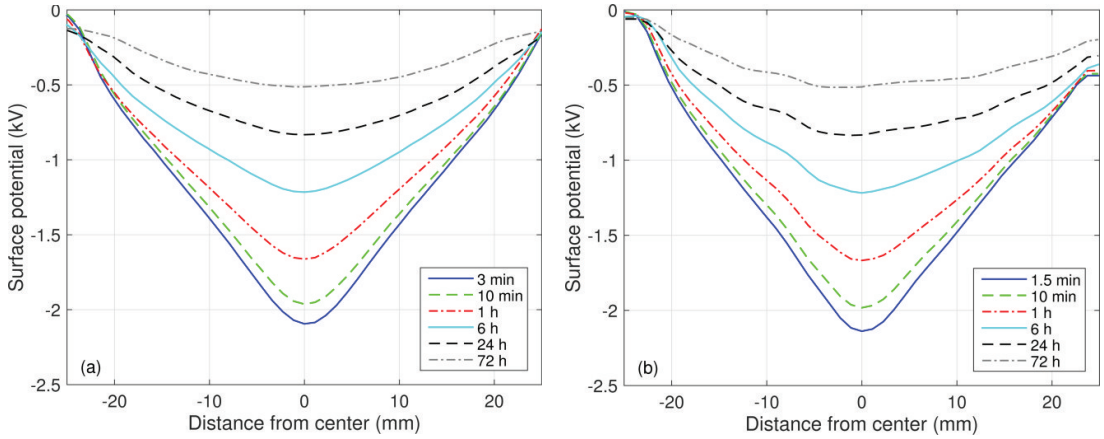

Figure 5.13. Surface potential distribution for the filled enamel charged by negative corona (–4 kV) in two directions across the surface center: (a) along wires and (b) perpendicular to wires.

enamels and, therefore, the results for the conventional enamel are not presented, but all the above remarks are also applicable.

Potential decay at sample center

Results on potential decay at the surface center of the filled enamel are shown in Figure 5.14 for different charging voltages. The initial magnitudes of surface potentials were recorded at ~(10–15) s after charging. As seen, the decay process was accelerated as the charging voltage increased, showing the dependence of decay rate on the surface potential magnitude. In addition, the decay characteristics were similar for both polarities of the charging voltage, indicating the independence of the decay process on the polarity of the deposited ionic charges. The potential decay characteristics are compared for both insulating materials in Figure 5.15. As the initial measured surface potentials were strongly diverged, the data were normalized by dividing the measured to the initial values. The potential decay process was obviously faster for the filled enamel than for the conventional one. For example, the decay of surface potentials to 60% of its initial level required ~(1.5–4)×10^4 s for the filled enamel, while the identical decay required approximately ten times longer duration for the conventional enamel.

The dependence of the decay rate on the surface potential magnitude is illustrated in Figure 5.16 for the charging voltage of 4.5 kV. As seen, the rates obtained for the filled and conventional enamels are quite similar at the beginning of the decay process (highest potential values). The difference increases with time (reduction of the potentials) and reaches around one order of magnitude at lower surface potentials. The observed difference can be elucidated by the enhanced volume conductivity of the filled enamel (section 5.1.2). From the figure, it is evident that for both materials the decay rate exponentially reduced with decreasing surface potential (the experimental data can be fitted by a straight line in the semi-logarithmic scale used).

On the other hand, the decay rate was also time-dependent. Figure 5.17 presents the decay rate of normalized surface potential $-\mathrm{d}V/V_0\mathrm{d}t$ as a function of time in a log–log plot for the filled enamel charged by positive corona. An important feature observed in this plot is that the

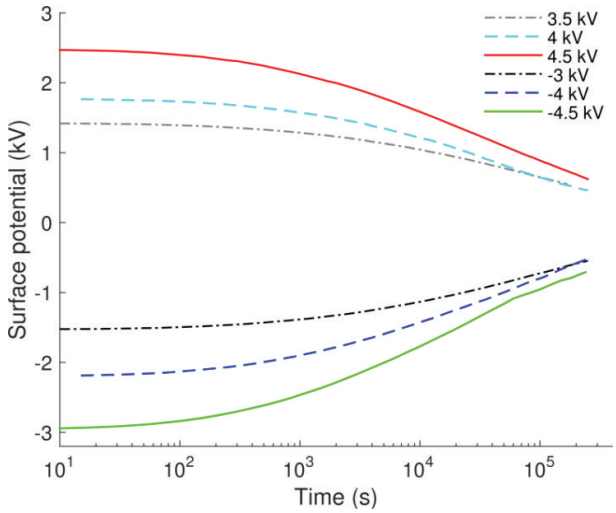

Figure 5.14. Potential decay at sample surface centers for the filled enamel. Charging voltages are indicated in the legend.

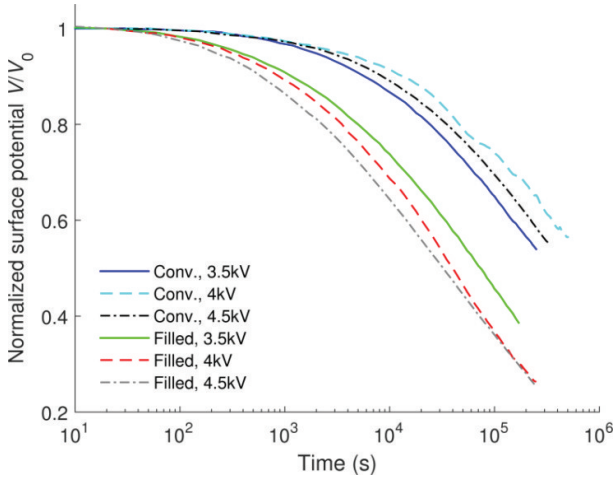

Figure 5.15. Decay characteristics of the normalized surface potential. Charging voltages and materials are indicated in the legend.

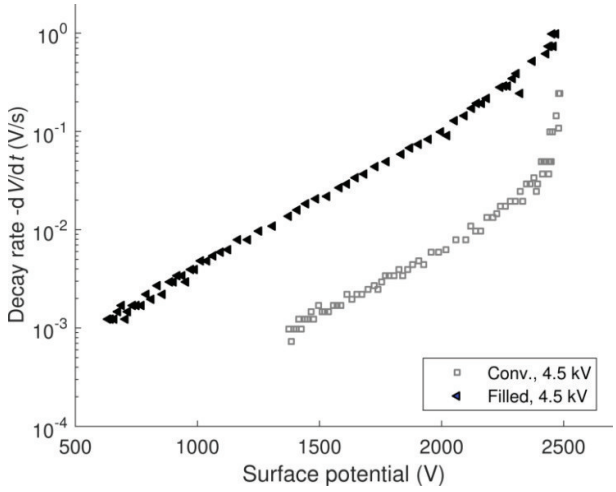

Figure 5.16. Decay rates of surface potentials at surface centers for charging level of 4.5 kV.

decay rate $-\mathrm{d}V/V_0\mathrm{d}t$ can be fitted by two straight lines with different slopes close to –1, thereby it can be described by the power-law time dependence:

$$-\frac{\mathrm{d}V(t)}{V_0\mathrm{d}t}=\begin{cases}M_1 t^{-(1-\eta_1)} & t<t_T\\ M_2 t^{-(1+\eta_2)} & t>t_T\end{cases}. \tag{5.13}$$

Here, M_j (j = 1, 2) stands for constant values, η_j indicates power factors, t_T denotes the characteristic time corresponding to the knee point of the curve. The factors $\eta_{1,2}$ obtained at different initial potentials are provided in Figure 5.18a. As seen, parameters $\eta_{1,2}$ vary within narrow intervals and their weak dependences on the field strength are illustrated by the fitting curves. This observation is analogous to that reported in [34] for SPD on thin films of HDPE. In this study, the characteristic times t_T varied between 10^3 and 2×10^3 s, while its field-dependent behaviour was not noticed.

For the conventional enamel, the decay rate of the normalized surface potential also obeyed the power-law dependence. The factors η_j obtained by curve fitting are presented in Figure 5.18b. Field dependence of the power factors η_j is more difficult to derive for the conventional than for the filled enamel. Furthermore, the characteristic time t_T varies between 3×10^3 and 10^4 s, which is several times larger than that for the filled material.

For each material, the fact that the variations of the power factors η_j take place within narrow ranges suggests that the decay rate of the normalized surface potential tends to be a unique function of time, irrespectively of the initial surface potential V_0 and the polarity of the charging voltage. Thus, the decay rate may be related to the polarization displacement current as suggested by the model based on dipolar polarization [137]. Besides, the power-law time dependence of the decay rate indicates that charge injection may contribute to the decay process [34, 138, 139]. Accordingly, the results of surface potentials obtained in this experimental study are examined further (section 5.3.2) utilizing corresponding models.

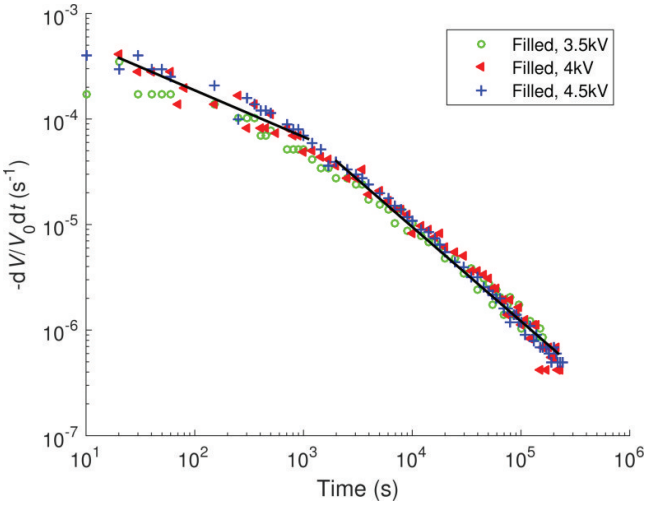

Figure 5.17. Decay rates of the normalized surface potential on the filled enamel. Applied voltages for corona charging are indicated in the legend.

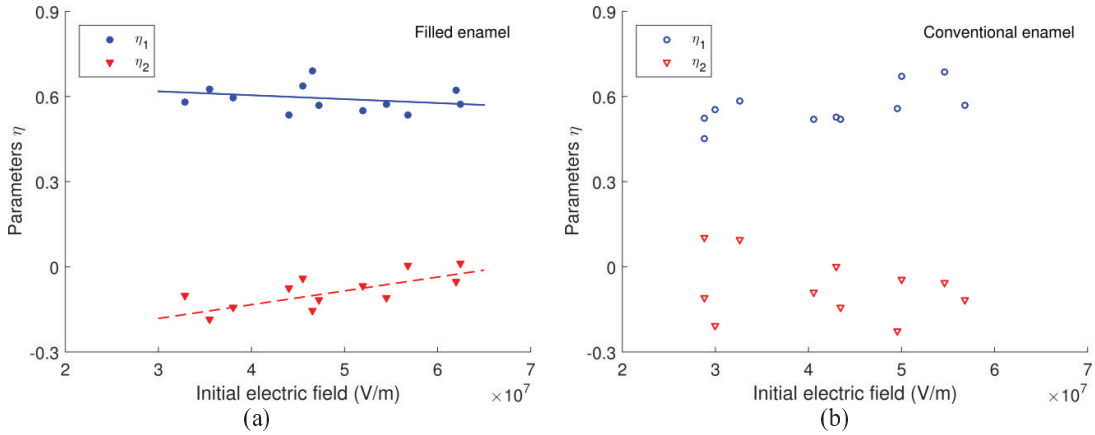

Figure 5.18. Decay parameters η_j as functions of the initial electric field for (a) the filled enamel and (b) the conventional enamel.

5.3.1.2. Potential decay on single-layered PAI insulations

Potential decay was also measured on single-layered PAI insulation with and without Cr_2O_3 microfillers. In these experiments, the flat specimens employed earlier for the DC conductivity measurements were used. Surface charging was conducted by positive corona at +4 kV and surface potential monitoring was performed according to the procedure described in section 3.2.3.2.

Decay of surface potential on the single-layered insulations is presented in Figure 5.19, where results are normalized to the potential magnitude recorded at 15 s after charging. As can be seen, a majority of surface charges/potential on both materials decayed within 2×10^3 s. The decay was faster for the Cr_2O_3-filled PAI than for PAI at the beginning of the process, but it became similar for both materials at low surface potentials. One may notice the significant difference in the magnitude of the surface potentials initially measured on Cr_2O_3-filled and unfilled PAI layers. This can be attributed to the contrasts in material dielectric properties and sample thicknesses. As it is discussed in [140], the density of surface charges Q_s on windings of enameled wires can be estimated by eqn. (5.14), which is commonly applied for the case of homogeneous surface potential distribution on a flat sample of an identical insulation thickness L:

$$Q_s = \frac{\varepsilon_0 \varepsilon_r}{L} V . \tag{5.14}$$

This estimation is validated by assuming insignificant charge injection into the bulk during charging process. By calculating surface charge densities corresponding to the surface potentials recorded at 4 s after charging, it was found that the charge density on the Cr_2O_3-filled PAI insulation is just ~9% lower than that on the PAI layer. The lower surface charge density on the Cr_2O_3-filled PAI can be attributed to the faster decay of surface charges on this material as compared to that on the unfilled PAI.

5.3.1.3. Comparison of potential decay on single- and multi-layered enamel insulations

Potential decay on the filled enamel with a double-layered structure is also shown in Figure 5.19 for comparison. The potential decay process was far faster for the single-layered samples than for the filled enamel. For instance, the potential decayed to 50% of its initial value required less than 300 s for both samples of the formers, while it appeared at ~3×10^4 s for the latter (100 times slower). Recall that the studied filled enamel consists of a PEI base coat (~25 µm thick) and a Cr_2O_3-filled PAI top coat (~15 µm). Flat samples of PEI were not available for conducting SPD measurements, but the decay characteristics on the material may be linked to its electrical volume conductivity, which is by two orders of magnitude lower than that of PAI in accordance to our evaluation (section 5.1). Therefore, the time to half of the initial potential is expected to be longer than 300 s, but it is presumably less than the corresponding time for the filled enamel. On the other hand, the time to half of the initial potential might be close to that for the Cr_2O_3-filled PAI flat sample and the material of the top coat of the filled enamel, even though the filler content of the former (4.3 vol%) is two times lower as compared to the latter (8.7 vol%). In summary, the potential decay is prolonged for the filled enamel as compared to that of its constituents, which may only be explained by the contribution of the interface between two layers to the decay process.

5.3.2. Potential decay mechanisms

The decay of charges deposited on insulation surface was measured in an open circuit configuration by means of a non-contact technique utilizing Kelvin's electrostatic probe [102]. As the contribution of the surface charge leakage and the gas neutralization in the decay process is insignificant for the studied material samples, the decay of surface potentials can be considered mainly through bulk processes and, thus, can be analyzed based on a current continuity equation [108]:

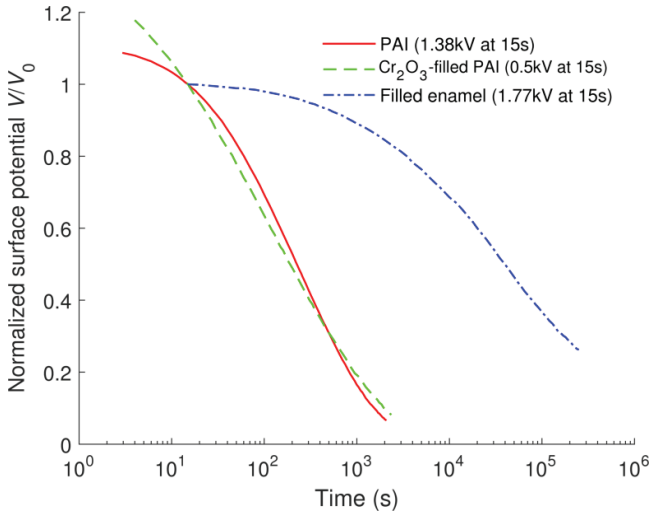

Figure 5.19. Potential decay on sample surface of PAI and Cr_2O_3-filled PAI single-layers and on the filled enamel. Results are normalized to the potential recorded at 15 s after charging.

$$\frac{\partial D}{\partial t} + \sigma E + \sum_j \mu_j \rho_j E = 0 . \tag{5.15}$$

The first term represents the contribution due to polarization of the material exposed to the electric field E induced by deposited charges, where D stands for the displacement field. The second term is related to the intrinsic conduction of material due to the field E. The third term takes into account the dynamics of charges injected into insulation, where μ_j and ρ_j are the charge mobility and density, respectively. The contribution of each mechanism on the total decay of surface charges depends on several factors such as dielectric properties of materials as well as the magnitude of the electric field in the bulk.

In order to understand the physical mechanisms of surface charge decay, numerous models have been proposed. A comprehensive review of SPD models can be found in [108, 141]. In this section, models based for intrinsic conduction, dipolar polarization, and charge injection are briefly outlined and are further utilized for examining SPD measured characteristics.

5.3.2.1. Potential decay due to intrinsic conduction

The dominance of the intrinsic conduction is found in case when polarization becomes stabilized and the effect of injected charges is insignificant. For this, the material is characterized by a constant relative permittivity ε_r and the third component in the continuity equation (5.15) can be ignored. Consequently, apparent bulk conductivity can be derived as

$$\sigma(V) = -\frac{\varepsilon_0 \varepsilon_r}{V(t)} \frac{\mathrm{d}V(t)}{\mathrm{d}t}, \tag{5.16}$$

where $V(t)$ is the surface potential as a function of time. Note that eqn. (5.16) is obtained assuming an uniform field $E(t) = V(t)/L$ in the material bulk induced by uniformly distributed surface charges.

The model has been utilized for characterizing electrical properties of several polymers, such as ethylene-propylene-diene-monomer (EPDM) based rubber and silicon rubbers with sample thicknesses in mm range [142]. The obtained in these cases apparent volume conductivities exhibited field-dependent behavior and could be therefore described in terms of Poole–Frenkel model as a function of $\sqrt{E}$:

$$\sigma = \sigma_0 \exp\left(\beta_{PF} \sqrt{E} / 2kT\right), \tag{2.8b}$$

where σ_0 is a constant parameter and the theoretical Poole–Frenkel coefficient β_{PF} is expressed as:

$$\beta_{PF} = \sqrt{q^3 / \pi\varepsilon} . \tag{2.9b}$$

In other works [74, 143], results of SPD measurements have been elucidated by a model including the contribution of intrinsic conduction. By fitting experimental results, the intrinsic

conductivities of materials like epoxy resin, polytetrafluoroethylene (PTFE), and alumina have been determined and, thus, SPD measurements were considered as an alternative method for evaluating their electrical conductivity.

The apparent volume conductivities of both enamels have been derived from SPD measurements (Figure 5.20), showing a field-dependent behavior. The obtained conductivity was higher for the filled enamel than for the conventional one, which is associated with the higher decay rates for the former material. This result is apparently caused by the addition of highly conductive chromium oxide particles into the top coat of the filled enamel. As the slopes of the volume conductivity curves changed, the obtained characteristics can be separated into two regions, as exhibited in the figure. By assuming the Poole–Frenkel model, one can deduce the material relative permittivities from the slopes of the dependencies. The calculated permittivities of both enamels are provided in Table 5.3, which are strongly differed from experimental results obtained in section 5.2.1. This suggests that Poole–Frenkel model is unlikely the governing conduction mechanism in the considered materials.

To illustrate the effect of the initial electric field on material properties, we present in a single plot data of the material bulk conductivity obtained from experiments at different charging levels (Figure 5.21). Provided that the decay process is mainly governed by intrinsic conduction, the derived conductivity should be the intrinsic material property that solely depends on the applied electric field. In other words, a single value of the conductivity should be obtained for a given surface potential (or an electric field), independently of the data used for calculations. Consequently, the curves of the apparent bulk conductivity derived from SPD at different charging voltage magnitudes must overlap each other. As can be observed in Figure 5.21, it is not the case for the present study, where deviations are significant at the initial stage of the measurement (associated with high surface potentials).

Material volume conductivity measured by standard method in section 5.1.2 is also provided in the figure for comparison. As the power factor of the field dependence is close to 1, the material conductivity can be considered as the intrinsic property. An extrapolation of these data to higher applied voltages (typical for the SPD measurement) assuming a similar slope of the field dependence yields magnitudes lower than the apparent bulk conductivity attained from SPD. Hence, the deduced apparent bulk conductivity must comprise other terms rather than only the intrinsic conductivity.

Discrepancies between the magnitudes of the apparent volume conductivity of the studied materials can also be found if surface potentials measured at different locations on sample surface are utilized for the calculation. Thus, the results shown in Figure 5.22 present the bulk conductivity obtained for three different locations apart from the sample center. As seen, the deviation from the data corresponding to the surface center increases with increasing distance from it. One may argue that as the Kelvin probe was not located above peripheral locations, the zero-field was not maintained in the surrounding gas volume, causing intensified surface charge neutralization by gas ions. This, in turn, could be a reason for the increase in the apparent bulk conductivity observed at those peripheral locations, as exhibited in Figure 5.22. However, an estimation (not provided here for sake of brevity) in accordance to the approach proposed in [144] demonstrates negligible contribution of gas neutralization in this case.

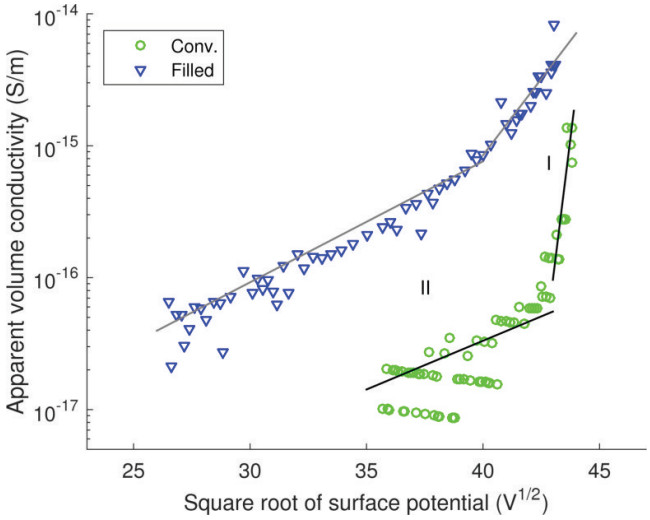

Figure 5.20. Field-dependent volume conductivity of enamels derived from SPD measurements at charging voltage of 4 kV.

Table 5.3. Relative permittivity derived from the field-dependent conductivity assuming Poole–Frenkel mechanism.

Calculated parameters	Conventional enamel	Filled enamel
ε_r in region I	0.017	0.784
ε_r in region II	6.15	4.99

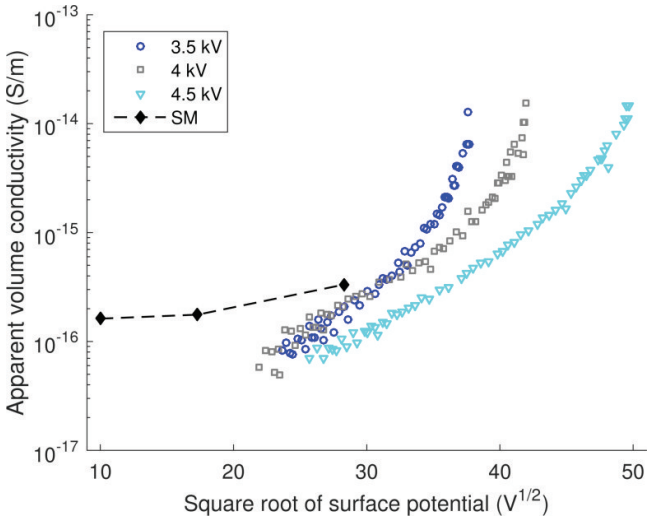

Figure 5.21. Field-dependent volume conductivity of the filled enamel derived from SPD measurements at three charging levels marked in the legend. The volume conductivity measured by the standard method (SM) [15] is shown by the dashed curve.

The deviation between the results attained by the SPD measurements and the standard method [15] as well as by using SPD data at different locations implies that intrinsic conduction should not be the main mechanism for potential decay in our tests. Extrinsic conduction processes such as charge injection at the air–insulation interface may take place, thus contributing the potential decay. In fact, charge injection can be stimulated by the

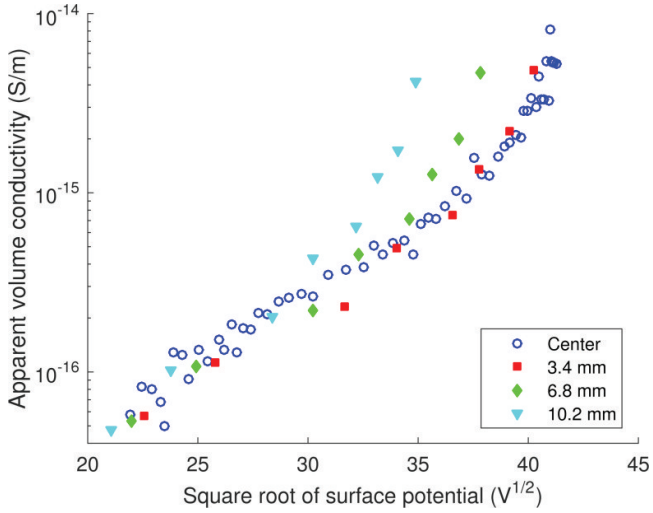

Figure 5.22. Field-dependent volume conductivity of the filled enamel derived from SPD measurement at charging voltage of 4 kV for the surface center and for different locations apart from the center as indicated in the legend.

presence of such a high initial electric field as ~5×10^7 V/m in the thin enamel layers [108]. Thus, the third component in the current continuity equation (5.15) cannot be neglected and the intrinsic conduction is not solely the contributor to the decay process. The apparent volume conductivity takes account of contributions of several mechanisms (intrinsic conduction, dipolar polarization as well as charge injection), and accounting for only one of them is erroneous, at least for the materials under consideration. The contribution of the intrinsic conduction seems to become important only at the very late stage of the decay process when the polarization is stabilized and the dynamics of injected charges is weakened. This argument is supported by the fact that the bulk conductivity derived at this period is comparable with its value measured by the standard method.

5.3.2.2. Potential decay due to polarization

Charges deposited on an insulation surface create an electric field inside the material that may stimulate the alignment of dipoles existing in the bulk, thus causing formation of bound charges inside the insulation. Even though the density of free surface charges is constant [108], the interaction between them and the formed bound charges results in a decay of surface potential. As can be noticed from the continuity equation (5.15), the contribution of polarization to decay process depends on material properties. If the intrinsic conduction in a material is extremely weak and the injected charges are negligible, polarization relaxation processes become the main factor affecting SPD. Polarization as a possible SPD mechanism was mentioned early [37], but its contribution to SPD had not been commonly reported in literature. A possible reason for that might be either the use of materials with relatively high electrical conductivity in experiments, thus manifesting the role of intrinsic conduction, or the use of very thin samples (thickness is in μm range) within which high electric fields are induced and promote the role of charge injection. In the last two decades, the role of dipolar polarization was systematically evaluated by Molinié and his coworkers [108, 137, 145]. The authors derived mathematical expressions relating the decay rate of surface potential and the

polarization current [137], thus providing a theoretical support for the model. Further in [145], a similarity was observed for the behavior of the time derivative of the surface potential and the absorption current described by Curie–von Schweidler law. Thus, dipolar polarization has been noted as the governing factor of SPD in epoxy resin 7 mm thick samples [137] as well as in thin films of HDPE and polypropylene (thickness ~10 μm) [145].

By correlating the applied electric field $E(t)$ and the displacement field $D(t)$ in materials through convolution relationships utilizing mutual dependent functions $\phi_D(t)$ and $\phi_E(t)$, the polarization current $i(t)$ and the decay rate of the surface potential $\mathrm{d}V(t)/\mathrm{d}t$ can be found as [108]:

$$i(t) = C_0 V_2 \phi_D(t)\,, \tag{5.17}$$

$$\frac{\mathrm{d}V(t)}{\mathrm{d}t} = \frac{LQ_0}{\varepsilon_0}\phi_E(t)\,, \tag{5.18}$$

where V_2 is a voltage applied for measuring the polarization current, C_0 is the geometric capacitance of the sample, Q_0 is the density of the initial deposited surface charges. By denoting $V_1 = LQ_0/\varepsilon_0$, the decay rate in eqn. (5.18) can be represented as:

$$\frac{\mathrm{d}V(t)}{\mathrm{d}t} = V_1\phi_E(t)\,. \tag{5.19}$$

As materials are assumed to have zero conductivity [108], the current $i(t)$ being referred to in eqn. (5.17) is the displacement current. In reality, the current $i(t)$ can be obtained by subtracting the component due to conduction from the measured polarization current. Besides, the function $\phi_D(t)$ can be represented as:

$$\phi_D(t) = \varepsilon_\infty \delta(t) + f(t)\,, \tag{5.20}$$

where ε_∞ is material relative permittivity at high frequencies, $\delta(t)$ stands for the Dirac function, and $f(t)$ being the dielectric response function. The latter is commonly employed to link the dielectric polarization $P(t)$ and the electric field $E(t)$ through a convolution relationship, which is presented, for example, by eqn. (6) in reference [146].

The following expression can be derived from eqns. (5.17) and (5.19):

$$\mathbf{L}\{C_0\phi_D(t)\}\mathbf{L}\{\phi_E(t)\} = \mathbf{L}\left\{\frac{i(t)}{V_2}\right\}\mathbf{L}\left\{\frac{\mathrm{d}V(t)}{V_1\mathrm{d}t}\right\}, \tag{5.21}$$

where operator $\mathbf{L}$ denotes the Laplace transform. Since the product of Laplace transforms for the functions ϕ_D and ϕ_E equals to unity [108], eqn. (5.21) can be rewritten:

$$C_0 = \frac{1}{V_2}\mathbf{L}\{i(t)\}\mathbf{L}\left\{\frac{\mathrm{d}V(t)}{V_1\mathrm{d}t}\right\}. \tag{5.22}$$

Hence, if the relationship (5.22) is fulfilled for the decay rate of the surface potential dV/dt and the displacement current $i(t)$, polarization can be considered as the main reason for the decay of the surface potential.

To examine the role of polarization in the decay process, we evaluate the right hand side of eqn. (5.22) utilizing the experimental results. Since $V_1 = LQ_0/\varepsilon_0$ being the induced surface potential at the instant immediately after charging ($t = 0$) is hard to attain experimentally, the initial measured potential V_0 is used instead of V_1. This introduces some error due to a discrepancy between these two quantities, which depends on time needed for obtaining V_0. Due to the nature of experimental data, the calculation would obviously provide the variation of the right hand side of eqn. (5.22) rather than a constant value.

For evaluating the right hand side of eqn. (5.22), two quantities should be obtained experimentally, namely the decay rate of the normalized potential and the polarization displacement current. As noted in section 5.3.1.1, the former obeys the power-law dependence:

$$-\frac{\mathrm{d}V(t)}{V_0\mathrm{d}t} = \begin{cases} M_1 t^{-n_1} & t < t_T \\ M_2 t^{-n_2} & t > t_T \end{cases}. \tag{5.13a}$$

On the other hand, deriving the polarization displacement current $i(t)$ from the measured polarization current may result in some uncertainties attributed to estimations of the current component due to conduction. This ambiguity can be avoided by noting that the magnitude of depolarization current can be found as the difference between the polarization and the conduction currents $i_{depol}(t) = i_{pol}(t) - i_{cond}$ [146], thus the depolarization current represents the same quantity as the polarization displacement current. Since the depolarization current can be easily measured, we utilize it for examining SPD mechanisms instead of the polarization displacement current. The depolarization currents obtained after a polarization period by applying different charging voltages V_2 (100, 300, and 800 V) are illustrated in Figure 5.3 and can be represented as:

$$i_{depol}(t) = \begin{cases} B_1 t^{-a_1} & t < t_K \\ B_2 t^{-a_2} & t > t_K \end{cases}. \tag{5.3}$$

As the curves of the decay rates and of the depolarization currents are featured by knee points at characteristic time t_T and t_K that are similar for each material, the calculation can thus be performed for each side of the knee points.

Laplace transform of the power-law function $t^{-\alpha}$ (α is a positive value but not integer) can be expressed as

$$\mathbf{L}\left\{t^{-\alpha}\right\} = \frac{\Gamma(1-\alpha)}{p^{1-\alpha}}, \tag{5.23}$$

where the gamma function is defined by:

$$\Gamma(\alpha) = \int_0^\infty x^{\alpha-1} e^{-x} dx. \tag{5.24}$$

Therefore, the right hand side of eqn. (5.22) becomes

$$R = \frac{B_j M_j \Gamma(1-a_j)\Gamma(1-n_j)}{V_2 p^{2-(a_j+n_j)}} = \frac{G_j}{p^{g_j}}, \tag{5.25}$$

where B_j, M_j, a_j, and n_j are defined in eqns. (5.3) and (5.13a); j = 1, 2.

The verification of the decay mechanism was implemented using the depolarization currents measured at three charging voltages and obtained results are similar for each type of the studied materials. Figure 5.23 demonstrate calculated results of the numerator G and the power factor g for both enamels in one of the cases (V_2 = 100 V). Each experimental result is represented by two points corresponding to the two time intervals on either side of the knee point. In the coordinate system illustrated in the figure, the ordinate presents the ratio between the numerator G and the geometric capacitance C_0 of the sample used in polarization current measurement, whereas the abscissa presents the power factor g. The horizontal dashed line corresponds to the equality $G = C_0$, and the vertical dashed line to the equality $g = 0$. The intersection of these dashed lines is marked by the point DP corresponding to both equalities $G = C_0$ and $g = 0$. In other words, the point DP indicates the fulfilment of eqn. (5.22) meaning that SPD is solely due to polarization. Note that the geometric capacitances are 24.6 pF and 20.5 pF for the samples of the filled and the conventional enamels, respectively. As seen from the figures, the experimental results for the filled enamel obtained for instants longer than the characteristic time ($t > t_T$) are represented by points close to the point DP (indicated by the region limited by the dashed ellipse in Figure 5.23a): the numerator G varies within less than one order of magnitude around the geometric capacitance C_0 and the exponent g is close to zero. This indicates that polarization is likely the most important contribution to SPD during

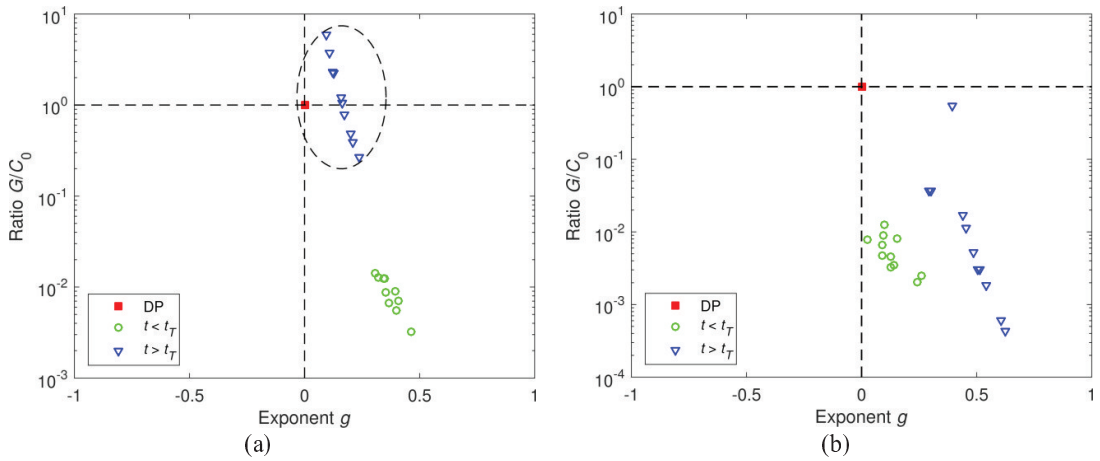

Figure 5.23. Calculated results for the numerator G and the exponent g in eqn. (5.25) at applied voltage 100 V for (a) the filled enamel and (b) the conventional enamel.

this period. For the time less than the characteristic time ($t < t_T$), the experimental results are illustrated by points that are far from the point DP: the exponent g is larger than it is in the previous case, while the numerator G is far below the value of the geometric capacitance C_0, suggesting that other mechanisms are dominating. For the conventional enamel, the same verification demonstrates that polarization is not dominant in the decay process at either time interval (Figure 5.23b). It should be noted that a more complicated process may take place during SPD in the conventional enamel due to the presence of two interfaces in its multi-layered structure.

5.3.2.3. Potential decay due to charge injection

Charging insulation surface by corona is associated with a deposition of ionic species in its external (drift) region. In case of air, these can be ionic clusters *e.g.* $(H_2O)_nH^+$, $(H_2O)_nNO^+$, $(H_2O)_nNO_2^+$ for positive discharge or ions CO_3^- produced by negative corona. Specific types of generated ions depend on atmospheric conditions, *e.g.* humidity, temperature, and pressure [147]. The ions could be either remained on the surface layer of the insulation or neutralized due to electron transfer brought about by the difference in energy states between the ions and the surface. Consequently, electrons or holes are formed in the surface states [39]. The dynamics of the formed charge carriers would account for the decay process, while the neutralized ions would not contribute further. In general, both surface and bulk traps exist in insulating materials and the former is considered as energetically deeper than the latter. Thus, a part of charge carriers is trapped in deep surface traps and will not be released within the measuring time [34]. Meanwhile, the other part of charges would be injected into the bulk due to the fact that a high electric field induced by charges lowers the potential barrier height for injection [39].

Charge injection and transport have been considered as the main mechanism responsible for the decay of surface potential in numerous investigations [34, 38, 39, 93, 138, 139]. The common need for the charge injection is the presence of an electric field as high as 10^7–10^8 V/m. In the present study, the initial field inside the samples varied in the range of (2.8–6.8)×10^7 V/m depending on the charging voltage magnitudes and the thickness of enamels used, thus charge injection may take place. Recently, it has been revealed in space charge measurement that charge injection occurs not only from the gas–insulation interface where charges were deposited, but also from the grounded metal–insulation interface [95]. These observations create a foundation for use of the bipolar charge injection model [44] for analyzing SPD on polymers. Verification of the model by employing computer simulations in [96] demonstrated a qualitative rather than quantitative agreement between the simulated and experimental results.

It should be noted that the described model based on charge injection is applicable for single-layered insulations. For multi-layered structures such as enamel coatings, on the other hand, the decay mechanism has not fully understood yet. Since experiments showed a remarkably slower SPD process on the multi-layered enamel as compared to that on the single-layered materials resembling its constituents (section 5.3.1.3), the role of the interface between polymeric layers in the studied enamels cannot be ignored while considering the decay mechanism. Experimental results obtained in section 4.1.2 suggest that the insulation

interface acts as a barrier hindering charge transport through insulation bulk. Thus, modifications should be introduced in the charge injection model for the single-layered insulation to account for the effect of the interface(s) in the multi-layered counterpart.

Based on the provided analysis, one can suggest that SPD on the filled enamel is initially controlled by the injection and hopping transport of charges in the bulk. Charge deposition on the air–insulation interface would lead to the appearance of induced charges with opposite polarity at the metal–insulation interface. This stimulates the bipolar charge injection, but the injection intensity should not be the same at both surfaces. As demonstrated in [148], insignificant space charges are accumulated in the insulation bulk of PEI films as compared to that in PAI films, indicating that the potential barrier height for charge injection is higher for the former than for the latter material. This observation is in line with the assumption that PEI is characterized as a more resistive material than PAI (section 5.1). Therefore, it can be hypothesized that charge injection from the grounded conductor into the PEI base coating is weak. The injection of electrons or holes into the filled PAI top coating and their transport driven by own field seem to be the dominating mechanisms during the first stage, starting immediately after corona charging up to the characteristic time t_T. When charges reach the interface between two layers in the enamel, the charge transport becomes limited. A part of charges arrived at the interface would be captured in deep traps existing in the interfacial regions. The remaining part of charge carriers penetrates through the interface and continues the hopping transport in the bulk of the second layer until reaching the grounded copper conductor. The contribution of charge injection to the decay mechanism will be further examined in section 5.4 by computer modeling.

Meanwhile, the electric field in the insulation induced by charges on the sample surface accounts for the relaxation polarizations that also affect SPD. Since electrical conductivity is different for PAI and PEI layers, interfacial polarization would arise, giving rise to charge accumulation at the interface between the layers. Similarly, charges can be observed at the interfaces between the fillers and PAI insulation of the top coating. The contribution of the interfacial polarization in the total decay process gradually increases, while the effect of charge transport weakens. As a support for the proposed hypothesis, the interfacial polarization between two insulation layers of the filled enamel is characterized by a loss peak frequency as low as $\sim 10^{-5}$ Hz corresponding to a relaxation time $\sim 10^{4}$ s (section 5.2.4). Eventually, as the polarization is stabilized, the potential decay is mainly due to the intrinsic conduction. The time evolution of dominant SPD mechanisms is illustrated in Figure 5.24 for the filled enamel.

A SPD mechanism similar to that described above may act in case of the conventional enamel. Charge injection is likely to take place at the initial stage after corona charging, followed by the large contribution of polarization relaxation processes (after observation of the knee point in the decay rate curve). However, polarization is still not the prevalent decay mechanism afterward, as discussed in section 5.3.2.2. The presence of the two interfaces in the material structure may result in a more complex decay mechanism of surface potential. This topic, however, will not be further analyzed in the present study.

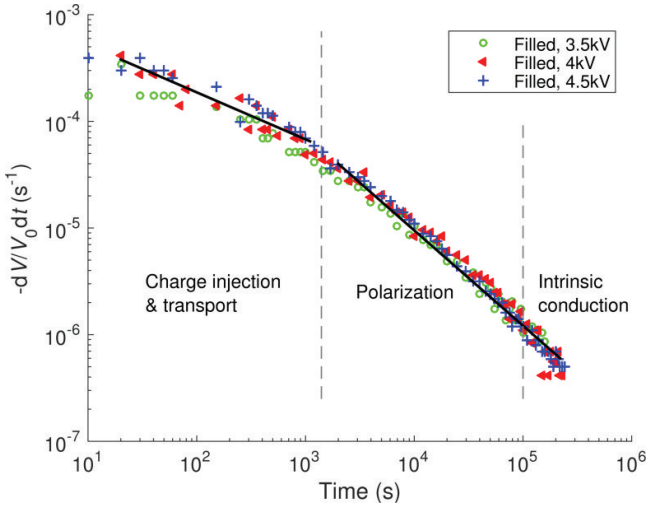

Figure 5.24. Schematic illustration of dominant SPD mechanisms for the filled enamel based on the decay curve of the normalized potential.

5.3.3. Charge mobility evaluations

As suggested and discussed above, ionic charges generated by corona in air and deposited on insulation surfaces may stimulate electron transfer with the surface states, thus leading to the appearance of mobile electrons or holes in the bulk of the enamel insulations. These injected charges are driven by a high electrical field in the material and contribute to the total transported charges. In this section, the mobilities of charge carriers are deduced from the results of SPD measurements using a similar approach as employed in section 4.2.3 (that the calculation was based on expression (4.3)). Recalling that the charge carriers injected from the air–insulation interface dominate over charges of opposite polarity injected from the metal–insulation interface as well as over mobile charges inherently existing in the studied materials, the mobility of injected holes can be obtained from the experimental results corresponding to positive corona charging, whereas electron mobility is estimated from those at negative charging voltage.

The calculated charge mobility in single-layered PAI with and without Cr_2O_3 fillers is provided in Table 5.4. The results derived from SPD on the enamel insulations are shown in Figure 5.25 as functions of the initial electric field. As seen, the mobilities of both types of charge carriers are higher for the filled enamel than for the conventional one. For both enamels, the electron mobility increases with enhancing initial electric field, while the hole mobility is field-independent.

As it is found, the charge mobility in the filled PAI layer is nearly 50 times higher than that in the filled enamel. As a result, the transit time of charge carriers within the filled-PAI top coat of the filled enamel is just ~20 s. Hence, the transit time of ~(1–2)×10^3 s within the filled enamel, which corresponds to the knee point observed in the experimental decay rates shown in Figure 5.17, should be mainly due to charge transport in the PEI base coat. This implies that the charge mobilities are similar in PEI and in the filled enamel. In fact, the latter statement is reasonable as shown by the following estimation. Recalling that the charge

Table 5.4. Charge mobilities in PAI with and without Cr_2O_3 fillers at the initial electric field of ~(3–4)×10^7 V/m.

Material	Mobility, $m^2V^{-1}s^{-1}$
PAI	1.3×10^{-14}
Cr_2O_3-filled-PAI	2.5×10^{-14}

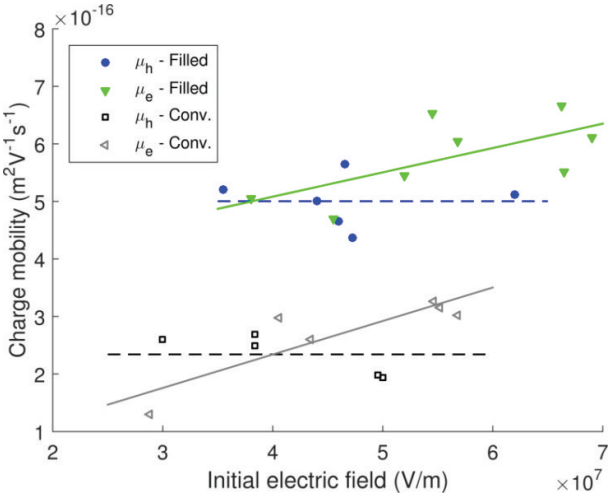

Figure 5.25. Charge mobilities as functions of the initial electric field. The fitted lines indicate tendencies of the variations. Each data point was derived from experimental results of a single SPD measurement.

mobility can be calculated as $\mu = L/(t_{tr}E)$ assuming insignificant accumulation of space charges in the insulation, the transit time of ~(1–2)×10^3 s correlates to the charge mobility of ~(3–4)×10^{-16} $m^2V^{-1}s^{-1}$ in the PEI base coat, which is close to the values shown in Figure 5.25. The difference in charge mobility in the Cr_2O_3-filled PAI top coat and in the PEI base coat is in agreement with the fact that DC conductivity is around two orders of magnitude higher for the former material than for the latter (section 5.1).

5.4. Simulations of charge transport in insulating materials during potential decay

As discussed, charge injection and transport play an important role in SPD on the filled enamel. In this section, a numerical approach is considered for modeling the generation and transport of charge carriers in the material under experimental conditions of the present study. This model is featured by two underlying distinctions as compared to the one described in section 3.3 and utilized for analyzing the transient processes in LDPE and its nanocomposites in section 4.4. Firstly, the barrier effect of PAI–PEI interface on the charge transport in the multi-layered structure is included. Secondly, the model outcomes are different in two cases. The characteristics to be fitted here are the time-varying surface potentials on the enamel insulation instead of the measured currents in LDPE and its nanocomposites for the previously considered model. Modifications introduced in the charge transport model are described in details below.

5.4.1. Peculiarities of the charge transport model in multi-layered insulations

5.4.1.1. Charge accumulation due to MWS polarization

Prior to describing the model of charge transport in multi-layered insulations, let us recall the effect of MWS polarization. We consider the double-layered insulation as shown in Figure 5.26, which is exposed to a DC voltage V. Owing to the difference in dielectric properties of the layers, charge carriers are accumulated at the interface between two materials. The time variation of the interfacial charge density can be found as [149]:

$$Q_{iDC}(t) = \frac{\sigma_2\varepsilon_1 - \sigma_1\varepsilon_2}{\sigma_1 L_2 + \sigma_2 L_1} V\left(1 - \exp\left(-\frac{t}{\tau}\right)\right), \tag{5.26}$$

where σ and ε stand for DC conductivity and permittivity of materials, L being layer thickness, the subscripts 1 and 2 respectively denote the bottom and top layers. The time constant τ is expressed as:

$$\tau = \frac{L_2\varepsilon_1 + L_1\varepsilon_2}{L_2\sigma_1 + L_1\sigma_2}. \tag{5.27}$$

Note that no charge accumulation takes place at the interface if the relationship $\varepsilon_1/\sigma_1 = \varepsilon_2/\sigma_2$ is maintained, which is rarely the case in reality. The time variation of the interfacial charge density $Q_{iDC}(t)$ is illustrated in Figure 5.27 for the time constant $\tau = 1.3\times10^4$ s calculated by

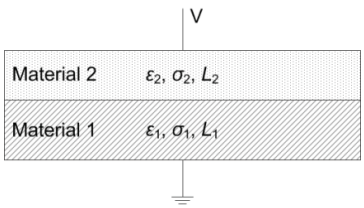

Figure 5.26. Multi-layered structure of insulating materials. Each layer is featured by dielectric permittivity (ε), DC conductivity (σ), and thickness (L).

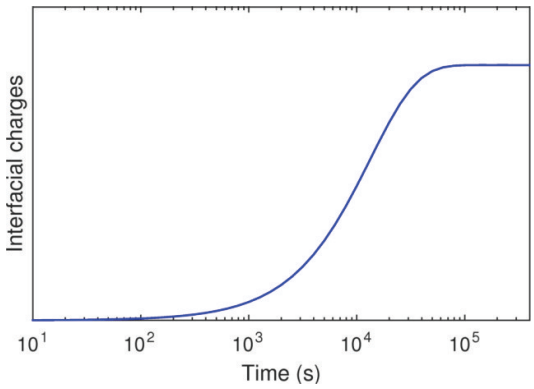

Figure 5.27. Time-dependent interfacial charges due to MWS polarization caused by the application of a DC voltage. The curve is plotted for $\tau = 1.3\times10^4$ s, which is the time constant of the MWS polarization at the interface between the top and base coats of the filled enamel.

using the materials properties of the base and the top coats in the filled enamel. The accumulation of the interfacial charges is then taken into account in the model of charge transport in a multi-layered insulation, which is presented in the following section.

5.4.1.2. The model

For the sake of clarity, the cross sectional view of a conductor covered with the filled enamel under consideration is again displayed in Figure 5.28a. As it is discussed in section 3.2.3.2, the insulation coating can be equivalently represented as a flat sample of an identical thickness. Thus, the transport of charge carriers in the filled enamel can be investigated in a 1D domain along x direction as depicted in Figure 5.28b. The position of the conductor–insulation interface is assigned to the coordinate $x = 0$, while the air–insulation interface corresponds to the coordinate $x = L$, with $L = L_1 + L_2$. The geometrical and dielectric properties of the layers provided in sections 5.1 and 5.2 are summarized in Table 5.5.

Deposition of ionic charges on the insulation surface by corona discharge induces an electric field inside the material. Due to the presence of a sufficiently high electric field, charge carriers are injected into the bulk [39]. The injected current density is assumed to have a form similar to that describing Schottky's injection:

$$j_2(t) = Q_2(t) v_0 \exp\left(-\frac{q(\varphi_2 - \Delta\varphi_2)}{kT}\right). \tag{5.28}$$

Here, $Q_2(t)$ denotes the time-varying density of surface charges on the air–insulation interface, C/m^2; φ_2 is the barrier height for charge injection at this interface, eV; v_0, q, k, T are quantities as previously determined. The pre-exponential factor $Q_2(t)v_0$ was adopted from [150], where an expression was introduced for describing the current density injected from surface charge

Table 5.5. Dielectric properties of the two layers of the filled enamel.

Parameters	PEI (base coat)	filled PAI (top coat)
Thickness L, μm	25	15
DC conductivity σ, S/m	6×10^{-17}	$(4–8)\times10^{-15}$
Relative permittivity ε_r at high frequency, 1	3.5	4.0

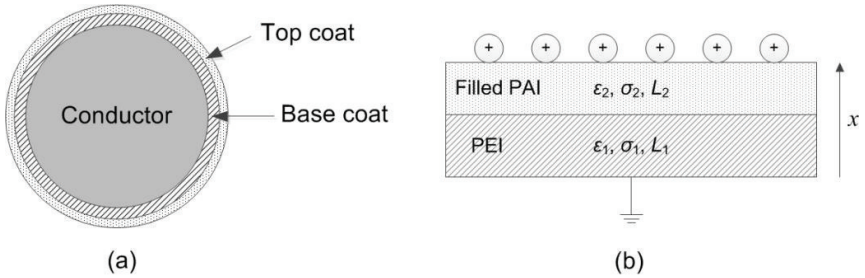

Figure 5.28. Cross section of the enameled wire (a) and the equivalent structure of enamel coating (b). Each layer is featured by dielectric permittivity (ε), DC conductivity (σ), and thickness (L).

layer into the insulation bulk. At the same time, charges are also injected from the grounded conductor–insulation interface that leads to the presence of charges in the base coat. By assuming Schottky mechanism, the density of this injected current is expressed as:

$$j_1(t) = AT^2 \exp\left(-\frac{q(\varphi_1 - \Delta\varphi_1)}{kT}\right). \tag{5.29}$$

Here, φ_1 is the barrier height for charge injection at the interface, eV; $\Delta\varphi_i$ (i = 1, 2) indicates the reduction of barrier heights due to the induced field as defined in section 3.3.1.

As for the single-layered insulations, the charge transport in multi-layered dielectrics is also governed by the system of equations (3.4)–(3.7) and it is associated with various processes including charge trapping, de-trapping, and recombination, the rates of which are expressed by eqns. (3.9)–(3.11). On the other hand, the difference in material properties of the two layers accounts for the discontinuity in parameters' values at the PEI–PAI interface. For example, the electron mobility is abruptly altered as:

$$\mu_e = \begin{cases} \mu_{e(\text{PEI})} & \text{for } x \le L_1 \\ \mu_{e(\text{filled PAI})} & \text{for } x > L_1 \end{cases}. \tag{5.30}$$

Also, the PEI–PAI interface is considered as a barrier hindering the transport of charge carrier from one layer to the other. This behavior is attributed to the existence of deep surface traps that act as trapping sites capturing a part of mobile charges reaching the interface. The barrier effect of the interface can be implemented in the simulation through a change in the conduction current. Thus, the current density j_p penetrating through the interface is assumed to be a proportion of the current density j_r reaching it:

$$j_p(L_1,t) = k_p j_r(L_1,t), \tag{5.31}$$

where the penetration coefficient k_p denotes the proportion of current passing through the interface. Hence, the discontinuity in the current density at the interface $\Delta j(L_1,t)$ can be represented as:

$$\Delta j(L_1,t) = j_r(L_1,t) - j_p(L_1,t) = k_c j_r(L_1,t), \tag{5.32}$$

with the capturing coefficient $k_c = 1 - k_p$ showing the fraction of charge carriers being captured at the interface, $0 \le k_p, k_c \le 1$.

Different values of the capturing coefficient k_c are considered in the model, specifically, $k_c = 0$, $k_c = const$, and time-dependent k_c expressed in eqn. (5.33) below. Note that the discontinuity in the current density at the interface only arises in the latter two cases.

$$k_c(t) = \Lambda \exp\left(-\frac{t}{\tau}\right) \tag{5.33}$$

In eqn. (5.33), τ is the time constant of the MWS polarization taking place at the interface between the PEI and the filled-PAI layers, whereas the pre-exponential factor A is adjusted for achieving the best fit of the experimental data. Utilizing the introduced quantities, one can find the total amount of the accumulated interfacial charges as:

$$Q_{inf}(t) = \int_0^t k_c(t_0)\, j_r(L_1, t_0)\, \mathrm{d}t_0 \,. \tag{5.34}$$

The time-dependent surface charge densities at the air–insulation and conductor–insulation interfaces can be respectively expressed as:

$$Q_2(t) = Q_0 - \int_0^t j_2(t_0)\mathrm{d}t_0 - \int_0^t j_e(L, t_0)\,\mathrm{d}\,t_0 \,, \tag{5.35}$$

$$Q_1(t) = -Q_0 + \int_0^t j_1(t_0)\mathrm{d}t_0 + \int_0^t j_h(0, t_0)\,\mathrm{d}\,t_0 \,. \tag{5.36}$$

For avoiding ambiguity, equations (5.35)–(5.36) are written for the case of positive corona charging. Here, Q_0 is the surface charge density initially deposited by corona discharge and $-Q_0$ is the induced surface charge density at the counter electrode. The second terms in the equations indicate the losses of the surface charges due to the charge injection. As Ohmic contacts are hypothesized, charges of opposite polarities reaching counter electrodes disappear from the insulation without any extraction barrier. These charges contribute to the neutralization of surface charges at both electrodes, which are presented by the third terms in these equations. The current densities $j_e(L,t_0)$ and $j_h(0,t_0)$ are respectively due to electrons arriving at the air–insulation interface and holes arriving at the conductor–insulation interface. For negative corona charging, some minor modifications should be introduced in these expressions.

Finally, the externally measured surface potential is derived as:

$$V_s(t) = \int_0^L E(x,t)\,\mathrm{d}\,x \,. \tag{5.37}$$

The simulation of charge transport in the filled enamel is implemented by considering the initial time $t = 0$ corresponding to the instant when the corona charging ceases. It is assumed that no charge injection takes place during corona charging, *i.e.* neither mobile nor trapped charges are present in the insulation at $t \leq 0$. This assumption is justified by the considerable difference between the charging duration and the transit time. As the surface charge density $Q_2(t)$ was time-varying, it must be updated at every time step prior to the calculation of the injected current density $j_2(t)$ in accordance to eqn. (5.28). Other measures for implementing the model have been described in section 3.3.2.

Table 5.6. Model parameters for simulation of SPD on the filled enamel.

Parameters	PEI	filled PAI
Injection barrier heights φ, eV	1.28	1.06
Effective mobilities $\mu_{e,h}$, $m^2V^{-1}s^{-1}$	4×10^{-16}	1×10^{-14}
Trapping coefficients $t_{e,h}$, s^{-1}	5×10^{-3}	
Deep trap densities $N_{etr,htr}$, m^{-3}	6.25×10^{20}	
De-trapping barrier heights $\varphi_{etr,htr}$, eV	0.96	
Recombination coefficients, m^3s^{-1}		
r_{etrhtr}	6.4×10^{-22}	
r_{ehtr}	6.4×10^{-22}	
r_{hetr}	6.4×10^{-22}	
r_{eh}	0	
Temperature, K	295	

Computer simulations of the above-described model for charge transport in the filled enamel were performed in a 1D computational domain using finite element software COMSOL Multiphysics. The set of model parameters used for the simulations is presented in Table 5.6. Different barrier heights for charge injection at the interfaces are used in the model owing to the remarkable distinction in the measured space charge profiles in the materials of the two layers [148]. Since less space charges were observed in PEI than in PAI, fewer charges should be generated in the former, thus the barrier height for charge injection into PEI was set to be much higher (1.28 eV) as compared to that of the Cr_2O_3-filled PAI layer (1.06 eV). The mobilities of charge carriers in both layers are close to the values estimated in section 5.3.3. As the field dependence of the mobility is rather weak, constant parameters were accepted. Also, since the derived mobilities of electrons and holes differ slightly, they are considered to be equal in the model. Other model parameters have been obtained by an optimization using various parametric studies. For such procedure, the parameters previously derived for the model of charge transport in LDPE [46] were used as initial guesses. The symmetry of the model parameters for electrons and holes was adopted in this work due to the fact that the potential decay is independent on the polarity of the corona charging. Due to the weak frequency dependence of the relative permittivities (see section 5.2.1), the parameters for PEI and Cr_2O_3-filled PAI were set to the values obtained in the measurements at high frequency for the conventional and filled enamels, respectively (see Table 5.5).

5.4.2. Results and discussion

5.4.2.1. Results obtained by ignoring the barrier effect of the interface

The simulation was initially performed without accounting for the barrier effect of the interface between the base and top coats of the filled enamel (k_c = 0), thus no interfacial charges were accumulated. The results depicted in Figure 5.29 show faster decay than that recorded in the experiments, especially at high magnitudes of the charging voltage. Additionally, one may notice that the simulated surface potentials for three levels of the charging voltage become identical at time $t \geq 4\times10^4$ s that was not observed in the measurements. The discrepancy between the simulated and experimental data implies that the model without considering the barrier effect of the interface is not fully sufficient to account for the charge transport processes in the studied filled enamel. Hence, the contribution of the interface between the two layers in the enamel insulation must be included in the model.

5.4.2.2. Results obtained by considering the barrier effect of the interface

The discontinuity in fluxes of charge carriers was realized in the model by selecting suitable capturing coefficient k_c, which was constant (k_c = 0.38) in one case and time-dependent in another case. For the latter, it was assumed that the magnitude of k_c followed eqn. (5.33) with pre-exponential factor A = 0.5 and the time constant $\tau = 1.3\times10^4$ s that resulted in its time variation depicted in Figure 5.30. The time constant τ was calculated by using the material properties of the base and the top coats of the filled enamel. This time constant is associated with the loss peak of the MWS polarization at the interface detected at frequency of ~10^{-5} Hz (see section 5.2.4). The time-varying nature of the coefficient k_c can be hypothesized as follows. At the beginning of the charge transport process (after completing corona charging), as a majority of deep traps existing at the interface are empty, more charge carriers can be captured while less charges are able to penetrate through the interface. It is thus assumed that a half of mobile charges are trapped at the PEI–PAI interface, while the other half is transported through it. Since these traps are gradually filled with time, the probability that charge carriers are being captured is reduced and, hence, more charges can penetrate through the interface. At long time instants, as most of traps are already filled, a

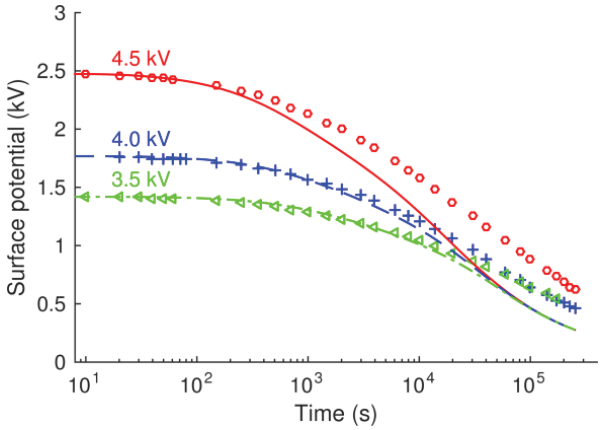

Figure 5.29. Comparison of surface potentials on the filled enamel obtained in measurements (markers) and simulations (curves) while ignoring the barrier effect at the PEI–PAI interface.

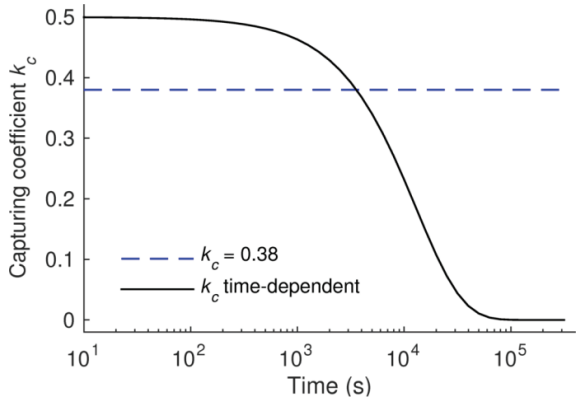

Figure 5.30. Values of the capturing coefficient k_c used in simulations.

large proportion of charge carriers arriving at the interface can continue their transport in the second layers without being trapped. This results in a small capturing coefficient k_c, which is equivalent to the continuity of the current density at the interface. As an illustration, at the time of 4×10^4 s (~3τ), the capturing coefficient k_c is as low as 0.025 that corresponds to a very tiny amount of charges captured at the interface.

Simulated surface potential decay characteristics yield a very good agreement with experimental results in both cases of constant and time-varying capturing coefficients k_c, as shown in Figure 5.31. Contributions of the interface in the decay of surface potentials are evaluated by comparing the simulated results in case when the barrier effect of the interface is accounted in the model and when it is not (Figure 5.32). One may observe that the latter model clearly accelerates the potential decay as compared to the one including the barrier effect. The differences between the surface potentials obtained in two models are shown by dash-dotted curves in the figure. As seen, these potential components start increasing after 10^3 s and they become saturated at ~$(2–4)\times10^4$ s, thus indicating the strong impact of the barrier effect to the charge transport in time interval of (10^3–4×10^4) s.

5.4.2.3. Charge accumulation at the interfaces and in the bulk

The total amount of space charges accumulated in the insulation can be obtained by integrating the charge density over the insulation thickness L as follows:

$$Q_{SC}(t) = \int_0^L \rho(x,t)\mathrm{d}x\,. \tag{5.38}$$

The resulting quantity is the charge per unit of area (C/m^2) and has the same dimension as for surface charge density. The time variation of the total space charges accumulated in the bulk

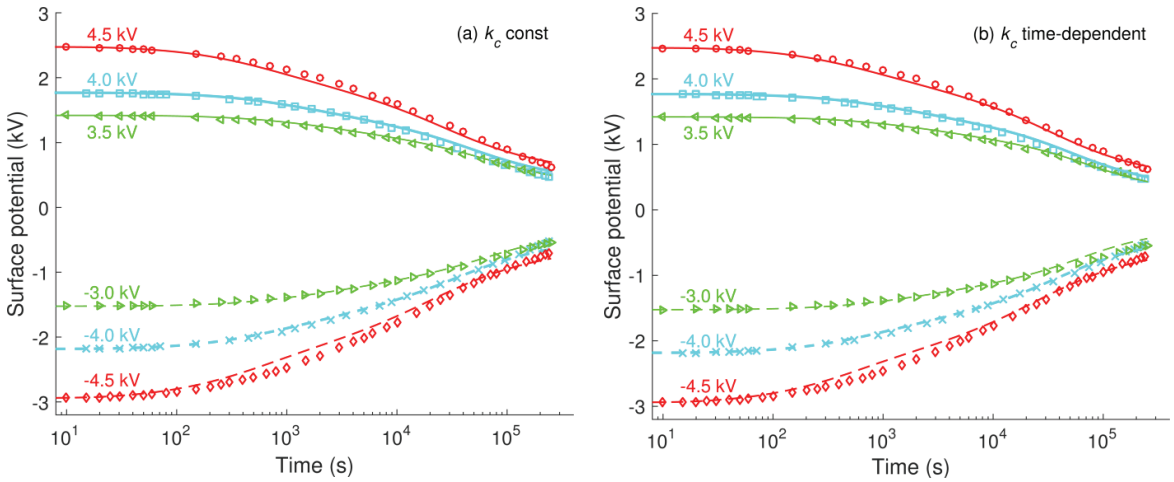

Figure 5.31. Simulated surface potentials (illustrated by solid and dashed curves) obtained for different capturing coefficents k_c and their comparison with the experimental results (markers). The simulated and experimental results at each magnitude of the charging voltage are depicted by the same color.

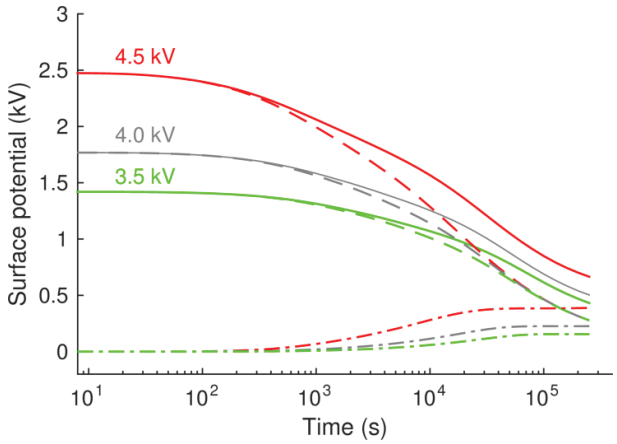

Figure 5.32. Simulated surface potentials obtained from the model with (solid curves) and without (dashed curves) considering the barrier effect of the interface. The difference between them (dash-dotted curves) shows the blocking impact of the interface to potential decay. The results at each magnitude of the charging voltage are depicted by the same color.

is presented in Figure 5.33 together with the charge densities at both surfaces and at the PEI–PAI interface of the studied enamel. Note that in the current and the following sections, only the results obtained for the case of the charging voltage of +4.5 kV are shown. For lower magnitudes of the charging voltage and for the negative polarity, similar results were attained and, thus, they are not depicted here.

As seen in the figure, the total amount of space charges reaches its maximum at around $(1–2)\times10^4$ s. The reduction in their quantity observed afterwards is attributed to the enhanced injection of electrons into the bulk from the cathode, leading to growing intensity of the recombination process. As for the surface charges, positive ionic charges deposited at the anode result in the appearance of induced charges of opposite polarity with the same magnitude at the cathode. While the charge density at the anode gradually decreases with time and becomes negligible at $t \sim 10^5$ s, significant reduction in the magnitude of the induced charges at cathode starts only after 10^4 s. It is noteworthy that a minor reduction in the charge density at the anode is observed within the first 100 s, which suggests the plausibility of the assumption of no charge injection during corona charging within two minutes. It is notable that the sum of the densities of surface charges at the anode, at the cathode, and at the interface as well as of the total space charges in the bulk is zero at any time instant as shown by the dash-dotted curve in Figure 5.33:

$$Q_1(t) + Q_2(t) + Q_{inf}(t) + Q_{SC}(t) = 0. \tag{5.39}$$

Charges are gradually built up at the PEI–PAI interface and the time variation of their density depends upon the magnitude of the capturing coefficient k_c used, as shown in Figure 5.34. Thus for the constant k_c, the interfacial charges are continuously accumulated during the decay process. For the time-varying k_c, the density of the interfacial charges reaches saturation at $\sim10^4$ s, which is close to the time constant τ. Such behavior is similar to the results of the analysis for the case with a constant voltage V applied to a double-layered

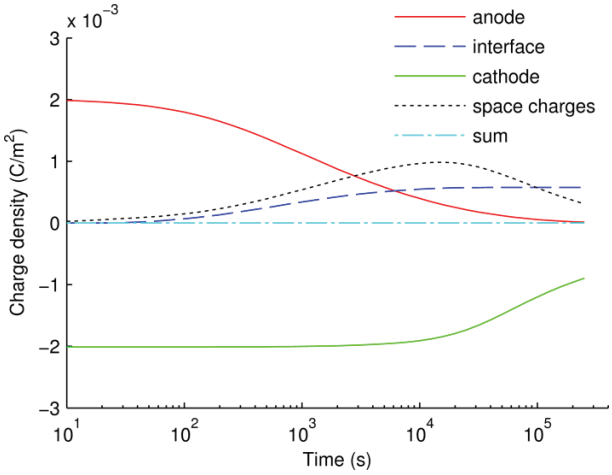

Figure 5.33. Surface charge densities and total space charges accumulated in the bulk of the filled enamel obtained in the model with time-dependent k_c. The corona charging voltage is +4.5 kV, the anode corresponds to the air–insulation interface while the cathode is the conductor–insulation interface.

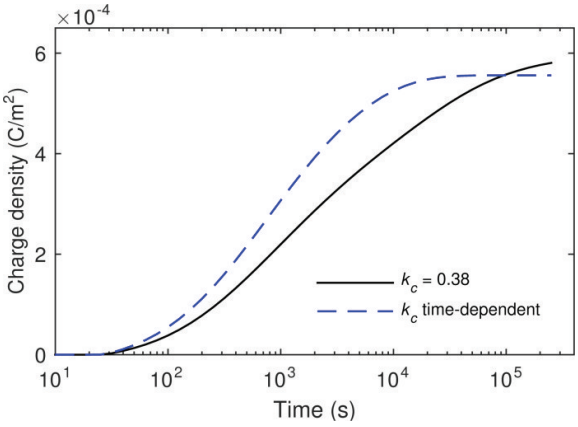

Figure 5.34. Interfacial charge densities obtained in models with constant and time-dependent capturing coefficients k_c.

insulation, as illustrated in Figure 5.27. This observation implies that the model with the time-dependent k_c appears to be most suitable for describing the contribution of the interface to the charge transport in multi-layered insulations.

5.4.2.4. Contributions of charge injection at each interface to the potential decay

Contributions of charge injection at each interface of the insulation to the total decay of the surface potential are examined in this section. For this, we define the reduction of surface potential $\Delta V(t)$ as a difference between the initially measured surface potential V_0 and the surface potential $V(t)$ obtained at a given time t during the decay process:

$$\Delta V(t) = V_0 - V(t)\,. \tag{5.40}$$

For calculating the potential reduction $\Delta V(t)$, three charge transport models are considered, as outlined in Table 5.7. They include unipolar models taking into account charge injection

Table 5.7. Different models of charge transport in multi-layered insulation.

Model	Description
#1	Bipolar charge injection
#2	Unipolar charge injection at the air–insulation interface
#3	Unipolar charge injection at the conductor–insulation interface

either from the air–insulation interface or from the conductor–insulation interface only. The model considering charge injection from both interfaces, *i.e.* the bipolar charge injection model that has been discussed in section 5.4.2.2, is employed as a reference. Contributions of charge injection at each interface can be found from the results of the respective unipolar injection model. Since only charges of the same polarity (either positive or negative) are presented in unipolar injection models, charge recombination is not incorporated in the simulation. The models were implemented using the time-dependent coefficient k_c followed eqn. (5.33). Other model parameters are the same as those provided in Table 5.6.

The reduction of surface potential $\Delta V(t)$ (5.40) calculated by the different models in Table 5.7 are shown in Figure 5.35 for the charging voltage of 4.5 kV. As seen, the unipolar model featuring charge injection at the air–insulation interface results in a higher potential reduction, whereas the one accounting for charge injection at the conductor–insulation interface leads to a discernable potential reduction only after 5×10^4 s. The results shown in the figure reflect the difference in the intensity of charge injection at each interface, as can be compared in Figure 5.33. The dash-dotted curve in Figure 5.35 represents the sum of the potential reductions acquired from the two unipolar models. It is noteworthy that this sum is still lower than the potential reduction obtained in the bipolar model.

Even though the charge injection at the air–insulation interface and the resulting charge transport in the bulk play a crucial role in the decay process, the effect of the charge injection at the conductor–insulation interface cannot be neglected. Its contribution can be found by comparing the time-varying surface charge densities and the electric field profiles obtained in models #1 and #2, which are shown in Figures 5.36 and 5.37. As seen, the densities of surface charges at the anode and the electric field within the top coat at indicated time instants are identical for both models. In contrast, the density of surface charges Q_{inf} accumulated at the PEI–PAI interface is significantly higher for the unipolar model than for the bipolar one (Figure 5.36), as charge neutralization by carriers of opposite polarity takes place only in the latter model. Since the interfacial charge desnity Q_{inf} represent the discontinuity in the displacement field D within two layers

$$D_1 - D_2 = Q_{inf}\,, \tag{5.41}$$

the field D should be subjected to a larger jump in the unipolar model #2, and so for the electric field E, as illustrated in Figure 5.37. The magnitudes of charge densities at the PEI–PAI interface (positive polarity) and at the cathode (negative sign) are higher for the model #2, as shown in Figure 5.36. Therefore, a considerably higher electric field in the PEI bottom layer was obtained in this model as compared to that for the bipolar model #1, see Figure 5.37. Recalling that the integral of the electric field over the sample thickness provides the

surface potential in accordance to eqn. (5.37), a higher surface potential $V(t)$ and, hence, a lower potential reduction $\Delta V(t)$ are attained in the unipolar model #2 as compared to the bipolar model #1, as demonstrated in Figure 5.35. Such differences in results of the models #1 and #2 are attributed to presence of charges of opposite polarity injected at the counter electrode.

In summary, the decay of surface potential is mainly due to the generation of charges by injection through electron transfer mechanism between the top coating layer and the layer of deposited charges produced by corona. Nevertheless, the role of charge injection at the counter electrode and space charges in the bulk cannot be neglected. This result indicates that the bipolar charge injection model is crucial for analyzing charge transport in insulating materials.

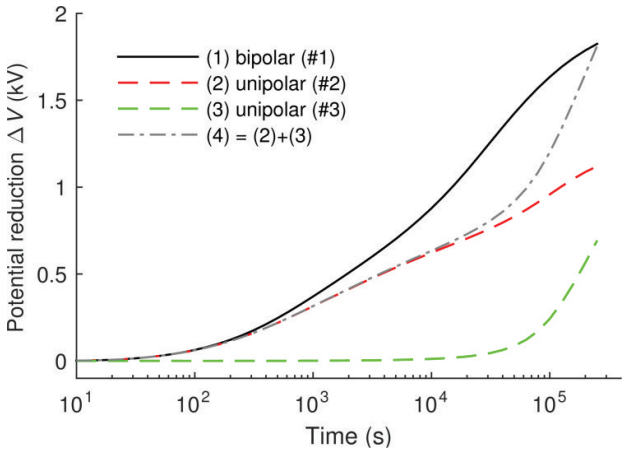

Figure 5.35. Potential reduction ΔV obtained in models considering charge injection at different interfaces. Curves (1)–(3) show respective results attained in models #1–#3 (Table 5.7).

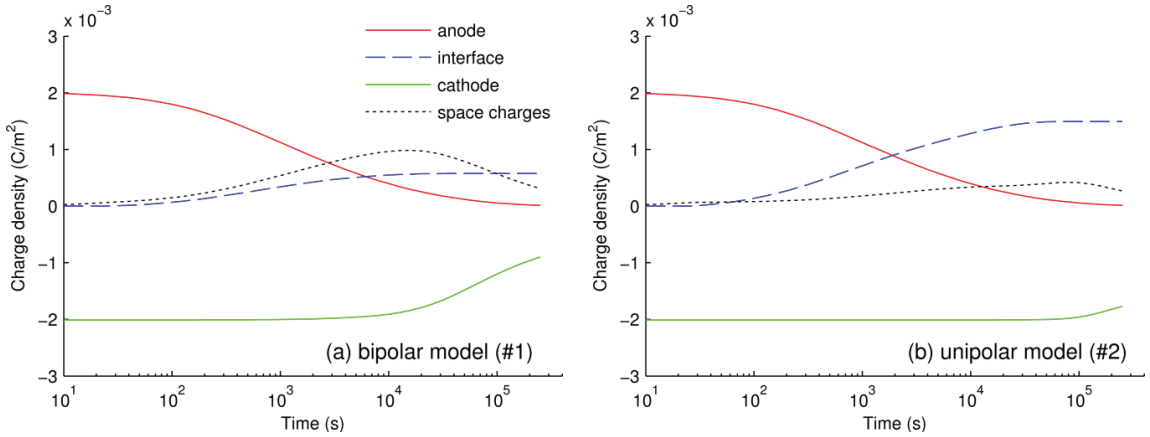

Figure 5.36. Surface charge densities and total space charge density obtained in (a) the bipolar model (#1) and (b) the unipolar model (#2) considering charge injection only at the air–insulation interface.

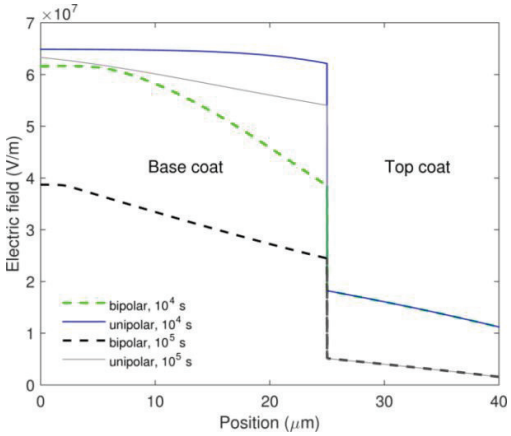

Figure 5.37. Distribution of electric field in the multi-layered enamel insulation obtained in the bipolar (#1) and unipolar (#2) models at indicated time.

6. Conclusions and future work

6.1. Conclusions

Charge generation and transport in two polymer composites were investigated in this thesis. As the material structure, properties of the base polymers and filler particles, and the filler size are different in two cases, the influences of the fillers on the considered processes are certainly dissimilar. The conclusions drawn from the work are therefore presented below separately in two parts.

6.1.1. Charge transport in low-density polyethylene and its nanocomposites

Experimental studies

Charge transport in LDPE filled with nanoparticles of alumina (Al_2O_3) and magnesia (MgO) as well as in the unfilled counterpart was investigated by measurements of DC conductivity, surface potential decay, and thermally stimulated discharge currents. As compared to the pure LDPE, remarkable reduction in the DC conductivity and considerable slower potential decay were observed for both LDPE nanocomposites at the filler content of 3 wt%. On the contrary, the material loaded with nanofillers at lower or higher percentages showed a less significant decrease in the DC conductivity. The results of conductivity measurements on multi-layered samples indicated that the internal interface between two insulation layers played a role as a barrier hindering charge transport through it. Meanwhile, results of SPD measurements on multi-layered samples strongly suggested that (a) charge injection at the air–insulation interface and the transport of injected charges were dominating in decay process; and (b) positive charges were prevailing in LDPE. Based on these, mobility of holes in the considered materials was deduced by using measured data on single-layered samples. At temperatures 20–60 °C, the parameter for both nanocomposites varied in the range of 2×10^{-15}–1.4×10^{-14} $m^2V^{-1}s^{-1}$, which was at least two times lower as compared to the corresponding of the unfilled LDPE (5×10^{-15}–5×10^{-14} $m^2V^{-1}s^{-1}$). Further, results of TSD current measurements demonstrated that the trap energy in LDPE/Al_2O_3 3wt% nanocomposite was clearly deeper than that in LDPE. In particular, the trap depth was 1.7–2.3 eV for the former and 1.1–1.3 eV for the latter. Thus, the reduced mobility of charge carriers and the increased trap depth were closely correlated with the weakened charge transport and the decreased DC conductivity of the nanofilled materials.

Additionally, by using the measured current densities and the calculated charge mobilities, lower activation energies were obtained for nanocomposites than for unfilled LDPE, indicating the weaker temperature dependency of the studied properties in nanofilled dielectrics. The field dependencies of the quasi-steady state current densities obtained in the DC conductivity measurements and the current densities derived from the SPD measurements

were analyzed, showing that the conduction mechanisms in studied materials were strongly affected by temperature and the presence of nanofillers, while SCLC was most probably the governing conduction mechanism in the considered materials.

Simulation studies

Computer models were used for simulating the dynamics of charge generation and transport in LDPE and its nanocomposites at different temperatures. By achieving a good agreement between simulated and measured conduction currents, quantitative changes in various physical processes in the insulating materials due to the presence of nanofillers have been revealed. In particular, the weakening charge transport in the nanodielectrics as compared to the unfilled LDPE was associated with the increased barrier heights for charge injection at electrodes, the reduced charge mobility, and the increased trap energy and trap density. Simulated results also showed that space charge accumulation and electric field enhancement were less noticeable in the LDPE nanocomposites than in the unfilled counterpart. The reduced conduction currents and the suppression of space charge accumulation in the nanofilled LDPE were most likely governed by the modification of the barrier heights for charge injection at the dielectric–electrode interfaces. Furthermore, the application of Schottky's mechanism for describing charge injection at electrodes in the simulation was still questionable as it did not fully explain the temperature dependence of the conduction currents obtained experimentally.

6.1.2. Charge transport and dielectric relaxation in enamel insulations

Experimental studies

Measurements of DC conductivity, dielectric response, and surface potential decay were used for characterizing electrical properties of two enamel insulations. The used enamels were featured by a multi-layered structure, consisting of at least two layers (a PEI base coat and a PAI coat on top of it). The considered partical discharge resistant enamel contained chromium oxide microfillers in the PAI top coating (referred to as the filled enamel), whereas the other was conventional material without filler particles (used as reference). Both enamels had low DC conductivities which were respectively 1.2×10^{-16} and 6×10^{-17} S/m at room temperature, while the property was found to be much higher for the top coat which was ~$(4–8)\times10^{-15}$ S/m. The results suggested that PEI was the most resistive among the layers and its DC conductivity should be in the same order as for the conventional enamel. The DC conductivity of chromium oxide filler was at least in eight orders of magnitude higher than that of the polymeric insulations. However, its introduction into the base polymer marginally increased the respective property of the filled enamel as the modification was only in the PAI top layer and the percolation level of the inclusions was not reached.

The dielectric responses of the studied enamels were characterized by dipolar relaxation at high frequencies (~10^5 Hz) and interfacial polarization at low frequencies (~10^{-5} Hz), the latter arising at the PEI–PAI interface. Chromium oxide filler was a strongly dispersive material, both the real and imaginary parts of its complex permittivity increased exponentially with reducing frequency. The additives gave rise to both the real and imaginary parts of the complex permittivity of the filled enamel as compared to those of the conventional one. By

analyzing the dielectric responses, it was found that the presence of chromium oxide fillers in the enamel insulation resulted in the increase of low frequency dispersion as well as the appearance of interfacial polarization at their interfaces with the base polymer.

The decay of surface potential was found to be considerably accelerated for the filled enamel as compared to that for the conventional one. For the considered materials, charge transport through the bulk was dominated in the charge decay, whereas surface charge leakage and charge neutralization by gas ions were found to be insignificant. The potential decay behavior was initially attributed to the difference in DC conductivity of the filled and conventional enamels. A detailed analysis revealed that the main processes contributing to SPD on the studied enamels are charge injection, polarization, and intrinsic conduction. For the filled enamel, charge injection and transport took place at the early stage of the decay (just after corona charging), followed by polarization process which dominated at intermediate time interval (10^3–10^5 s) and finally, intrinsic conduction became crucial at long instants (after 10^5 s). The involvement of polarization could be due to the presence of the PEI–PAI interface that hindered charge transport through the bulk. For the conventional enamel, a more complicated decay mechanism may act as two interfaces existed in its structure.

Results of SPD measurements allowed for deriving the charge carrier mobility in the insulations. The parameters were similar for holes and electrons and a weak field-dependent behavior was noted. In particular, the charge mobilities were in order of 10^{-16} $m^2V^{-1}s^{-1}$ and 10^{-14} $m^2V^{-1}s^{-1}$ in the PEI base coat and filled PAI top coat, respectively. The difference in the materials' parameters was in line with the fact that the DC conductivity of the former was around two orders of magnitude lower than that of the latter insulation.

Simulation studies

A numerical model was developed for studying charge transport in the filled enamel during potential decay. The model included the migration of charges into the material from the open surface and from the metallic counter electrode as well as their drift driven by the electric field induced in the insulation. A good matching between the simulated and measured surface potentials was achieved only in case the effect of the PEI–PAI interface was included in the model. Accordingly, the interface between two layers was considered as a barrier hindering charge transport and was featured by a capturing coefficient. The latter can be either a constant value or an exponential function of time that took into account the time constant of MWS polarization. Additionally, the charge injection at the air–insulation interface and transport of the injected charges were the most important contributor to the potential decay in the studied material, whereas the charge injection at the conductor–insulation interface and the interaction of space charges of opposite polarities in the bulk could not be ignored.

As the developed model provided a consistent prediction of the potential decay in the considered enamel insulation, its application in studying charge transport in similar multi-layered structures is therefore highly appropriate.

6.2. Future work

This work presents the study of charge transport in two different types of composite materials using both experimental techniques and computer simulation. While the former approach focused on recording macroscopic quantities such charging currents or surface potentials, the latter dealt with elementary processes, *e.g.* charge generation, transport, and trapping. The links between these approaches were attempted to be established by using various material properties such as charge mobility and trap depth derived from experimental results as inputs for the computer models. Despite the fact that many measurements were carried out in the present study, more data on material properties are still required.

The first suggestion for continuations of this investigation is apparently related to collecting additional experimental data so that a comprehensive picture showing the impact of temperature and field strength on charge transport in insulations, especially in LDPE nanocomposites, can be revealed. Based on that, the dependencies of charge mobility on temperature and electric field in broader ranges should be obtained. Such a collection of experimental results is beneficial not only for understanding the effect of nano- and mirco-particles on material properties, but also for elucidating the electrical breakdown in insulating materials as well as in developing reliable computer models of such processes.

It is also interesting to extend the implemented simulation work so that the intensity of charge transport can be compared for different applied electric fields and temperatures. On one hand, a unified set of model parameters have already been proposed for three temperature levels and a constant applied electric field while simulating charge transport in LDPE and its nanocomposites. Thus, the realization of the model at different field strengths is desirable. On the other hand, the numerical model of charge transport in the filled enamel was developed for three values of the initial applied electric field and only one temperature level. The later simulation should be complemented at different temperatures. Once the models are able to reproduce experimental outcomes at numerous test protocols, its applicability is obviously more assertive. Besides, the extension of the computer models from 1D to 2D and 3D domains would be favorable for modeling charge transport processes in complex insulating structures utilized in practice.

As regards the effect of the multi-layered structures, several arrangements of laminated films and layered structures of enamels were used in experimental study while computer models were developed for simulating the dynamics of charge generation and transport in the latter. Since such multi-layered structures can be found in various applications, further investigations should be performed for practical geometry of solid insulations under their working conditions.

References

[1] G. Asplund, "HVDC towards more power and higher voltage - a challenge for the insulation," *Proc. 21st Nordic Insulation Symposiums (NORD-IS 09)*, Gothenburg, Sweden, 2009, pp. 127-130.

[2] J. W. Feltes, B. D. Gemmell, and D. Retzmann, "From smart grid to super grid: Solutions with HVDC and FACTS for grid access of renewable energy sources," *2011 IEEE Power and Energy Society General Meeting*, 2011, pp. 1-6.

[3] E. Persson, "Transient effects in application of PWM inverters to induction motors," *IEEE Trans. Ind. Appl.,* vol. 28, pp. 1095-1101, 1992.

[4] M. Kaufhold, H. Aninger, M. Berth, J. Speck, and M. Eberhardt, "Electrical stress and failure mechanism of the winding insulation in PWM-inverter-fed low-voltage induction motors," *IEEE Trans. Ind. Electron.,* vol. 47, pp. 396-402, 2000.

[5] D. Fabiani and G. C. Montanari, "The effect of voltage distortion on ageing acceleration of insulation systems under partial discharge activity," *IEEE Electr. Insul. Mag.,* vol. 17, pp. 24-33, 2001.

[6] L. Paulsson, B. Ekehov, S. Halen, T. Larsson, L. Palmqvist, A. A. Edris, D. Kidd, A. J. F. Keri, and B. Mehraban, "High-frequency impacts in a converter-based back-to-back tie; the Eagle Pass installation," *IEEE Trans. Power Del.,* vol. 18, pp. 1410-1415, 2003.

[7] T. Bengtsson, F. Dijkhuizen, L. Ming, F. Sahlen, L. Liljestrand, D. Bormann, R. Papazyan, and M. Dahlgren, "Repetitive fast voltage stresses-causes and effects," *IEEE Electr. Insul. Mag.,* vol. 25, pp. 26-39, 2009.

[8] T. Tanaka, "Dielectric nanocomposites with insulating properties," *IEEE Trans. Dielectr. Electr. Insul.,* vol. 12, pp. 914-928, 2005.

[9] S. U. Haq, S. H. Jayaram, and E. A. Cherney, "Performance of nanofillers in medium voltage magnet wire insulation under high frequency applications," *IEEE Trans. Dielectr. Electr. Insul.,* vol. 14, pp. 417-426, 2007.

[10] T. Tanaka, Y. Ohki, M. Ochi, M. Harada, and T. Imai, "Enhanced partial discharge resistance of epoxy/clay nanocomposite prepared by newly developed organic modification and solubilization methods," *IEEE Trans. Dielectr. Electr. Insul.,* vol. 15, pp. 81-89, 2008.

[11] H. Kikuchi and H. Hanawa, "Inverter surge resistant enameled wire with nanocomposite insulating material," *IEEE Trans. Dielectr. Electr. Insul.,* vol. 19, pp. 99-106, 2012.

[12] Y. Suzuoki, G. Cai, and M. Ieda, "Effects of interface on electrical conduction in polyethylene-(ethylene-vinyl acetate) copolymer composites," *J. Phys. D: Appl. Phys.,* vol. 17, pp. 141-146, 1984.

[13] K. S. Suh, J. Y. Kim, H. S. Noh, and C. R. Lee, "Interfacial charge in polyethylene/ethylene vinylacetate laminates," *IEEE Trans. Dielectr. Electr. Insul.,* vol. 3, pp. 758-764, 1996.

[14] X. Wang, Z. Lv, K. Wu, X. Chen, D. Tu, and L. A. Dissado, "Study of the factors that suppress space charge accumulation in LDPE nanocomposites," *IEEE Trans. Dielectr. Electr. Insul.,* vol. 21, pp. 1670-1679, 2014.

[15] IEC Standard 60093: "Methods of test for volume resistivity and surface resistivity of solid electrical insulating materials," 1980.

[16] J. G. Simmons, "Conduction in thin dielectric films," *J. Phys. D: Appl. Phys.,* vol. 4, pp. 613-657, 1971.

[17] V. Adamec and J. H. Calderwood, "Electrical conduction and polarisation phenomena in polymeric dielectrics at low fields," *J. Phys. D: Appl. Phys.,* vol. 11, pp. 781-800, 1978.

[18] M. Ieda, "Electrical conduction and carrier traps in polymeric materials," *IEEE Trans. Electr. Insul.,* vol. 19, pp. 162-178, 1984.

[19] T. Mizutani and M. Ieda, "Electrical conduction in solid dielectrics," *IEEE Trans. Dielectr. Electr. Insul.,* vol. 21, pp. 833-839, 1986.

[20] L. A. Dissado and J. C. Fothergill, "Charge injection and transport in insulating polymers," *Electrical degradation and breakdown in polymers*, IET, 1992.

[21] D. M. Taylor and T. J. Lewis, "Electrical conduction in polyethylene terephthalate and polyethylene films," *J. Phys. D: Appl. Phys.,* vol. 4, pp. 1346-1357, 1971.

[22] V. Adamec and J. H. Calderwood, "Electrical conduction in dielectrics at high fields," *J. Phys. D: Appl. Phys.,* vol. 8, pp. 551-560, 1975.

[23] P. Fischer and P. Röhl, "Transient currents in oxidized low-density polyethylene," *Mehrphasige Polymersysteme*. vol. 62, Steinkopff, 1977, pp. 149-153.

[24] V. Adamec and J. H. Calderwood, "On the determination of electrical conductivity in polyethylene," *J. Phys. D: Appl. Phys.,* vol. 14, pp. 1487-1494, 1981.

[25] S. Pelissou, H. St-Onge, and M. R. Wertheimer, "Electrical conduction of polyethylene below and above its melting point," *IEEE Trans. Electr. Insul.,* vol. 23, pp. 325-333, 1988.

[26] R. Nath, T. Kaura, and M. M. Perlman, "Steady-state conduction in linear low-density polyethylene with Poole-lowered trap depth," *IEEE Trans. Electr. Insul.,* vol. 25, pp. 419-425, 1990.

[27] G. Sawa, T. Inayoshi, Y. Nishio, S. Nakamura, and M. Ieda, "Determination of predominant carrier species in organic polymers by a galvanic cell," *J. Appl. Phys.,* vol. 48, pp. 2414-2418, 1977.

[28] G. C. Montanari, G. Mazzanti, F. Palmieri, A. Motori, G. Perego, and S. Serra, "Space-charge trapping and conduction in LDPE, HDPE and XLPE," *J. Phys. D: Appl. Phys.,* vol. 34, pp. 2902-2911, 2001.

[29] L. A. Dissado and J. C. Fothergill, "Polymers as wide band-gap insulators," *Electrical degradation and breakdown in polymers*, IET, 1992.

[30] C. A. Mead, "Electron transport mechanisms in thin insulating films," *Phys. Rev.,* vol. 128, pp. 2088-2093, 1962.

[31] J. G. Simmons, "Poole-Frenkel effect and schottky effect in metal-insulator-metal systems," *Phys. Rev.,* vol. 155, pp. 657-660, 1967.

[32] M. Ieda, G. Sawa, and S. Kato, "A consideration of Poole–Frenkel effect on electric conduction in insulators," *J. Appl. Phys.,* vol. 42, pp. 3737-3740, 1971.

[33] M. Unge, T. C, and T. Christen, "Space charges and deep traps in polyethylene – Ab initio simulations of chemical impurities and defects," *Proc. 2013 IEEE Int'l. Conf. Solid Dielectrics (ICSD)*, 2013, pp. 935-939.

[34] H. von Berlepsch, "Interpretation of surface potential kinetics in HDPE by a trapping model," *J. Phys. D: Appl. Phys.,* vol. 18, pp. 1155-1170, 1985.

[35] G. G. Raju, "Field enhanced conduction," *Dielectrics in electric fields*, Marcel Dekker, 2003.

[36] T. Tanaka and J. H. Calderwood, "Transient currents and electron mobility in polythene," *J. Phys. D: Appl. Phys.,* vol. 7, pp. 1295-1302, 1974.

[37] H. J. Wintle, "Decay of static electrification by conduction processes in polyethylene," *J. Appl. Phys.,* vol. 41, pp. 4004-4007, 1970.

[38] M. M. Perlman, T. J. Sonnonstine, and J. A. St.Pierre, "Drift mobility determinations using surface potential decay in insulators," *J. Appl. Phys.,* vol. 47, pp. 5016-5021, 1976.

[39] E. A. Baum, T. J. Lewis, and R. Toomer, "Decay of electrical charge on polyethylene films," *J. Phys. D: Appl. Phys.,* vol. 10, pp. 487-497, 1977.

[40] R. Toomer and T. J. Lewis, "Charge trapping in corona-charge polyethylene films," *J. Phys. D: Appl. Phys.,* vol. 13, pp. 1343-1356, 1980.

[41] T. Mizutani and M. Ieda, "Carrier transport in high-density polyethylene," *J. Phys. D: Appl. Phys.,* vol. 12, pp. 291-296, 1979.

[42] T. Mizutani, T. Tsukahara, and M. Ieda, "The effects of oxidation on the electrical conduction of polyethylene," *J. Phys. D: Appl. Phys.,* vol. 13, pp. 1673-1679, 1980.

[43] G. Chen, T. Y. G. Tay, A. E. Davies, Y. Tanaka, and T. Takada, "Electrodes and charge injection in low-density polyethylene using the pulsed electroacoustic technique," *IEEE Trans. Dielectr. Electr. Insul.,* vol. 8, pp. 867-873, 2001.

[44] J. M. Alison and R. M. Hill, "A model for bipolar charge transport, trapping and recombination in degassed crosslinked polyethene," *J. Phys. D: Appl. Phys.,* vol. 27, pp. 1291-1299, 1994.

[45] F. Boufayed, G. Teyssèdre, C. Laurent, S. Le Roy, L. A. Dissado, P. Ségur, and G. C. Montanari, "Models of bipolar charge transport in polyethylene," *J. Appl. Phys.,* vol. 100, 104105 (10 pp.), 2006.

[46] S. Le Roy, G. Teyssedre, C. Laurent, G. C. Montanari, and F. Palmieri, "Description of charge transport in polyethylene using a fluid model with a constant mobility: fitting model and experiments," *J. Phys. D: Appl. Phys.,* vol. 39, pp. 1427-1436, 2006.

[47] T. J. Lewis and J. P. Llewellyn, "Electrical conduction in polyethylene: The role of positive charge and the formation of positive packets," *J. Appl. Phys.,* vol. 113, 223705 (12 pp.), 2013.

[48] T. Tanaka, "Optical absorption and electrical conduction in polyethylene," *J. Appl. Phys.,* vol. 44, pp. 2430-2432, 1973.

[49] J. G. Simmons and M. C. Tam, "Theory of isothermal currents and the direct determination of trap parameters in semiconductors and isulators containing arbitrary trap distributions," *Phys. Rev. B,* vol. 7, pp. 3706-3713, 1973.

[50] P. K. Watson, "The energy distribution of localized states in polystyrene, based on isothermal discharge measurements," *J. Phys. D: Appl. Phys.,* vol. 23, pp. 1479-1484, 1990.

[51] P. Llovera and P. Molinié, "New methodology for surface potential decay measurements: application to study charge injection dynamics on polypropylene films," *IEEE Trans. Dielectr. Electr. Insul.,* vol. 11, pp. 1049-1056, 2004.

[52] M. Meunier and N. Quirke, "Molecular modeling of electron trapping in polymer insulators," *J. Chem. Phys.,* vol. 113, pp. 369-376, 2000.

[53] M. Meunier, N. Quirke, and A. Aslanides, "Molecular modeling of electron traps in polymer insulators: Chemical defects and impurities," *J. Chem. Phys.,* vol. 115, pp. 2876-2881, 2001.

[54] P. Mark and W. Helfrich, "Space-charge-limited currents in organic crystals," *J. Appl. Phys.,* vol. 33, pp. 205-215, 1962.

[55] S. Diaham and M.-L. Locatelli, "Space-charge-limited currents in polyimide films," *Appl. Phys. Lett.,* vol. 101, 242905 (4 pp.), 2012.

[56] E. Kanegae, Y. Ohki, T. Tanaka, Y. Sekiguchi, Y. Murata, and C. C. Reddy, "Space charge behavior in multi-layered dielectrics with LDPE and LDPE/MgO nanocomposites," *Proc. 10th IEEE Int'l. Conf. Solid Dielectrics (ICSD)*, 2010, pp. 1-4.

[57] S. Li, N. Zhao, Y. Nie, X. Wang, G. Chen, and G. Teyssedre, "Space charge characteristics of LDPE nanocomposite/LDPE insulation system," *IEEE Trans. Dielectr. Electr. Insul.,* vol. 22, pp. 92-100, 2015.

[58] T. J. Lewis, "Polyethylene under electrical stress," *IEEE Trans. Dielectr. Electr. Insul.,* vol. 9, pp. 717-729, 2002.

[59] T. J. Lewis, "Nanometric dielectrics," *IEEE Trans. Dielectr. Electr. Insul.,* vol. 1, pp. 812-825, 1994.

[60] S. Serra, E. Tosatti, S. Iarlori, S. Scandolo, and G. Santoro, "Interchain electron states in polyethylene," *Phys. Rev. B,* vol. 62, pp. 4389-4393, 2000.

[61] G. Chen and J. Zhao, "Observation of negative differential mobility and charge packet in polyethylene," *J. Phys. D: Appl. Phys.,* vol. 44, 212001 (4 pp.), 2011.

[62] A. See, L. A. Dissado, and J. C. Fothergill, "Electric field criteria for charge packet formation and movement in XLPE," *IEEE Trans. Dielectr. Electr. Insul.,* vol. 8, pp. 859-866, 2001.

[63] L. Boudou and J. Guastavino, "Influence of temperature on low-density polyethylene films through conduction measurement," *J. Phys. D: Appl. Phys.,* vol. 35, pp. 1555-1561, 2002.

[64] M. Roy, J. K. Nelson, R. K. MacCrone, and L. S. Schadler, "Candidate mechanisms controlling the electrical characteristics of silica/XLPE nanodielectrics," *J. Mater. Sci.,* vol. 42, pp. 3789-3799, 2007.

[65] R. J. Fleming, A. Ammala, S. B. Lang, and P. S. Casey, "Conductivity and space charge in LDPE containing nano- and micro-sized ZnO particles," *IEEE Trans. Dielectr. Electr. Insul.,* vol. 15, pp. 118-126, 2008.

[66] Y. Murakami, M. Nemoto, S. Okuzumi, S. Masuda, M. Nagao, N. Hozumi, and Y. Sekiguchi, "DC conduction and electrical breakdown of MgO/LDPE nanocomposite," *IEEE Trans. Dielectr. Electr. Insul.,* vol. 15, pp. 33-39, 2008.

[67] Y. Hayase, H. Aoyama, Y. Tanaka, T. Takada, and Y. Murata, "Space charge formation in LDPE/MgO nano-composite thin film under ultra-high DC electric stress," *Proc. 8th Int'l. Conf. Properties and Applications of Dielectric Materials*, 2006, pp. 159-162.

[68] T. J. Lewis, "Charge transport in polyethylene nano dielectrics," *IEEE Trans. Dielectr. Electr. Insul.,* vol. 21, pp. 497-502, 2014.

[69] T. Takada, Y. Hayase, Y. Tanaka, and T. Okamoto, "Space charge trapping in electrical potential well caused by permanent and induced dipoles for LDPE/MgO nanocomposite," *IEEE Trans. Dielectr. Electr. Insul.* , vol. 15, pp. 152-160, 2008.

[70] L. Zhang, Y. Zhou, J. Tian, Y. Sha, Y. Zhang, H. Wu, and Y. Wang, "Experiment and simulation of space charge suppression in LDPE/MgO nanocomposite under external DC electric field," *J. Electrostatics,* vol. 72, pp. 252-260, 2014.

[71] D. Min, W. Wang, and S. Li, "Numerical analysis of space charge accumulation and conduction properties in LDPE nanodielectrics," *IEEE Trans. Dielectr. Electr. Insul.,* vol. 22, pp. 1483-1491, 2015.

[72] T. Tanaka, M. Kozako, N. Fuse, and Y. Ohki, "Proposal of a multi-core model for polymer nanocomposite dielectrics," *IEEE Trans. Dielectr. Electr. Insul.,* vol. 12, pp. 669-681, 2005.

[73] E. O. Filatova and A. S. Konashuk, "Interpretation of the changing the band gap of Al2O3 depending on its crystalline form: Connection with different local symmetries," *J. Phys. Chem. C,* vol. 119, pp. 20755-20761, 2015.

[74] N. W. Green, A. R. Frederickson, and J. R. Dennison, "Experimentally derived resistivity for dielectric samples from the CRRES internal discharge monitor," *IEEE Trans. Plasma Sci.,* vol. 34, pp. 1973-1978, 2006.

[75] T. J. Lewis and A. J. Wright, "The electrical conductivity of magnesium oxide at low temperatures," *J. Phys. D: Appl. Phys.,* vol. 1, pp. 441-447, 1968.

[76] J. Mazierska, D. Ledenyov, M. V. Jacob, and J. Krupka, "Precise microwave characterization of MgO substrates for HTS circuits with superconducting post dielectric resonator," *Supercond. Sci. Technol.,* vol. 18, pp. 1-6, 2005.

[77] S. Diaham and M.-L. Locatelli, "Dielectric properties of polyamide-imide," *J. Phys. D: Appl. Phys.,* vol. 46, 185302 (8 pp.), 2013.

[78] S. K. Dolui, D. Pal, and S. Maiti, "Synthesis of a novel polyesterimide," *J. Appl. Polym. Sci.,* vol. 30, pp. 3867-3878, 1985.

[79] J. A. Crawford and R. W. Vest, "Electrical conductivity of single crystal Cr2O3," *J. Appl. Phys.,* vol. 35, pp. 2413-2418, 1964.

[80] R. C. Ku and W. L. Winterbottom, "Electrical conductivity in sputter-deposited chromium oxide coatings," *Thin Solid Films,* vol. 127, pp. 241-256, 1985.

[81] P. R. Chapman, R. H. Griffith, and J. D. F. Marsh, "The physical properties of chromium oxide-aluminium oxide catalysts. II. Electrical properties," *Proc. R. Soc. London, Ser. A,* vol. 224, pp. 419-426, 1954.

[82] A. Holt and P. Kofstad, "Electrical conductivity and defect structure of Cr2O3. II. Reduced temperatures (<1000°C)," *Solid State Ionics,* vol. 69, pp. 137-143, 1994.

[83] P. H. Fang and W. S. Brower, "Dielectric constant of Cr2O3 crystals," *Phys. Rev.,* vol. 129, pp. 1561-1561, 1963.

[84] G. Teyssedre and C. Laurent, "Charge transport modeling in insulating polymers: from molecular to macroscopic scale," *IEEE Trans. Dielectr. Electr. Insul.,* vol. 12, pp. 857-875, 2005.

[85] Y. Li and T. Takada, "Experimental observation of charge transport and injection in XLPE at polarity reversal," *J. Phys. D: Appl. Phys.,* vol. 25, pp. 704-716, 1992.

[86] M. Fukuma, M. Nagao, and M. Kosaki, "Computer analysis on transient space charge distribution in polymer," *Proc. 4th Int'l. Conf. Properties and Applications of Dielectric Materials*, 1994, pp. 24-27.

[87] K. Kaneko, T. Mizutani, and Y. Suzuoki, "Computer simulation on formation of space charge packets in XLPE films," *IEEE Trans. Dielectr. Electr. Insul.,* vol. 6, pp. 152-158, 1999.

[88] S. Le Roy, P. Segur, G. Teyssedre, and C. Laurent, "Description of bipolar charge transport in polyethylene using a fluid model with a constant mobility: model prediction," *J. Phys. D: Appl. Phys.,* vol. 37, pp. 298-305, 2004.

[89] Y. V. Serdyuk, S. M. Gubanski, and A. S. Mohammad, "Computer simulations of space charge dynamics and electric fields in HVDC cable insulation," *Proc. 15th Int'l. Symp. High Voltage Engineering*, 2007, paper T8-405.

[90] S. Le Roy, T. T. N. Vu, C. Laurent, and G. Teyssedre, "Modelling charge generation and transport in solid organic dielectrics under DC stress," *Proc. European Seminar on materials for HVDC cables and accessories: Performance, Modeling, Testing, Qualification (Jicable HVDC'13)*, 2013, paper 4.1.

[91] M. Taleb, G. Teyssedre, S. Le Roy, and C. Laurent, "Modeling of charge injection and extraction in a metal/polymer interface through an exponential distribution of surface states," *IEEE Trans. Dielectr. Electr. Insul.,* vol. 20, pp. 311-320, 2013.

[92] F. Baudoin, C. Laurent, G. Teyssedre, and S. Le Roy, "Charge packets modeling in polyethylene," *Appl. Phys. Lett.,* vol. 104, 152901 (4 pp.), 2014.

[93] T. J. Sonnonstine and M. M. Perlman, "Surface-potential decay in insulators with field-dependent mobility and injection efficiency," *J. Appl. Phys.,* vol. 46, pp. 3975-3981, 1975.

[94] S. Sahlia, A. Bellela, Z. Ziaria, A. Kahlouchea, and Y. Seguib, "Measure and analysis of potential decay in polypropylene films after negative corona charge deposition," *J. Electrostatics,* vol. 57, pp. 169-181, 2003.

[95] Z. Xu, L. Zhang, and G. Chen, "Decay of electric charge on corona charged polyethylene," *J. Phys. D: Appl. Phys.,* vol. 40, pp. 7085–7089, 2007.

[96] G. Chen, "A new model for surface potential decay of corona-charged polymers," *J. Phys. D: Appl. Phys.,* vol. 43, 055405 (7 pp.), 2010.

[97] M. Fukuma, M. Nagao, and M. Kosaki, "Numerical analysis on transient space charge distribution in XLPE," *Proc. 5th IEEE Int'l. Conf. Conduction and Breakdown in Solid Dielectrics (ICSD'95)*, 1995, pp. 139-143.

[98] M. H. Lean and W.-P. L. Chu, "Model for charge transport in ferroelectric nanocomposite film," *J. Polymers,* vol. 2015, 17 pp., 2015.

[99] L. K. H. Pallon, A. T. Hoang, A. M. Pourrahimi, M. S. Hedenqvist, F. Nilsson, S. Gubanski, U. W. Gedde, and R. T. Olsson, "The impact of MgO nanoparticle interface in ultra-insulating polyethylene nanocomposites for high voltage DC cables," *J. Mater. Chem. A,* vol. 4, pp. 8590-8601, 2016.

[100] A. Hjortsberg, G. Holmström, L. Johansson, and T. Karlsson, "Electrical conductor provided with a surrounding electrical insulation," Patent EP0287813 A2, 1988.

[101] J. A. Giacometti and O. N. Oliveira, "Corona charging of polymers," *IEEE Trans. Electr. Insul.,* vol. 27, pp. 924-943, 1992.

[102] M. A. Noras, "Non-contact surface charge/voltage measurements: Fieldmeter and voltmeter methods," *Trek Application Note No. 3002, Trek Inc.,* 2002.

[103] K. Ishimoto, E. Kanegae, Y. Ohki, T. Tanaka, Y. Sekiguchi, Y. Murata, and C. C. Reddy, "Superiority of dielectric properties of LDPE/MgO nanocomposites over microcomposites," *IEEE Trans. Dielectr. Electr. Insul.,* vol. 16, pp. 1735-1742, 2009.

[104] I. Kitani and K. Arii, "Anomalous discharge current in polyethylene (PE), ethylene-vinylacetate copolymer (EVA) and PE-EVA laminated films," *Jpn. J. Appl. Phys.,* vol. 24, pp. 285-288, 1985.

[105] I. Kitani, Y. Tsuji, and K. Arii, "Analysis of anomalous discharge current in low-density polyethylene," *Jpn. J. Appl. Phys.,* vol. 23, pp. 855-860, 1984.

[106] T. Mizutani, T. Oomura, and M. Ieda, "Anomalous TSC and space charge in high-density polyethylene," *Jpn. J. Appl. Phys.,* vol. 21, pp. 1195-1198, 1982.

[107] S. Kumara, Y. V. Serdyuk, and S. M. Gubanski, "Surface charge decay on polymeric materials under different neutralization modes in air," *IEEE Trans. Dielectr. Electr. Insul.,* vol. 18, pp. 1779-1788, 2011.

[108] P. Molinié, "Measuring and modeling transient insulator response to charging: the contribution of surface potential studies," *IEEE Trans. Dielectr. Electr. Insul.,* vol. 12, pp. 939-950, 2005.

[109] R. Coelho, P. Jestin, L. Levy, and D. Sarrail, "On the return-voltage buildup in insulating materials," *IEEE Trans. Electr. Insul.,* vol. 22, pp. 683-690, 1987.

[110] M. Ieda, G. Sawa, and U. Shinohara, "A decay process of surface electric charges across polyethylene film," *Jpn. J. Appl. Phys.,* vol. 6, pp. 793-794, 1967.

[111] W.-W. Shen, H.-B. Mu, G.-J. Zhang, J.-B. Deng, and D.-M. Tu, "Identification of electron and hole trap based on isothermal surface potential decay model," *J. Appl. Phys.,* vol. 113, 083706 (6 pp.), 2013.

[112] T. Mizutani, Y. Suzuoki, and M. Ieda, "Thermally stimulated currents in polyethylene and ethylene–vinyl-acetate copolymers," *J. Appl. Phys.,* vol. 48, pp. 2408-2413, 1977.

[113] A. T. Hoang, Y. V. Serdyuk, and S. M. Gubanski, "Dielectric relaxation in LDPE/Al2O3 nanocomposite," unpublished.

[114] M. M. Perlman, "Thermal currents and the internal polarization in carnauba wax electrets," *J. Appl. Phys.,* vol. 42, pp. 2645-2652, 1971.

[115] R. A. Creswell and M. M. Perlman, "Thermal currents from corona charged mylar," *J. Appl. Phys.,* vol. 41, pp. 2365-2375, 1970.

[116] G. F. J. Garlick and A. F. Gibson, "The electron trap mechanism of luminescence in sulphide and silicate phosphors," *Proc. Phys. Soc., London,* vol. 60, pp. 574-590, 1948.

[117] T. A. T. Cowell and J. Woods, "The evaluation of thermally stimulated current curves," *Brit. J. Appl. Phys.,* vol. 18, pp. 1045-1051, 1967.

[118] C. Bucci, R. Fieschi, and G. Guidi, "Ionic thermocurrents in dielectrics," *Phys. Rev.,* vol. 148, pp. 816-823, 1966.

[119] Y. Asano and T. Suzuki, "Characteristics of polyethylene terephthalate electrets," *Jpn. J. Appl. Phys.,* vol. 11, pp. 1139-1146, 1972.

[120] J. van Turnhout, "Thermally stimulated discharge of electrets," *Electrets,* Springer Berlin Heidelberg, 1980, pp. 81-215.

[121] P. Fischer and P. Röhl, "Thermally stimulated and isothermal depolarization currents in low-density polyethylene," *J. Polym. Sci.: Polym. Phys. Ed.,* vol. 14, pp. 531-542, 1976.

[122] F. Tian, Q. Lei, X. Wang, and Y. Wang, "Effect of deep trapping states on space charge suppression in polyethylene/ZnO nanocomposite," *Appl. Phys. Lett.,* vol. 99, 142903 (3 pp.), 2011.

[123] A. Many and G. Rakavy, "Theory of transient space-charge-limited currents in solids in the presence of trapping," *Phys. Rev.,* vol. 126, pp. 1980-1988, 1962.

[124] L. Chen, D. H. Tran, Y. C. Quintero, and R. Ramprasad, "Charge injection barriers at metal/polyethylene interfaces," *J. Mater. Sci.,* vol. 51, pp. 506-512, 2015.

[125] A. K. Jonscher, *Dielectric relaxation in solids*. London: Chelsea Dielectrics Press, 1983.

[126] X. Ma, N. H. Lee, H. J. Oh, J. S. Hwang, and S. J. Kim, "Preparation and characterization of silica/polyamide-imide nanocomposite thin films," *Nanoscale Res. Lett.,* vol. 5, pp. 1846-1851, 2010.

[127] M. Hasegawa, Y. Sakamoto, Y. Tanaka, and Y. Kobayashi, "Poly(ester imide)s possessing low coefficients of thermal expansion (CTE) and low water absorption (III). Use of bis(4-aminophenyl)terephthalate and effect of substituents," *Eur. Polym. J.,* vol. 46, pp. 1510-1524, 2010.

[128] T. A. Hahn, "Thermal expansion of copper from 20 to 800 K—Standard reference material 736," *J. Appl. Phys.,* vol. 41, pp. 5096-5101, 1970.

[129] H. Scher and R. Zallen, "Critical density in percolation processes," *J. Chem. Phys.,* vol. 53, pp. 3759-3761, 1970.

[130] Y. V. Serdyuk, A. D. Podoltsev, and S. M. Gubanski, "Numerical simulations of dielectric properties of composite material with periodic structure," *J. Electrostatics,* vol. 63, pp. 1073-1091, 2005.

[131] O. Wiener, "Die theorie des mischkörpers fur das feld der stationären strömung," *Abh. Math. Phys. Kl. Akad. Wiss. Leipzig,* vol. 32, pp. 509-604, 1912.

[132] T. Okamoto, K. Abe, Y. Itoh, and T. Umemura, "Partial discharge resistant mechanism of newly developed enameled wire," *Ann. Rep. IEEE Conf. Electrical Insulation and Dielectric Phenomena,* 1997, pp. 512-515.

[133] G. Paulsson, F. Sahlen, H. Hillborg, A. Björklund, M. Takala, and J. Andersson, "New type of PD-resistant enameled wire," *Proc. 12th Int'l. Electrical Insulation Conf.*, Birmingham, UK, 2013, pp. 169-174.

[134] R. M. Hill and L. A. Dissado, "The temperature dependence of relaxation processes," *J. Phys. C: Solid State Phys,* vol. 15, pp. 5171-5193, 1982.

[135] E. Tuncer and S. M. Gubanski, "Electrical properties of filled silicon rubber," *J. Phys.: Condens. Matter,* vol. 12, pp. 1873-1897, 2000.

[136] E. Kuffel, W. S. Zaengl, and J. Kuffel, *High voltage engineering: Fundamentals*: Newnes, 2000.

[137] P. Molinié, M. Goldman, and J. Gatellet, "Surface potential decay on corona-charged epoxy samples due to polarization processes," *J. Phys. D: Appl. Phys.,* vol. 28, pp. 1601-1610, 1995.

[138] V. I. Arkhipov, J. A. Popova, and A. I. Rudenko, "Space-charge perturbed dispersive transport in disordered dielectrics," *J. Electrostatics,* vol. 18, pp. 23-37, 1986.

[139] W. Tomaszewicz, "Surface-potential decay of disordered solids," *J. Electrostatics,* vol. 51, pp. 340-344, 2001.

[140] A. T. Hoang, Y. V. Serdyuk, and S. M. Gubanski, "Charge decay on enamel wire surface," *Proc. 2014 Int'l. Conf. High Voltage Engineering and Application (ICHVE 2014)*, Poznan, Poland, 2014, paper A-4-3.

[141] P. Molinié, "A review of mechanisms and models accounting for surface potential decay," *IEEE Trans. Plasma Sci.,* vol. 40, pp. 167-176, 2012.

[142] H. Sjostedt, S. M. Gubanski, and Y. V. Serdyuk, "Charging characteristics of EPDM and silicone rubbers deduced from surface potential measurements," *IEEE Trans. Dielectr. Electr. Insul.,* vol. 16, pp. 696-703, 2009.

[143] A. R. Frederickson and J. R. Dennison, "Measurement of conductivity and charge storage in insulators related to spacecraft charging," *IEEE Trans. Nucl. Sci.,* vol. 50, pp. 2284-2291, 2003.

[144] J. Kindersberger and C. Lederle, "Surface charge decay on insulators in air and sulfurhexafluorid - part I: simulation," *IEEE Trans. Dielectr. Electr. Insul. ,* vol. 15, pp. 941-948, 2008.

[145] P. Molinié, "Potential decay interpretation on insulating films: necessity of combining charge injection and slow volume polarization processes," *Proc. 7th Int'l. Conf. Dielectric Materials, Measurements and Applications*, 1996, pp. 50-55.

[146] W. S. Zaengl, "Dielectric spectroscopy in time and frequency domain for HV power equipment. I. Theoretical considerations," *IEEE Electr. Insul. Mag.,* vol. 19, pp. 5-19, 2003.

[147] M. M. Shahin, "Mass-spectrometric studies of corona discharges in air at atmospheric pressures," *J. Chem. Phys.,* vol. 45, pp. 2600-2605, 1966.

[148] M. Negishi, K. Akada, K. Takizawa, H. Miyake, Y. Tanaka, and T. Takada, "Space charge accumulation in coating materials for motor windings under DC high voltage," *Proc. Int'l. Conf. Condition Monitoring Diagnosis,* 2012, pp. 122-125.

[149] F. H. Kreuger, *Industrial high DC voltage*, Delft University Press, 1995.

[150] D. Min, M. Cho, S. Li, and A. R. Khan, "Charge transport properties of insulators revealed by surface potential decay experiment and bipolar charge transport model with genetic algorithm," *IEEE Trans. Dielectr. Electr. Insul.,* vol. 19, pp. 2206-2215, 2012.